Leaching of uranium and heavy metals from acid producing black shales

Experiments and modeling study

Lars-André Erstad

Master Thesis in Geoscience
Environmental geology
60 credits

Department of Geosciences
Faculty of Mathematics and Natural sciences

UNIVERSITY OF OSLO

JUNE 2017

II

Leaching of uranium and heavy metals from acid producing black shales

Experiments and modeling study

Lars-André Erstad

Master Thesis in Geoscience
Environmental geology
60 credits

Department of Geosciences
Faculty of Mathematics and Natural sciences

UNIVERSITY OF OSLO

JUNE 2017

IV

Leaching of uranium and heavy metals from acid producing black shales – experiments and modelling study

Lars-André Erstad

Abstract

The Scandinavian black shales, known as alum shales are found in the eastern part of Norway, stretching across Sweden and into the Baltics. In Norway, it is found throughout the most densely popluated areas around Oslo as well in urban centres around lake Mjøsa. Due to its high sulfide content, alum shales can produce significant acid rock drainage if exposed to oxygen and water. The acid runoff can contain high concentrations of heavy metals which can cause severe damage to the environment. These factors have led to strong restrictions on the depositions of excess masses containing alum shale. Only a few deposits capable of storing such masses exist in Norway, leading to high costs in relation to excess masses from construction projects.

The long- and short term leaching potential of alum shale was assessed through an outdoor bulk- and a laboratory column experiment. Water samples were analyzed for Al, Fe, V, Co, Ni, Zn, Cu, Sr, Mo, Cd, Pb, Hg, Th, Na, K, Mg, Ca and SO_4 using QICP-MS and IC. The results were anlyzed with statistical software. XRD and SEM were used to identify possible heavy metal and uranium bearing mineral phases. The results were combined into a geochemical model in PHREEQC to to estimate mineral dissolution kinetics and assess the long term leaching potential of zink and uranium.

Results from the leaching experiments show that after almost two years, pH conditions in the bulk experiment are circum neutral (pH 8 - 6) due to buffering from dissolution of carbonates in the rock. Despite the relatively high pH, Zn, Ni, Cu, Cr, Cd and U show a high mobility and aqueous concentrations far exceed Norwegian standards for drinking water and environmental quality. Al, V, Mo and Pb all show a low mobility.

Mineralogical analyses indicate that sulfides such as sphalerite, chalcopyrite, arsenopyrite and galena are important in understanding the leaching of Zn, Cd, Cu, As and Co. Uranium was found in monazite, apatite and uranium oxide. The geochemical model shows that calcite buffering can keep pH at near neutral conditions for at least 50 years. A rate constant for Zn mobilization due to sphalerite dissolution in alum shale of 1.1×10^{-17} mol/g/s was found by applying a 1st-order rate law, which is apparently lower than the 3.24×10^{-3} mol/m^2/s rate constant found by Acero et al. (2007) even though the constants cannot be directly compared.

Keywords: alum shale, black shale, uranium, heavy metals, leaching, phreeqc.

Acknowledgements

This thesis would not be possible without the assistance of Halldis Fjermestad at the Norwegian Public Roads Administration Thank you for letting us use your equipment and for providing us with data.

Håkon S. Børresen for good cooperation and help, not only with this thesis, but throughout the last five years. Thank you for being so organized and remembering all the things I forget.

Thank you to my supervisors, Helge Hellevang and Per Aagaard.

I would like to extend a special thanks to the professors and staff that have helped me on the way to completing this thesis. Firstly, Beyene Girma Haile for assisting in sample preparation and XRD analysis of our rock samples. Mufak Said Naoroz for helping us with water sampling equipment and ion chromatography. Siri Simonsen for helping us with the QICP-MS analyses. Salahalldin Akhavan for making excellent thin sections from our crappy samples. Berit Løken Berg for assistance with the SEM analyses.

To my family, thank you for great support during the last five years. I know you will probably stop reading at this point because you don't understand the remainder of this paper anyway. That's ok, you tried with my BSc. To my fellow student and girlfriend Rikke, thank you for making the last six months so much more enjoyable. Last, but not least thank you Hamkam for a great start of the football season; ett liv, ett lag!

x

Table of contents

1   Introduction

In the National Transport Plan for 2006 – 2015, the Norwegian parliament decided to upgrade the main road (Rv 4) between Oslo and Gjøvik to improve safety, transportation and the local environment (St.meld. Nr. 024 (2003 - 2004)). The construction project is the responsibility of the Norwegian Public Roads Administration (NPRA) and started in spring 2013. The new road is planned to open in 2020 (NPRA, 2016a). A stretch of the road, going from Roa – Jaren in Gran municipality required cutting and tunneling through acid producing black shale known as alum shale.

The alum shale is found throughout the Oslo region and eastern Norway, stretching across Sweden into the Baltics. The shales are known for being particularly rich in carbon (10 - 15 %), sulfur and heavy metals such as cadmium (Cd), arsenic (As), copper (Cu), nickel (Ni), lead (Pb), zink (Zn), vanadium (V) and uranium (U) (Nakrem and Worsley, 2007, Armands, 1973, Bjørlykke, 1974). Alum shale is well known for its issues related to geotechnics, health and the environment. The problems arise when the shale is exposed to water and oxygen, this can cause the shale to swell and induce structural damage to buildings and infrastructure (NGI, 2015). Oxidation of sulfides can cause acid rock drainage which leads to release of heavy metals which can have a negative effect on the environment (Shokes and Möller, 1999). The alum shale is enriched in uranium (up to 200 mg/kg), the radioactive decay of uranium produces radon gas (Schoene, 2013). Radon is radioactive and is the second most important cause of lung cancer in Norway after smoking (NRPA, 2016).

An NPRA's research and development project Nordic Road Water (NORWAT) was started in January 2012 with the purpose of limiting the damage to aquatic environments during construction and operation of the road network (NPRA, 2016b). Several studies were undertaken to investigate the effect of road construction in acid producing rocks (Skipperud et al., 2016). The studies have revealed that there is a risk of negative impact on the environment due to leaching of heavy metals and uranium during construction works in areas with acid producing rocks. Regulations on deposition of acid producing rock are strict, and such masses must be treated as contaminated soil (Lovdata, 2004). Shale containing more than 80 mg /kg uranium can have an activity of >1 Bq/kg which is the limit for radioactive waste and must be deposited as such (NGI, 2015). Deposit sites for hazardous waste are limited in Norway and deposition is therefore costly. It is therefore in environmental and economic interest to develop

methods to assess the leaching potential of such rocks without the need for a large number of drillcores and expensive chemical analyses.

Main objectives of this study:

- Investigate long term leaching of heavy metals and uranium from acid producing black shales in oxidizing conditions through natural leaching experiments.

- Use controlled column experiments to reproduce weathering processes in acid producing black shales.

- Compare water chemistry to rock mineralogy, with the purpose of identifying mineral phases to which heavy metals are bound.

- Use numerical geochemical modelling to assess long term leaching of heavy metals from acid producing black shales in aerobic conditions.

Statement of cooperation

The experiments forming the scientific basis of this thesis were conducted in cooperation with fellow master student Håkon S. Børresen. This included experimental setups, field work, laboratory work, SEM analyses and XRD result analyses. The results were interpreted individually and each thesis written with different objectives and without cooperation, using the same raw data.

2 Background

2.1.1 Study area

The main study area is located in Gran municipality in Oppland county, north of Oslo. Gran is situated in a geological area known as the Oslo-graben. The map in Figure 1 (left) shows the new stretch of road going from Roa to Lygna and the lithology of the area. Material has also been sampled from a different road construction project nearby, E16 Nymoen – Olum. The samples were taken from two boreholes drilled near Jevnaker, Oppland shown in Figure 1 (right).
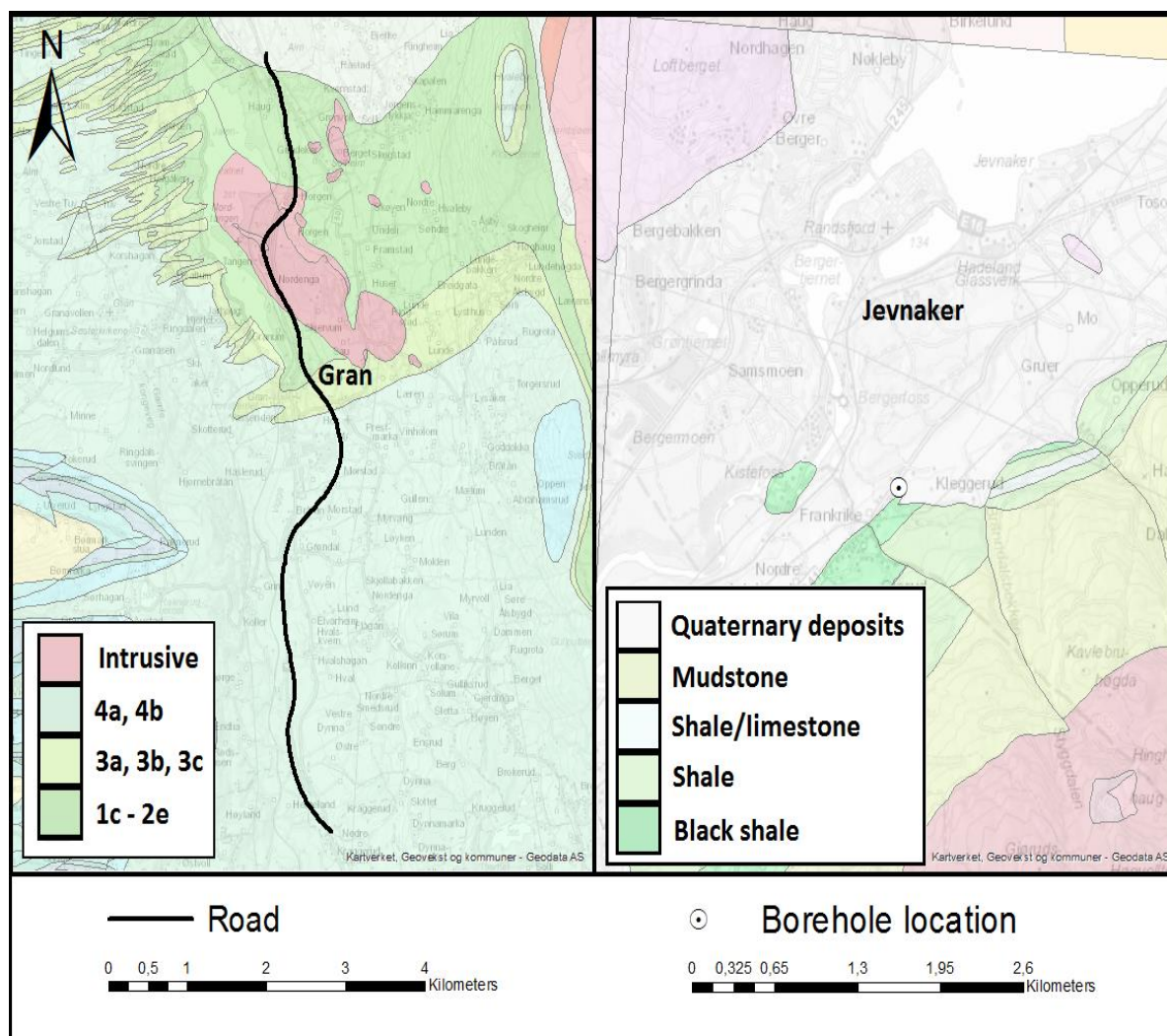
Figure 1: Maps showing the location of the new road near Gran (left) and the borehole location near E16 Nymoen - Olum (right). Different lithologies named according to NGU. **1c-2e**: Alum shale. **3a-3c**: Shale and limestone. **4a-4b**: Shale and limestone. For further information see section 1.1.2. Figure made with maps from NGU, Kartverket and Geodata AS.

2.1.2 Regional geology

The Oslo graben system is a result of rifting and volcanism in the Permian. The rift stretches from Langesund in the south to the northern part of lake Mjøsa (Figure 2). The graben system is bordered by Precambrian basement rocks to the east and west (Larsen et al., 2007). Geologically, the area is varied with a thick succession of sedimentary rocks ranging from Precambrian sparagmites (feldspar rich arkose) in the Hedmark Group, to the late Silurian sandstones of the Ringerike Group. The Cambro-Silurian rocks are followed by a large variety of volcanic intrusives and extrusives formed during the Permian rifting event (Nakrem and Worsley, 2007).
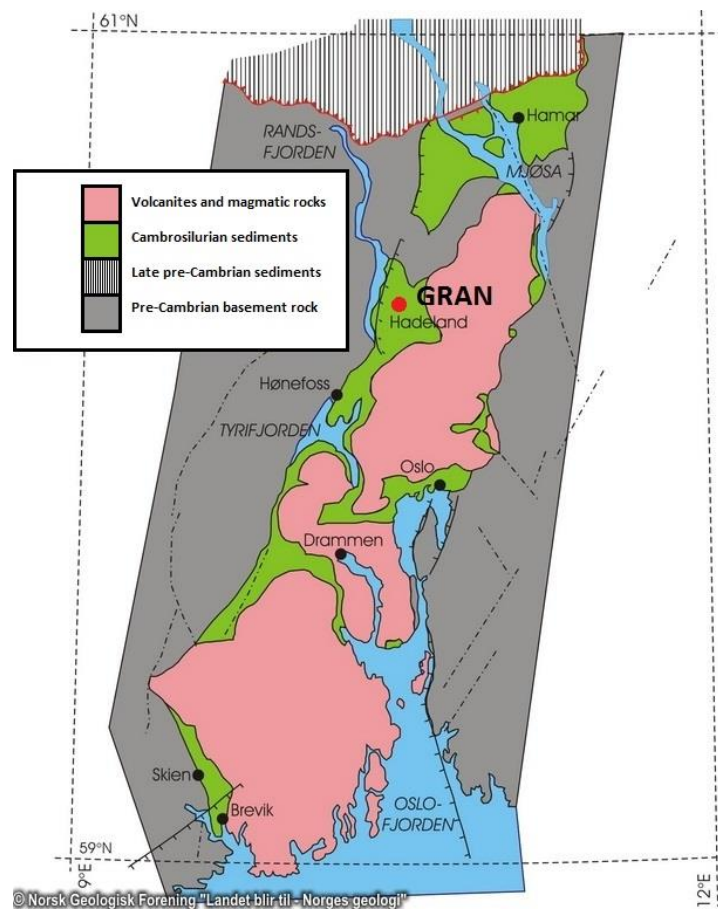
Figure 2: Map showing the region known as the Oslo-graben system. Figure modified from Nakrem and Worsley (2007)

Sedimentary stratigraphy

The Cambro-Silurian rocks in the Oslo region have been thoroughly described through numerous works (Owen et al., 1990, Bjørlykke, 1974 and references therein). The lithology is divided into five groups, which are further divided into 24 formations. The stratigraphy covers 10 stages with further subdivisions (Bjørlykke, 1974, Nakrem and Worsley, 2007). The rocks through which the tunnel was constructed are all found in the Røyken Group which consists of the Alum shale (2e-3a), Bjørkåsholm (3aγ), Tøyen (3b) and Huk (3c) formations (Figure 3).

The Alum shale Formation has a thickness of about 75 m and consists of carbon rich black shales and thin layers of limestone (Owen et al., 1990). Overlying the alum shale is the

Bjørkåsholm Formation (3aγ), made up of limestone and shale approximately 1 m thick (Owen et al., 1990). Above stage 3aγ lies the 20 m thick Tøyen Formation (3b) which can be divided into the Galgeberg Member and the Hagastrand Member (Owen et al., 1990). It consists mainly of black shales and shales. The last formation in the Røyken Group is the Huk Formation (3c), consisting of massive limestone (Owen et al., 1990).

For this study, the Alum shale Formation and the Galgeberg Member are of most importance as these can be considered acid

Age		Formation	Stage	Lithology
Ordovician 485 – 443 Ma	Early	Huk	3c	Limestone
		Tøyen	3b	Shale
		Bjørkåsholm	3aγ	Shale and limestone
			3a	
Cambrian 541 – 485 Ma	Late	Alum shale	2e	Shale
	Mid			
	Early			

Figure 3: Stratigraphic chart of the Røyken group in the lower Cambrosilurian sediments in the Oslo region. Figure modified from Nakrem and Worsley (2007).

producing (NGI, 2015). The Galgeberg Member is an approximately 10 m thick black shale of early Ordovician age. Mineralogical studies of this shale are limited, but it has a higher than average sulfur and uranium content (NGI, 2015). It is found all throughout the southern part of the Oslo graben, stretching into western and southern Sweden (Owen et al., 1990). The alum shales were deposited in the late Cambrian to early Ordovician, when the ocean intruded over the flat landscapes of Baltica (Nakrem and Worsley, 2007). The formation extends north from Oslo up to the Mjøsa area, and eastwards across Sweden and into the Baltics (Puura et al., 1999).

2.2   Theory and previous studies

Shales are siliciclastic sedimentary rocks, composed of mainly fine grained quartz, clay minerals and feldspars, but also contain varying degrees of metals, carbonates, sulfides and organic material. Due to the abundancy of fine grained sediments and quiet-water depositional environments, shales (and mudstones) make up roughly 50 % of all sedimentary rocks (Boggs, 2011). Black shales are a type of shale, named so after its black color. The black color is due to a high content of organic matter (normally 2 – 10 %) (Tourtelot, 1979). The depositional environment in which black shales are formed are thought to have been much like the conditions found in anoxic bottom waters today. In a water column with a low rate of vertical circulation, and a high accumulation of organic matter, oxidation of organic matter consumes oxygen,

leading to anoxia. When oxygen is depleted, dissolved sulfate (SO_4^{2-}) will act as an electron acceptor and is reduced to form hydrogen sulfide (H_2S). H_2S can then react with iron to form pyrite (FeS_2) (Berner, 1985). Other trace metals are also precipitated out from seawater and trapped in the sediment. Due to these processes, black shales are normally enriched in heavy metals and sulfur compared to crustal averages (Rudnick and Gao, 2004, Armands, 1973, Bjørlykke, 1974). Black shales are economically important in many parts of the world as the high carbon content make them a source of fossil fuels, and the recent developments in shale oil extraction has made shale oil competitive with traditional petroleum source rocks.

The Scandinavian alum shales have also been used as a resource. In Sweden, the shales have a long tradition of economic exploitation, starting with alum ($KAl(SO_4)_2·12H_2O$) production from which the shale bears its name, to oil and uranium extraction. Due to the economic importance, several studies have been done to establish its mineralogical and hydrocarbon content (e.g. Armands (1973), Erlström (2014) and references therein). The mining of alum shale has also created large heaps of burnt and weathered shale which have led to several studies concerning the leaching of potential hazardous trace elements from the shale and shale residue (Allard et al., 1991, Bäckström and Sartz, 2015, Falk et al., 2006, Karlsson et al., 2011, Lavergren et al., 2009a, Lavergren et al., 2009b, Puura et al., 1999).

The Norwegian alum shale has not had any economic importance, and only a few in-depth pure studies of mineralogy exist (e.g. Bjørlykke (1974), Gautneb and Sæther (2009) and references therein). Most studies in Norway are related to health, environmental and geotechnical problems in relation to building and infrastructure construction e.g. (Abreham, 2007, Bjørlykke, 1974, Fjermestad, 2013, NGI, 2015, Oftedahl, 1955).

2.2.1 Mineralogy

The bulk mineralogical composition of alum shale does not differ greatly from that of "normal" shale. Main mineral constituents include quartz, feldspars, calcite and clay minerals such as chlorite, muscovite and illite in varying degrees (Armands, 1973, Bjørlykke, 1974, Lavergren et al., 2009a, Fjermestad, 2013). Other clay minerals and oxides and have also been identified, but not in a quantifiable amount. The proposed sedimentation rate for the alum shale is 1 mm/1000 years, indicating sedimentation of a very fine grained material ($< 10\,\mu m$) (Bjørlykke, 1974). What separates alum and black shale from 'normal' shale is the high content of organic carbon, sulfur and trace elements.

6

Organic carbon content can be as high as 15 % and sulfur up to 5 - 6 % (Armands, 1973, Bjørlykke, 1974). Trace element content is also high, this is expanded upon further in chapter 2.2.3.

Armands (1973) divided the alum shale into five mineral fractions: detritus, authigenic, sulfide, carbonate and organic fraction. Detrital minerals are a weathering products that are incorporated into the shale, examples include quartz, feldspar, zircon and various oxides. Authigenic minerals are formed during sedimentation or lithification, typical minerals are calcite, pyrite, pyrrhotite, kaolinite, illite and other clay minerals. The last three fractions divide the trace elements by which mineral phases they are associated with and can be both authigenic and detrital. Certain minerals and elements were found to be associated with each of the different fractions, either as their own mineral phases, as substitutions in other mineral structures or adsorbed to mineral surfaces.

2.2.2 Major elements

Sulfur (S)

Alum shales are highly enriched in sulfur compared to average crustal values (Table 1). Most of the sulfur is bound as sulfides, of which pyrite is the most dominant (Armands, 1973, Bjørlykke, 1974).

Iron (Fe)

Fe levels in alum shale are reported between 60.7 mg/kg up to 60000 mg/kg. Leaching tests and sequential chemical extraction (SCE) indicate that most Fe is bound in weathering resistant oxides and silicates, and that the Fe mobilized is likely due to pyrite oxidation. (Yu et al., 2014, Lavergren et al., 2009b, Lavergren et al., 2009a, Allard et al., 1991, Fjermestad, 2013).

Aluminum (Al)

The concentrations of Al in alum shale vary from 71.5 mg/kg up to approximately 70 000 mg/kg. Sequential extraction and leaching indicate that most Al is bound in more weathering resistant minerals such as clays and feldspars and thus shows a low mobility (Fjermestad, 2013, Yu et al., 2014, Lavergren et al., 2009b, Lavergren et al., 2009a, Allard et al., 1991).

Calcium (Ca)

Calcium in alum shale is mostly bound in calcite, but other carbonates such as secondarily formed dolomite and ankerite can occur. The Ca concentrations in the shale vary from 3200 mg/kg up to 71000 mg/kg (Lavergren et al., 2009b, Fjermestad, 2013, Allard et al., 1991)

2.2.3 Trace elements

Trace elements are defined as elements in rocks occurring in concentrations of less than 0.1 % by weight or 1000 mg/kg (Britannica, 2017). Data on trace element content in alum shale is somewhat limited, and most studies only cover a selection of elements. Cu, Ni, V, U and Zn are included in most studies. As, Cd, Cr, Mo, Pb, Co and S are more limited, while Th is only covered in one study (Table 1).

Table 1: Concentrations of selected trace elements documented in mid Cambrian – early Ordovician black shales in previous studies. Some of the values are averages of all samples listed in the different studies. All concentrations are in mg/kg.

Element	Avg. Earth crust[1]	Gran[2], NOR	Billingen[3], SWE	Oslo[4], NOR	Oslo[5], NOR	Billingen[6], SWE	Degerhamn[7], SWE	Kvarntorp[8], SWE	Maardu[9], Estonia	Öland[10], SWE
As	4.8	21	-	-	-	106	121	79	-	121
Cd	0.09	4.7	-	-	-	2.5	5.81	-	-	5.5
Co	17.3	11	-	-	-	-	24.6	-	-	-
Cr	92	-	94	140	135	320	80.8	-	-	-
Cu	28	94	190	104	156.7	110	157	-	125	117
Mo	1,1	21	-	-	-	340	97	163	210	-
Ni	47	78	160	98	201.3	200	163	70	95	107
Pb	17	46	-	-	33	14	27.1	-	120	-
S	621	14000	-	25870	38012	-	65200	-	-	-
Th	10.5	-	-	10.2	-	-	-	-	-	-
U	2.7	22	206	150	113.8	300	72.4	235	120	-
V	97	-	680	484	1022	750	1150	650	900	-
Zn	67	300	150	86	136.5	130	297	-	125	277

[1]Rudnick and Gao (2004), [2]Fjermestad (2013), [3]Armands (1973), [4]Bjørlykke (1974), [5]Abreham (2007), [6]Allard et al. (1991), [7]Lavergren et al. (2009a), [8]Bäckström and Sartz (2015), [9]Puura et al. (1999), [10]Falk et al. (2006).

Trace elements highly enriched in the shale (Factor > 10)

Uranium (U)

Uranium is highly enriched in the alum shale at levels up to 300 mg/kg, with higher concentrations in some of the Swedish shales (Table 1). Different studies of U in alum shales has indicated a somewhat complex behavior. Sequential extraction has indicated that U is bound to more weathering resistant minerals in the residual fraction (up to 50 %) (Lavergren et al., 2009a, Fjermestad, 2013). Armands (1973) found a strong statistical correlation between U and authigenic K-feldspar, but the study also showed that acid leaching of U was almost complete. The study concluded that U probably occurs as UO_2, U_3O_8, adsorbed or included in apatite or fixed in uranyl humates. Helmers (2013) and Yu et al. (2014) both indicate that much of the U is leachable both under acid and near neutral conditions and concludes that the easily mobilized fraction of U is bound to carbonates or loosely bound to the shale matrix or Fe/Mn-oxides, especially in weathered rocks.

Molybdenum (Mo)

Molybdenum is at 1.1 mg/kg, a relatively rare element in the earth's crust, but is found enriched in alum shale from 21 up to 340 mg/kg (Table 1). Armands (1973) found Mo to be correlated with organic carbon, potassium and K-feldspar. Sequential extraction performed by Lavergren et al. (2009a) showed high mobility of Mo in water based leaching experiments and suggested that this was due to Mo occurring as thiomolybdates (MoS_4^{2-}) which are easily transformed to Molybdate (MoO_4^{2-}). A large fraction of Mo was also released during targeting of sulfides and organic matter. Fjermestad (2013) did not see the same mobility for Mo in Norwegian alum- and black shales and indicated that Mo is bound in more stable minerals and sulfides not easily oxidized. Therefore, the evidence in the existing literature indicates that the behavior of Mo is split between an easily mobilized fraction bound to organics, and one low mobility fraction bound to more weathering resistant minerals.

Vanadium (V)

Vanadium is enriched in the shale, with levels up to 12 times that of the earth's crust (Table 1). Studies have indicated that V is associated to the organic carbon content in alum shales (Bjørlykke, 1974). Armands (1973) found a correlation between V and S, but no correlation

with iron. This indicates that it is not associated with pyrite, but rather to organic sulfur. Sequential extraction shows low mobility for V (Lavergren et al., 2009a).

Arsenic (As)

Arsenic is enriched in alum shale up to 25 times the crustal average (Table 1). The content is 4 - 5 times higher in the Swedish shale, but only one Norwegian study (Fjermestad, 2013) includes this metal. The behavior of As during sequential extraction suggests it is associated with sulfides, but it is not easily mobilized by oxidation (Lavergren et al., 2009a). Fjermestad (2013) found As to be associated with the residual fraction, indicating a binding to more weathering resistant minerals. Lavergren et al. (2009a) suggests the behavior is due to binding on oxides during oxidation.

Cadmium (Cd)

Cadmium is highly enriched in the alum shale at 28 – 65 times the crustal average (Table 1). Studies have shown Cd to have high mobility by ionic substitution and oxidation. Current research points towards Cd being bound as sulfides more easily oxidized than pyrite and sorbed on mineral surfaces (Lavergren et al., 2009a, Fjermestad, 2013).

Trace elements moderately enriched in the shale (Factor > 2)

Zinc (Zn)

Zinc is found in alum shale at an enrichment factor of 1.3 - 4.5 (Table 1). Lavergren et al. (2009a) and Fjermestad (2013) found Zn to be associated with sulfide, but not pyrite. This is similar to Armands (1973) and Bjørlykke (1974) who found a low correlation with sulfur and low concentrations of Zn in pyrite. The main conclusions are that Zn occurs as a separate sulfide phase, or bound in silicates.

Copper (Cu)

The copper content in alum shale is 3 – 7 times the crustal average (Table 1). Bjørlykke (1974) found a strong correlation between Cu and S. Cu is shown to have a low correlation with, and concentration in pyrite, which indicates that Cu occurs as a separate sulfide phase or in silicates (Armands, 1973, Bjørlykke, 1974, Fjermestad, 2013). Results from sequential extraction

10

supports these findings and suggests that Cu mainly occurs in mineral such as chalcopyrite ($CuFeS_2$), bornite (Cu_5FeS_4) and chalcocite (Cu_2S) (Lavergren et al., 2009a).

Nickel (Ni)

Nickel is enriched in the alum shale in a factor of 1.5 - 4.2 compared to the crustal average (Table 1). Ni is correlated with sulfur and chlorite, but is not found in high concentrations in pyrite (Armands, 1973, Bjørlykke, 1974). Sequential extraction done by Lavergren et al. (2009a) and Fjermestad (2013) indicates that Ni is bound in separate sulfide phases and in silicates.

Trace elements weakly enriched in the shale (Factor < 2)

Thorium (Th)

Few studies include thorium and data is therefore quite limited. Bjørlykke (1974) found Th to be bound in detrital minerals such as zircon and monazite. These findings are supported by Fjermestad (2013) where Th showed low solubility and remained in the residual fraction.

Lead (Pb)

Lead content in alum shale ranges from 14 - 120 mg/kg (Table 1). Sequential extraction shows Pb likely bound in sulfides and adsorbed to oxides and carbonates. In general, Pb shows low mobility and is mostly contained in the residual fraction (Lavergren et al., 2009a, Fjermestad, 2013).

Cobalt (Co)

The behavior of cobalt in alum shale is not well studied. Sequential extraction shows an association with sulfide but not pyrite, in the same pattern as Ni, Zn and Cu. This indicates a possible binding to a separate sulfide phase (Lavergren et al., 2009a, Fjermestad, 2013).

Chromium (Cr)

Chromium is found enriched to levels between 80 – 320 mg/kg compared to the crustal average of 92 (Table 1). Experiments have found Cr to be highly immobile and associated with the

residual fraction (Lavergren et al., 2009a). This is supported by Bjørlykke (1974) who suggested that Cr is present in illite as substitution for Al and occurring as a trace element in chlorite where it shows a strong correlation with Ni.

2.2.4 Chemistry of weathering reactions

Pyrite oxidation

Alum shales have a high sulfur content, most of which is bound in different sulfides. Pyrite (FeS_2) and pyrrhotite ($Fe_{(x-1)}S$) are two important sulfur bearing minerals found in alum shales (NGI, 2015, Oftedahl, 1955). Pyrite is the most common sulfide mineral and often occurs together with other sulfides or oxides in ore deposits (Nesse, 2012). The oxidation of pyrite in e.g. mine tailings can lead to water acidification and release of heavy metals known as acid mine/acid rock drainage (Nordstrom, 2011). This can cause significant environmental damage, and the oxidation process of pyrite has therefore been studied quite extensively (Appelo and Postma, 2005).

The electrochemical reaction of pyrite oxidation happens in three stages. First a cathodic reaction transfers electrons from the crystal surface to the oxidant. The second step involves the transportation of charge from an anodic reaction to replace the electrons. The third step involves oxygen in a water molecule interacting with a sulfur atom at an anodic site to form a sulfoxy specie, releasing an electron into the crystal and protons into solution (Rimstidt and Vaughan, 2003). Pyrite can be oxidized by either dissolved molecular oxygen (O_2) or ferric iron (Fe^{3+}) according to the following reactions (Heidel and Tichomirowa, 2011, Williamson and Rimstidt, 1994):

$$FeS_2 + 3.5O_2 + H_2O \rightarrow Fe^{2+} + 2SO_4^{2-} + 2H^+ \qquad \text{(React. 2.2.1)}$$

$$FeS_2 + 14Fe^{3+} + 8H_2O \rightarrow 15Fe^{2+} + 2SO_4^{2-} + 16H^+ \qquad \text{(React. 2.2.2)}$$
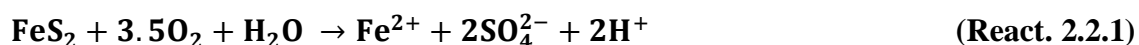
The overall reaction is well understood, but knowledge about the individual oxidation/reduction steps are limited due to the complex process. The overall oxidation can be seen as a two-step process. In the first step (reaction 2.2.1) pyrite either reacts directly with molecular oxygen, yielding sulfate (SO_4^{2-}) and ferrous iron (Fe^{2+}) or it dissolves into ferrous iron and disulfide (S_2^{2-}), which reacts with oxygen to form sulfate (Appelo and Postma, 2005). The second step is

12

the oxidation of pyrite by ferric iron according to reaction 2.2.2. Both reactions are acid producing. The Fe^{2+} produced by reaction 2.2.1 can be oxidized to Fe^{3+} thereby resulting in a higher rate. Fe^{2+} is stable in aqueous solutions at low pH, and the solubility of Fe^{3+} is low at high pH (Hem, 1972, Beverskog and Puigdomenech, 1996) as it will precipitate to form iron oxides/hydroxides such as hematite or goethite, this in turn will limit the oxidation rate (Appelo and Postma, 2005). The process is therefore dependent on iron oxidizing bacteria such as *Acidithiobacillus ferrooxidans* and *Leptospirillum ferrooxidans* which act as a catalysts by oxidizing Fe^{2+} to Fe^{3+} (Nordstrom, 2011, Appelo and Postma, 2005).

The process of pyrite oxidation can therefore be divided in two based on the pH of the solution. Oxidation by O_2 at higher pH and oxidation by Fe^{3+} at lower pH. Williamson and Rimstidt, 1994 proposed three different rate laws for pyrite oxidation (unit is mol/m^2/s):

By O$_2$: $$R = 10^{-8.19} * m_{O_2}^{0.5} * m_{H^+}^{-0.11} \quad \textbf{(Eq. 2.2.3)}$$

By Fe^{3+} in aerobic conditions: $$R = 10^{-6.07} * m_{Fe^{3+}}^{0.93} * m_{Fe^{2+}}^{-0.40} \quad \textbf{(Eq. 2.2.4)}$$

By Fe^{3+} in anaerobic conditions: $$R = 10^{-8.58} * m_{Fe^{3+}}^{0.3} * m_{Fe^{2+}}^{-0.47} * m_{H^+}^{-0.32} \quad \textbf{(Eq. 2.2.5)}$$

As mentioned, the oxidation of Fe^{2+} is a rate limiting factor, and if there is no presence of iron oxidizing bacteria, the process will be slow in near neutral conditions. Another rate limiting factor is the availability of oxygen, even though pyrite can be oxidized by iron in anaerobic conditions (Heidel and Tichomirowa, 2011). Other factors such as trace metal impurities in the crystal structure can cause an increase in the oxidation rate (Lehner et al., 2007). The crystal size of the pyrite can also affect the rate because of variations in surface area (Rimstidt and Vaughan, 2003).

Pyrrhotite oxidation

Pyrrhotite ($Fe_{(x-1)}S$) is a non-stochiometric monosulfide occurring in the alum shale together with pyrite, especially in zones subjected to contact metamorphism (Antun, 1967). Oxidation of pyrrhotite is faster than oxidation of pyrite (Nicholson and Scharer, 1993), and therefore alum shale containing pyrrhotite can potentially be more reactive than alum shale containing only pyrite. The oxidation rate of pyrrhotite has been much less studied, but the factors affecting it are the same as for pyrite (Belzile et al., 2004). Pyrrhotite is oxidized by molecular oxygen and ferric iron according to reactions 2.2.6 and 2.2.7:

$$Fe_{1-x}S + \left(2 - \frac{1}{2}x\right)O_2 + xH_2O \rightarrow (1-x)Fe^{2+} + SO_4^{2-} + 2xH^+ \qquad \text{(React. 2.2.6)}$$

$$Fe_{1-x}S + (8-2x)Fe^{3+} + 4H_2O \rightarrow (9-3x)Fe^{2+} + SO_4^{2-} + 8H^+ \qquad \text{(React. 2.2.7)}$$
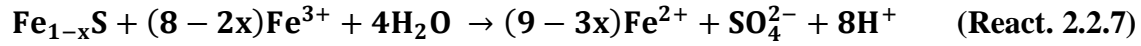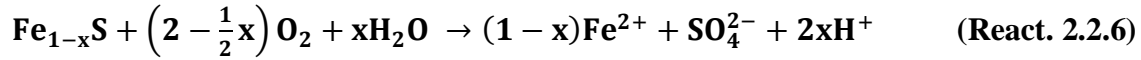
Sorption

Sorption is a broad term, covering three different processes that bind trace metal ions and keep them out of solution. Adsorption is the term used when the ion is bound to a mineral surface, absorption occurs when the ion is incorporated into the mineral structure. Ion exchange occurs when an ion changes place with an ion already sorbed to another mineral. Some heavy metals such as lead and cadmium sorb very strongly and surface complexation is needed to explain the behavior of such elements in solution (Appelo and Postma, 2005). Certain minerals have charged surfaces due to crystal structure deficits or ionic substitutions. Examples include Fe-oxides/hydroxides and clay minerals such as montmorillonite $((Na,Ca)_{0.3}(Al,Mg)_2Si_4O_{10}(OH)_2 \cdot nH_2O)$ in which Mg can substitute for Al leading to a net negative charge. Variable surface charge is a phenomenon which is observed on such charged particles when there is change in the pH of the solution. At a certain pH, the negative surface charge will be fully compensated by protons and give a net charge of zero, this is known as the point of zero charge (PZC). When pH is above PZC, the surface will have a negative charge, when pH goes below PZC the surface charge is positive due to protons occupying the sorption sites (Appelo and Postma, 2005). This means that at low pH most heavy metals will be in solution due to their positive charge.

Variable surface charge is important to understand the behavior of some trace metals released during pyrite weathering. As previously mentioned, the oxidation process can form Fe^{3+} which can precipitate as the iron hydroxide goethite (FeO(OH)). The crystal structure of goethite can contain double or single coordinated oxygen atoms at the surface to which heavy metal ions can easily sorb. Surface complexation is usually modelled by either the Gouy-Chapman double layer model, or the Stern-Grahame triple layer model (Appelo and Postma, 2005).

Element transport

The transportation velocity v_i of an element i in solution is related to the velocity of water v_{H2O} through the *retardation equation* (eq. 2.2.11) (Appelo and Postma, 2005):

14

$$v_i = \frac{v_{H_2O}}{(1+\frac{dq}{dc_i})} \quad \text{(m/s)} \qquad\qquad \text{(Eq. 2.2.11)}$$

Where $\frac{dq}{dc_i}$ is the slope of the sorption isotherm for the particular element. A sorption isotherm describes the relation between the concentration, c_i (mol/l) of an element in solution and the sorbed concentration q, expressed in mol/l of pore water (by multiplying the sorbed concentration e.g. mol/g soil by the bulk density of the soil e.g. g/l and dividing by the water filled porosity). The two most common sorption isotherms (Figure 4) are described by the Freundlich (eq. 2.2.12) and the Langmuir (eq. 2.2.13) equations (Appelo and Postma, 2005).

Freundlich isotherm: $\qquad\qquad\qquad q = K_F * c_i^n \qquad$ **(Eq. 2.2.12)**

K_F and n are adjustable coefficients. The Freundlich isotherm is empirical and does not have a maximum limit for sorption, meaning that if the concentration increases, the sorption continues to increase (Figure 4).

Langmuir isotherm: $\qquad\qquad\qquad q = \frac{q_{max} * c_i}{K_L + c_i} \qquad$ **(Eq. 2.2.13)**

q_{max} is the total concentration of sorption sites, K_L is an adjustable coefficient. The Langmuir isotherm is physically based on the assumption that there exists a finite number of sorption sites, and sorption is therefore limited by the number of sites.

The transportation of an element in solution is therefore dependent on the affinity of the element to sorb to charged particles and the nature of the material the water must pass through.
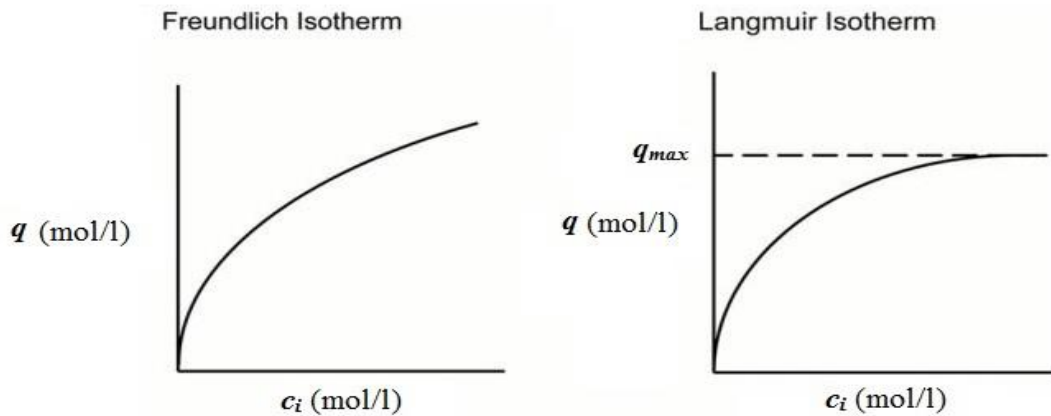
Figure 4: Sketch of the Freundlich and Langmuir sorption isotherms. Figure modified from Goldberg et al. (2007).

Rate laws for mineral dissolution

The generally accepted rate law for dissolution/precipitation reactions is given in equation 2.2.14 (Appelo and Postma, 2005).

$$R = k\frac{A_0}{V}\left(\frac{m_t}{m_0}\right)^n g(c) \qquad \text{(mol/L/s)} \qquad \textbf{Eq. 2.2.14}$$

R is the overall rate, **k** (mol/m^2/s) is the specific rate constant **A$_0$** (m^2) is the surface area of the solid reactant, **V** (m^3) is the solution volume, **m$_0$** and **m$_t$** are the amount of moles of reactant initially and at time t. **n** is a function of grain size and **g(c)** accounts for effects such as pH and distance to equilibrium among others (Appelo and Postma, 2005, Palandri and Kharaka, 2004, Lasaga, 1995). When information about solution composition, crystal size and surface area is limited, a simplified empirical rate law may be applied, given in eq. 2.2.15:

$$R = k(1 - \Omega) \qquad \text{(mol/L/s)} \qquad \textbf{Eq. 2.2.15}$$

R and **k** are the same as before, but in this expression **g(c)** in eq. 2.2.14 has been replaced with the saturation state Ω=**IAP/K** (Ionic Activity Product/Solubility product)**,** when $\Omega \rightarrow 1$, (1 - Ω) $\rightarrow 0$ allowing the rate to slow down towards zero at equilibrium (Rimstidt and Barnes, 1980).

3   Methods

3.1   Rock samples

In total, 16 rock samples were collected for the XRD, thin sections and laboratory leaching experiment. Ten of the samples came from Rv. 4 Gran and were taken from the bulk experiment containers. Out of these ten, three were Galgeberg shale, three were alum shale from the roadcut and four were alum shale from the tunnel. A geological profile of the tunnel is shown in Figure 5, with approximate locations of the sampling locations. The last six samples came from the two boreholes near Jevnaker (Figure 1). The borehole samples were taken from different depths (Table 2). A core log showing the different lithologies and sampling depths is shown in Figure 6.

Table 2: List of rock samples collected for XRD, thin section analysis and the column experiment.

Location:	Sample Name:	Galgeberg shale	Alum shale (roadcut)	Alum shale (tunnel)	Borehole 1	Borehole 2
Gran	A1		x			
	A2K		x			
	A3		x			
	G1	x				
	G2	x				
	G3K	x				
	AT1			x		
	AT2			x		
	AT3K			x		
	AT4K			x		
Jevnaker	BH1N - 1 m				x	
	BH1N - 3 m				x	
	BH1N - 7 m				x	
	BH1N - 8 m					x
	BH2S - 1 m					x
	BH2S - 5 m					x
	BH2S - 9 m					x
	BH2S - 15 m					x

Figure 5: Profile of the northern half of the tunnel near Gran (Figure 1) showing the different stratigraphic units and the approximate positions the samples for the bulk experiments were taken from (based on descriptions from NPRA). Samples A1-A3K were taken outside the tunnel. Figure modified from original unpublished material produced by Multiconsult for NPRA and given to the author by Halldis Fjermestad at the NPRA.

18
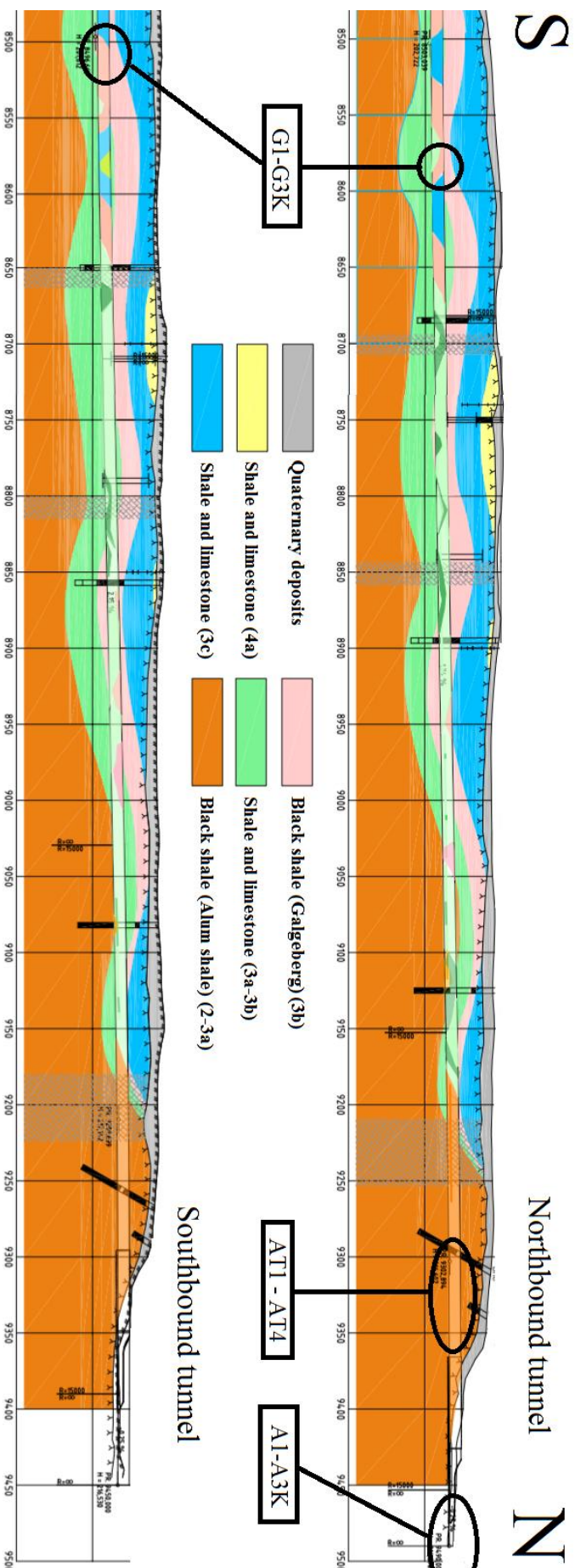
3.2 Leaching experiments

3.2.1 Bulk experiment

The large scale natural leaching experiment was set up near the road construction site at Gran in Oppland. The purpose of the experiment was to see how the shale reacted with water and oxygen under «natural» conditions. For the original experiment, the NPRA used 1 m^3 IBC (intermediate bulk container) containers which had the top removed, and were filled with approximately 200 liters of rock material. The precise volume of rock is uncertain, as it was measured using ten liter buckets. IBC containers are fitted with a valve at the bottom, this was left open and 20 liter jugs

Figure 6: Core logs from Boreholes 1 and 2 at Jevnaker, showing the different lithologies with sample names and depths. Figure modified from Multiconsult (2014).

were placed underneath together with a funnel (Figure 7). The jugs and the funnel were covered with plastic to prevent rainwater from entering directly into the jugs. The idea of the experiment is that the infiltrating water will react with oxygen and the rock material, the water can then be sampled from the jugs and analyzed for trace elements, sulfur, pH, EH and EC.
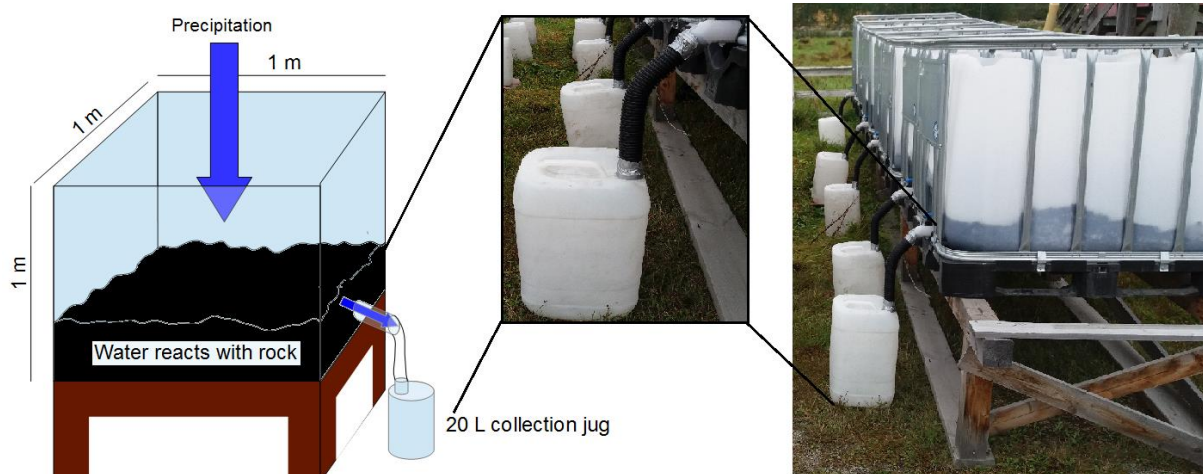
Figure 7: Conceptual sketch (left) and actual photo of the bulk experiment after it was moved to Roa.

Experiment 1 and 2

Experiment 1 was set up by the Norwegian Public Roads Administration (NPRA) and ran from 01/08/2014 to 19/05/2015. It was set up using ten containers. Five containers were filled with black shale from the Galgeberg Member blasted from the tunnel. Ten L of granulated dolomite was added to one of the containers (G3K). Two containers were mixed 75/25 (G4H) and 50/50 (G5H) with limestone from the Huk formation. The remaining five containers were filled with alum shale from the road construction site. A1 and A3 containing only alum shale. A2K was mixed with 10 L granulated dolomite, while A4H and A5H was mixed 75/25 and 50/50 with Huk limestone. The grain size of the material in both experiments varied greatly, from very fine grained up to cobble size.

In experiment 2, alum shale from the tunnel was used. They were labelled AT1, AT2, AT3K and AT4K. AT1 and AT2 contains 200 L of alum shale, while AT3K and AT4K had 200 L of shale and ten and 20 l of crushed limestone added respectively. The experiment ran from 21/5 to 18/6/2015.

The granulated dolomite that was added contained some trace elements that could have had a small effect on the experiment, in addition to this, some tapwater was added to the containers in dry periods, which could also impact the results slightly. The analysis results from experiment 1 and 2 are included in appendix II, but for detailed description and analyses of these results, see Fjermestad et al. (2017).

Experiment 3

Experiment 3 was set up on the 21/9-2016 as a continuation of selected containers from experiment 1 and 2 (Table 3). The remaining containers were moved from Gran to nearby Roa. No new material was added to the containers, and none of the containers with limestone from the Huk formation were included (A4H, A5H, G4H and G5H). Instead of using funnels and plastic cover to collect water in the 20 L jugs, hoses were fitted connecting the jugs to the containers (Figure 7).

Table 3: List of the experimental containers and the type of material contained in each.

Name	Galgeberg shale	Alum shale (roadcut)	Alum shale (tunnel)	Granulated dolomite	Crushed limestone
G1	200 L	-	-	-	-
G2	200 L	-	-	-	-
G3K	200 L	-	-	10 L	-
A1	-	200 L	-	-	-
A3	-	200 L	-	-	-
A2K	-	200 L	-	10 L	-
AT1	-	-	200 L	-	-
AT2	-	-	200 L	-	-
AT3K	-	-	200 L	-	10 L
AT4K	-	-	200 L	-	20 L

Sampling methods

About 1 L of the content in the 20 L jug was first used to wash the measuring cup, the sampling tubes and the syringe before each respective sampling. If the content in the jug was inadequate for washing and sampling, Milli-Q deionized water was used instead.

- 1 L (or less, if the sample was small) of water was transferred to the measuring cup.

- Eh, pH, EC and temperature of the sample was measured.

- 35 – 50 ml of the sample was drawn into the syringe and transferred to two, 50 ml centrifuge tubes through a 0.45 µm filter, one for anion/cation analysis and one for trace element analysis. The sample to be used for trace element analysis had 1 - 2 droplets of 1 % HNO_3 added to prevent ions precipitating out of solution.

Samples were collected every two weeks, 5/10, 19/10, 1/11 and 16/11-2016

3.2.2 Column experiment

The purpose of the column experiment was to simulate "natural" leaching conditions similar to the bulk experiment, but in a more controlled environment. For this experiment the rock samples were taken from the boreholes from the E16 Nymoen – Olum project. The sampling depths and lithologies are shown in Figure 6. The experiment ran from 7/12-2016 to 16/1-2017. Samples were collected once a day except for weekends. Between 21/12 and 16/1 no samples

were collected and the pump was shut off, giving a residence time of 26 days for the last sample collected.

Experiment setup

The experiment was set up using five syringes with their plungers removed, as columns. To ensure saturated conditions the peristaltic pump was connected to the bottom to pump water upwards. A cotton filter was added to the top of the column to prevent particles in the sampled water (Figure 8). All columns were fitted with hoses for easy sampling. The columns were filled with a mix of quartz sand and crushed shale. The quartz sand was added to increase the permeability as a previous attempt using only shale material failed due to pressure build up because of lack of flow.
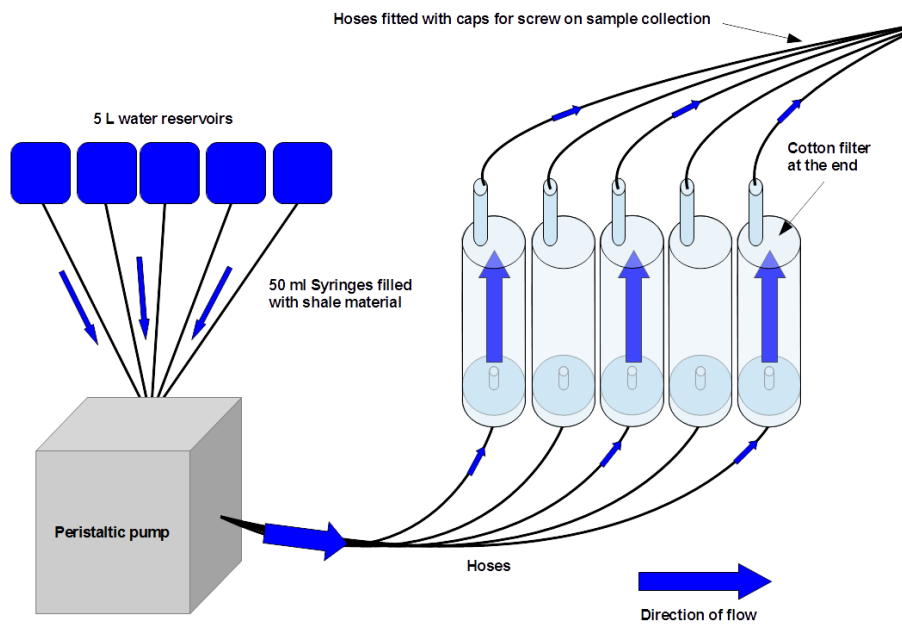
Figure 8: Conceptual sketch of the column experiment.

Sample preparation

- First, the empty columns were weighed.

- The shale samples were crushed using a sling mill.

- Approximately 30 g of crushed shale was added to a plastic container. For the mixed samples 15 g of each sample was added.

- 70 g of quartz sand was added to the crushed shale and the sample mixed by shaking.

- Each column was then filled with 50 ml of the sand/shale mixture and weighed again, the amount of shale and quartz in each column was then calculated by subtracting the column weight and multiplying by the mixing factor.

Table 4 gives an overview of which samples are in which column and the respective shale/sand ratios.

Table 4: Overview of which samples were put in which column, the amount of sample and the amount of shale/quartz.

Syringe no.:	1	2	3	4	K (control)
Sample:	BH1N - 3m	BH1N - 7+8 m	BH2S - 5+9m	BH2S - 15 m	Sand
Quartz sand (g)	20.84	49.14	42.85	40.81	63
Shale (g)	9.06	21.16	16.85	17.49	0

Potential errors

There are some factors that can produce erroneous results in this experiment. Firstly, the sand was not "pure", some organic material and broken shells were observed. To counter this, the control column (K) was set up. The process of mixing the shale/sand material by shaking can produce sorting due to gravity and grain size, causing smaller particles to settle towards the bottom and thus creating a different mixing ratio.

3.3 Water sample analysis

3.3.1 Cation/anion analysis (Ion chromatography)

Ion chromatography works by injecting the sample into an eluent and then pumping it through two ion exchange columns containing an anion or cation exchange resin depending on what is being analyzed. The ions are then separated according to their affinity to the different exchange sites and the solution passes through a conductivity suppressor to reduce the conductivity of the eluent. After neutralization, the solution is passed through a conductivity detector which detects the amount of cations or anions in the sample. The concentration is then calculated by using external standards (UIO, 2016, UIO, 2013).

Sample preparation

All water samples were filtered with a 0.45 µm filter to prevent particles in solution. Each sample was then diluted 10, 100 and 1000 times with Milli-Q deionized water using the following method:

- 1 ml of sample transferred to a 15 ml centrifuge tube using a pipette. 9 ml of deionized water was then added to the tube and shaken. This sample was used as the 10x solution.

- 1 ml of the 10x solution was then transferred to a new 15 ml centrifuge tube and mixed with 9 ml of deionized water to produce a 100x solution.

- 1 ml of the 100x solution was transferred to a new 15 ml centrifuge tube and mixed with 9 ml of deionized water to produce the 1000x solution.

The samples were then analyzed for the cations sodium (Na), potassium (K), magnesium (Mg), calcium (Ca), and the anions fluoride (F), chloride (Cl) and sulfate (SO_4). Bromide (Br^-) and nitrate (NO_3) were also included in the analyses, but were not included in the results due to too many gaps in the data.

The analyses were done by Mufak Said Naoroz at the Institute for Geosciences, University of Oslo. The equipment used were Dionex ICS-1000/2000 Ion Chromatography System (1000 for cations, 2000 for anions).

3.3.2 Trace element analysis (QICP-MS)

Quadrupole Inductively Coupled Plasma Mass Spectrometry uses a plasma source to convert the atoms in a sample to ions. Argon gas is converted to plasma, the sample is then introduced into the plasma and the atoms in the sample are ionized. The ions are focused into the mass spectrometer using an electrostatic lens. Here the ions are separated by their charge-to-mass ratio in a quadrupole mass filter. The quadrupole mass filter only allows ions of a single charge-to-mass ratio to pass at a time. The detectors then count the ions, and the software calculates the concentration based on a reference standard (Wolf, 2005).

Sample preparation

The samples from the bulk experiment were filtered in the field using a syringe and a 0.45 µm filter to reduce the amount of particles in solution. After filtering, a droplet of 1% HNO_3 was added to prevent precipitation. The samples had to be further diluted with HNO_3 due to high measured conductivity as the machine can only handle 1000 mg/l total dissolved solids (TDS).

1. 1 gram of sample was added to a 15 ml centrifuge tube.

2. 9 grams of 1 % HNO_3 was added to each sample and the sample was shaken.

The samples from the controlled lab experiment were filtered and 10 ml were transferred 15 ml centrifuge tubes. 0.01 ml of 2% HNO_3 was then added to each sample.

Analyses were done by Siri Simonsen at the Institute for Geosciences, University of Oslo using the Bruker Aurora elite quadrupole Inductively Coupled Mass Spectrometer (ICP-MS). A total of 13 elements were analyzed, Aluminum (Al), Vanadium (V), Chrome (Cr), Iron (Fe), Cobalt (Co), Nickel (Ni), Copper (Cu), Zink (Zn), Strontium (Sr), Molybdenum (Mo), Cadmium (Cd), Mercury (Hg), Lead (Pb), Thorium (Th) and Uranium (U). To remove molecular interference, Brukers Collision Reaction Interface II was used with helium gas when analyzing the lighter elements (Al, V, Cr, Fe, Co, Ni, Cu, Zn, Sr and Mo). The helium gas reduces molecular interference by colliding with multiatomic ions, while letting single atoms through. For the heavier element analysis (Sr, Mo, Cd, Hg, Pb, Th and U) no gas was used.

Five standards were used, and run as unknowns:

- Etalon 30 µg/l for Al, V, Cr, Fe, Co, Ni, Cu, Zn, Sr and Mo.

- Trace metals in drinking water (TMDW) for Al, V, Cr, Fe, Co, Ni, Cu, Zn, S, Mo, Cd, Hg and Pb.

- 68A for Sr, Th, Mo, and U.

- 6020-5 µg/l for Cd, Hg and Pb.

- 6020-50 µg/l for Al, V, Cr, Fe, Co, Ni, Cu and Zn.

3.3.3 Statistical analysis of water sample results

The anion/cation and trace element analyses yielded a large amount of data. To investigate any correlation between the behavior of the elements, statistical analyses were applied. Correlation analysis was performed on the following parameters: Al, V, Cr, Fe, Co, Ni, Cu, Zn, Sr, Mo, Cd, Pb, U, Na, K, Mg, Ca, F, Cl, SO_4 and pH. The purpose of this was to find groups of elements showing similar behavior that can be investigated further.

To produce enough data points, the analysis results from each experiment were grouped together in three groups (A1, A2K, A3), (G1, G2, G3K) and (AT1, AT2, AT3K, AT4K) instead of analyzing each container separately. Two parameters were calculated, the Spearman correlation coefficient ρ and the p-value **p.**

The Spearman correlation coefficient is a measure of how well the relationship between two variables can be described by a monotonic function (Hauke and Kossowski, 2011). It is the correlation between the rank of the variables and is described by the formula:

$$\boldsymbol{\rho = 1 - \frac{6\Sigma d_j^2}{n(n^2-1)}} \qquad\qquad \textbf{(Eq. 3.3.1)}$$

Where **n** is the number of observations and $\mathbf{d_j = X_j - Y_j}$ is the difference between the ranks $\mathbf{X_j}$, $\mathbf{Yj}$ of each variable pair $\mathbf{X_i}$ and $\mathbf{Y_i}$ (Graham and Ian, 2008).

The p-value is a measure of the probability of the data obtaining its value if the null hypothesis is true (the null hypothesis being that there is no relationship between the variables) (Braut, 2015).

Calculations using R

All calculations were performed using the statistical software R (version 3.2.3 (2015-12-10)).

- The data was copied into a .txt file for importation in R.

- The Spearman correlation coefficient and the significance was calculated using the Harrel Miscellaneous package in R. The tool yields a correlation matrix which lists ρ for each pair of variables and a matrix of p-values.

- Using the correlation matrix, the variables showing a strong/moderate positive or strong/moderate negative correlation ($\rho > 0.7/0.5$ or $\rho < -0.7/-0.5$) were selected for further analysis.

The input code used in R is listed in appendix III.

Potential errors

The largest source of error in this method is given by the few number of data points (analyses) to compare. Statistical analysis was only performed on the results generated from four sampling occasions. For G1 - G3K this only gives 10 data points for each variable.

3.4 Mineralogy

3.4.1 X-ray powder diffraction (XRD)

X-ray diffractometers consist of a sample holder, an X-ray tube, an X-ray detector, and a goniometer to measure angles. They are widely used for mineral identification through the powder diffraction method. X-rays are generated in a cathode ray tube by directing high energy free electrons at a metal target. The free electrons dislodge an electron from the innermost orbit of an atom in the target. When an electron from a higher energy orbit move in and replace the dislodged electron radiation with a specific wavelength λ (measured in Ångstrøm) is emitted. Electrons moving from the L and M orbits generate a characteristic wavelength known as Kα and Kβ. Only monochromatic (single wavelength) X-rays are used, so the radiation is filtered through either metal foil or a monochrometer (Nesse, 2012).

After filtering, the radiation is directed toward the sample being analyzed. The X-rays interact with the atoms in the crystal lattice of the sample producing constructive interference according to Bragg's law (eq. 3.4.1):

$$n\lambda = 2dSin\Theta \qquad \text{(Eq. 3.4.1)}$$

Where λ is the X-ray wavelength, **d** is the space between the crystal lattice planes and **θ** is the incident angle of the X-ray. Constructive interference between two waves occurs when *n* is equal to an integer multiple of the wavelengths λ of the X-rays diffracted from two parallel atomic planes in the crystal lattice (Nesse, 2012, Dinnebier et al., 2008). In X-ray powder

diffraction, the sample is placed in a goniometer that is rotated at an angle θ between 0° - 90° relative to the X-ray tube. The detector is continuously rotated at an angle 2θ (normally ~5° and 70°) relative to the sample, recording the intensity of the reflected X-rays. A peak in the intensity is an indication that the mineral being radiated has atomic planes with a d-spacing capable of reflecting X-rays for the angle θ (Nesse, 2012). The recorded peaks are displayed in a diffractogram and the d-spacing can then be checked against the Powder Diffraction File (http://www.icdd.com/) for mineral identification. Normally 3 peaks are required for precise identification of a particular mineral.

Sample preparation

- The rock samples were first observed visually and a smaller sub-sample representative of the whole sample was chosen. The smaller sample was placed in a metal container and manually crushed using a hammer and pestle and transferred into a new container for powdering. After powdering the samples were transferred into airtight plastic sample holders. All equipment was cleaned with water and rectified alcohol in between each sample preparation.

- After initial powdering, the samples were micronized using a McCrone micronizing mill. The mill uses 48 corundum or agate elements to reduce the grain size to < 5 µm. Between 3.2 and 3.5 grams of the powdered rock sample was added to the container together with 8 ml of rectified alcohol. The sample was then run in the mill for 12 minutes, before taken out and flushed into new plastic sample holders using rectified alcohol. Samples were then placed in a heating cabinet until dry.

- After drying the micronized samples were transferred to XRD sample holders and flattened using a glass plate. All the while taking care to compact them to an even surface without orienting grains in a preferred direction by twisting the plate.

A total of 16 rock samples were crushed and micronized, analyses were done by Beyene Girma Haile with a Bruker D8 Advance at the Institute for Geosciences, University of Oslo. The instrument uses a 2.2 kW Cu Kα radiation source (wavelength λ=1.5418 å).

Raw data analysis

Initial X-ray diffraction analyses were done with Diffrac.Eva by Bruker Software (www.bruker.com). The diffractograms were imported and the Kα2 peaks were filtered out using the built-in software. Minerals were identified using the automatic peak search feature, and any remaining peaks were identified manually. The program was used for semi-quantitative analysis of the mineral content.

For a more accurate quantification of mineral content in the rock samples, Siroquant by Sietronics was used (www.siroquant.com). The program allows the user to import a diffractogram and then add the previously identified mineral phases. The software then calculates a synthetic curve to match the added mineral phases, and employs the Rietveld method to fit the observed diffraction pattern and the synthetic pattern.

- First, the XRD raw data was imported

- The mineral phases identified in Diffrac.Eva was added.

- The synthetic curve was calculated and the difference between the patterns was then minimized through six refinement cycles (Table 5) , five of which were taken from Hillier (2000).

Table 5: List of refinement steps used in Siroquant. *Taken from Hillier (2000)

Stage	Cycles	Damping factor	Target
1*	6	0.4	Phase scales
2*	6	0.4	Phase scales + Instrument zero refinement
3*	6	0.8	Phase scales
4*	6	0.2	Half-widths
5*	6	0.2	Unit cell dimensions
6	6	0.4	Orientation

- The fit between the observed and calculated pattern was then evaluated based on the Global Chi Squared and R-factor values calculated and visual observation of the curve fit.

Potential errors

The sample preparation process includes some potential sources of error. Primarily, improper cleaning of equipment in between each sample can cause cross contamination. The alum shale samples contain a relatively large amount of organic carbon, and the equipment used in the micronizing was hard to clean without leaving some small amount of carbon. Selection of sub samples from the drill cores was done purely by visual observation and the samples might not be completely representative of the original rock.

When placing the micronized samples in the XRD containers, they must be flattened. This is done using a small glass plate. If the plate is twisted to try and obtain a flat surface, some mineral grains like micas may obtain a preferred orientation causing an overestimation of the amount when using semi-quantitative analysis.

The sample holders in the McCrone micronizing mill are prone to leaking during the milling process. To prevent losing to much material, the sampling container was placed underneath to collect any material leaking out. This may lead to some of the material in the final sample not being properly micronized.

3.4.2 Scanning electron microscopy (SEM)

A scanning electron microscope produces magnified images by use of electrons instead of visible light such as a regular microscope. This allows for a much higher magnification of the sample being viewed. A SEM works by focusing a beam of electrons towards the sample surface, the electron beam interacts with the atoms in the sample producing secondary electrons (SE), back-scattered electrons (BSE) and X-rays (Nesse, 2012). For this method, BSE was employed together with energy dispersive X-ray spectroscopy (EDS). The purpose of SEM was to identify the mineral phases present in the samples, and use EDS to investigate the elemental composition of the minerals. Focus was specifically on finding trace elements and which minerals they were associated with. Mapping was used to get a more general idea of the bulk mineralogical composition. For the bulk mineralogical composition, some assumptions were used:

- Areas with overlapping K, Si, O and Al represent mica. Any areas with more intense K concentrations represents K-feldspar.

- Areas with high Si concentrations, but no Al, Na, Ca or K represents quartz.

- Areas with high Na concentrations represent albite.

- S is representative of sulfides, mainly pyrite and pyrrhotite.

The equipment used was a Hitachi SU5000 FE-SEM (Schottky FEG) and Dual Bruker XFlash30 EDS system and HR EBSD system with Argus, running on Quantax 800. The analysis was performed at the Institute for Geosciences, University of Oslo together with Håkon Børresen and senior engineer Berit Løken Berg.

3.5 Reaction modelling with PHREEQC

The purpose of using PHREEQC for reaction modelling was to assess the long-term behavior of alum shale in contact with oxygen and water. The reaction was modelled as a batch reaction with no transport.

Pyrite oxidation

Pyrite oxidation is included in most of the available PHREEQC databases (LLNL, PHREEQC, MINTEQ, minteq.v4), but only oxidation by O_2 is included through equation 2.2.3. Oxidation by Fe^{3+} in aerobic and anaerobic conditions had to be added using PHREEQCs RATES function which allows the user to define a mathematical rate expression for kinetic reactions. Pyrite oxidation rate was implemented based on Williamson and Rimstidt (1994), using parts of the code from example 9.9 in Appelo and Postma (2005). The reaction parameters for the pyrite oxidation, such as the starting concentrations, time steps and solver options for the set of kinetic equations (Ordinary Differential Equations) were then defined using the KINETICS function.

Mineral phases

To model the mineral phases present in the alum shale, the EQUILIBRIUM_PHASES function in PHREEQC was used. The function allows the user to define pure mineral phases that can react with the aqueous phase. The user can define a target saturation index, allow the mineral phase to react to equilibrium or until the amount of the phase in assemblage is completely dissolved. The reactions are reversible, so the function also allows minerals to precipitate when the solution becomes saturated unless the user doesn't allow it.

Some assumptions had to be made when defining the mineral assemblage. For the major mineral constituents, the XRD data was used. 1 kg of shale material was assumed, and the weight % for each mineral from the XRD was used to calculate the amount. Molecular weight for each mineral was then used to calculate the amount of moles. For the trace metals, a different approach was used. The ICP-MS and extraction data from Fjermestad (2013) were combined. E.g. extraction gives an indication that 50 % of Zn is bound in sulfides. The total amount of Zn in the shale was then multiplied by 0.5 and the resulting amount is considered as Zn bound in sphalerite. For uranium, an apatite phase where 10 % of Ca had been replaced by U was defined. The kinetic reaction rates of Sphalerite and U-apatite were defined using the RATES function, where a 1st order simplified rate law was applied according to eq. 2.2.15.

4 Results

4.1 X-ray powder diffraction

This section presents the results of the XRD analyses. Overall the samples mainly consist of quartz, mica, calcite, feldspars and sulfides. Three different feldspars were detected in the samples by Diffrac.Eva, albite and the K-feldspars microcline and orthoclase. Three different sulfides were detected, pyrite, pyrrhotite and chalcopyrite.

4.1.1 Alum shale (A1, A3, AT1, AT2, AT3K, AT4K)

The alum shale samples from the tunnel and the roadcut consist mostly of quartz and mica, from 22 – 32 and 13 - 29 wt. % respectively (Figure 9). Feldspar (microcline) was detected in all samples from 8 – 30 wt. %. Calcite was detected in both the roadcut samples (A1 and A3) and in one tunnel sample (AT1). All samples contain a relatively large amount of sulfides (20 – 31 wt. %). AT4K is the only sample where chalcopyrite was detected. All the alum shale samples can be characterized as shales from the bulk mineralogy.
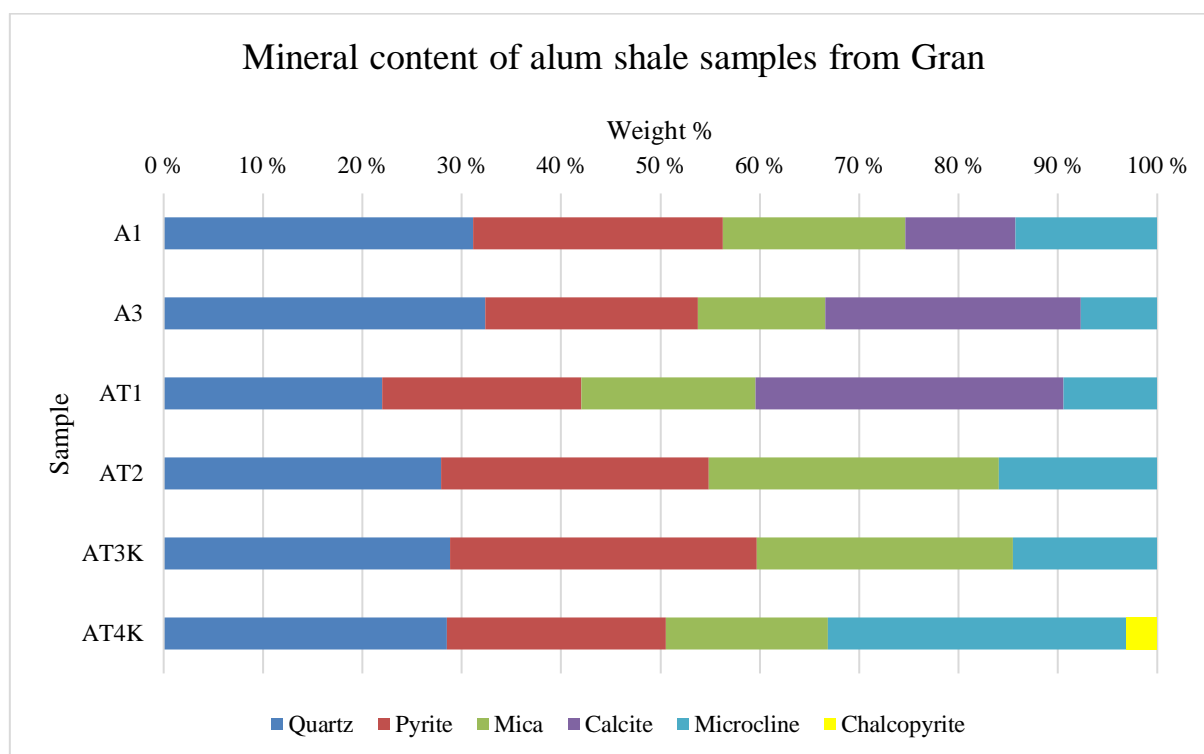
Figure 9: Mineral content detected by XRD in alum shale samples from Gran. Content is given as weight %.

4.1.2 Galgeberg shale (G1, G3K)

The mineralogical composition of the Galgeberg shale samples is shown in (Figure 10). Both samples contain quartz (28 and 35 wt. %), mica (44 – 62 wt. %) and feldspar (4 – 23 wt. %). The high content of mica in G3K might be an indicator of preferred orientation which will overestimate the content. G1 contained microcline, while albite was detected in G3K. A small amount of pyrite was detected in G1 (5 wt. %). From the bulk mineralogy, both samples can be characterized as shales.
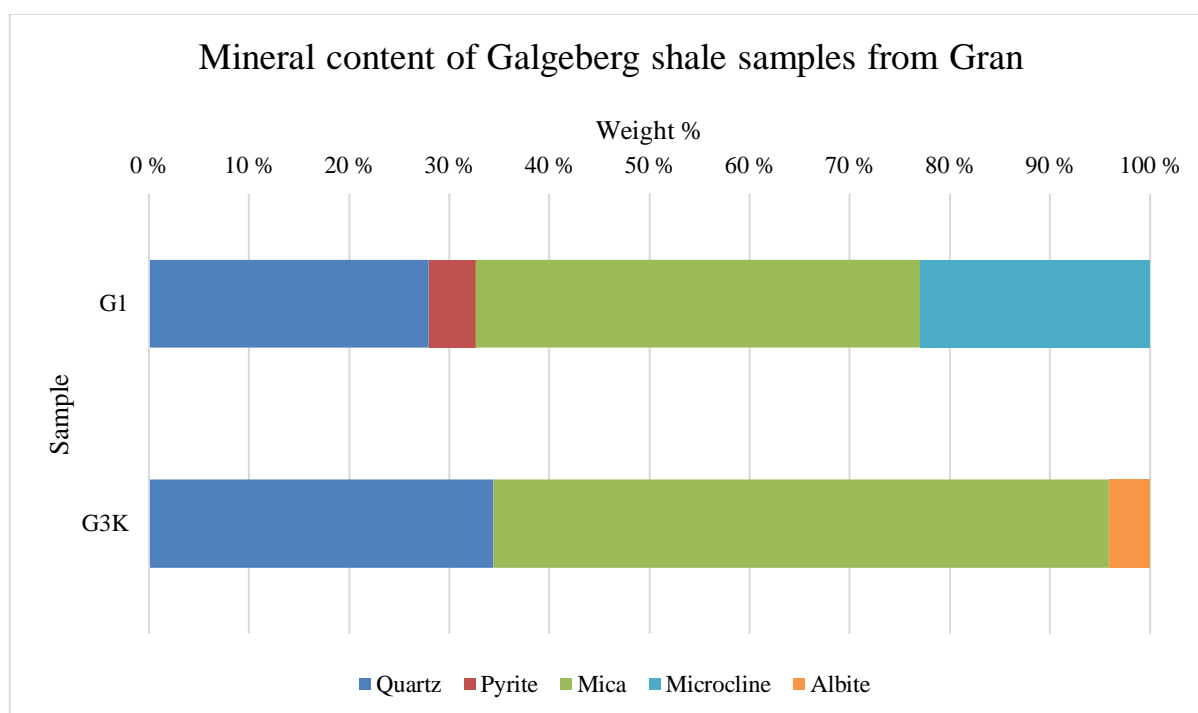
Figure 10: Mineral content detected by XRD in Galgeberg shale samples from Gran. Content is given as weight %.

4.1.3 Core samples (BH1N and BH2S)

Borehole 1 (BH1N)

The samples from borehole 1 display a varying mineralogical composition (Figure 11). BH1N – 8 m contains 95 wt. % calcite and 5 wt. % quartz, and is significantly different from the other samples from this core. The top three samples all contain quartz, mica, feldspar and sulfides. BH1N – 7 m and BH1N - 3 m differs from the other two samples as they contain pyrrhotite. BH1N – 3 m contains chalcopyrite (around 1 - 2 wt. %), but no calcite.

The top three samples (BH1N – 1, 3, and 7 m) can all be characterized as shales, while the bottom sample (BH1N – 8 m) is a limestone.
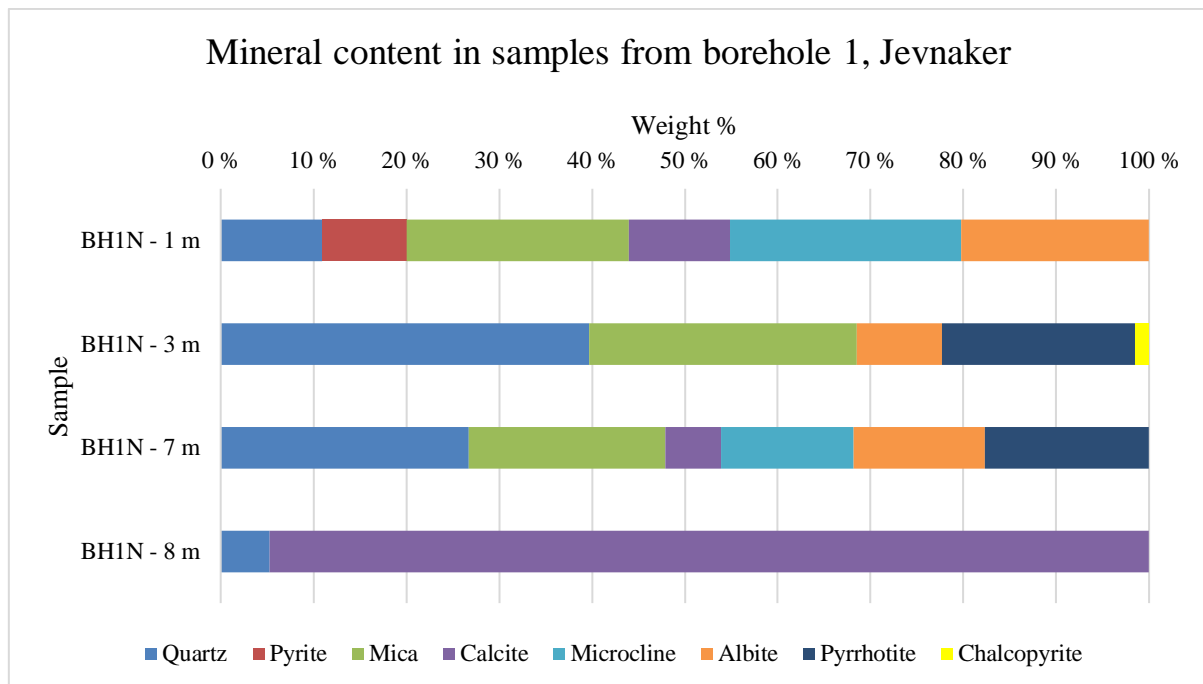
Figure 11: Mineral content detected by XRD in the samples from borehole 1, Jevnaker. Content given as weight %.

Borehole 2 (BH2S)

The four samples from borehole 2 show an increase in calcite content downwards (Figure 12). Sample BH2S – 1 m contains 47 wt. % mica, 36 wt. % quartz, 12.5 wt. % pyrite and 5 wt. % jarosite. BH2S – 5 m contains very little mica (3 - 4 wt. %) and is the only sample containing orthoclase. The two lowermost samples (BH2S – 9 m and 15 m) contain no mica minerals, but have a calcite content of 73 wt. % and 59 wt. % respectively. Both samples contain albite. Pyrite is found in the 1 m and 9 m sample (ca. 12 wt. % in both), while the two other samples contain about 9 wt. % pyrrhotite. Based on the mineral content, the sample from the top meter can be classified as a shale, while the three bottom samples are classified as "dirty" limestones.

Figure 13 shows a ternary plot of the quartz/feldspar/sulfide, carbonate and clay mineral content of each shale, illustrating the variation in bulk mineralogy. 12 of the samples plots towards the silica/feldspar/sulfide corner, seven of which contain no calcite. All the alum shale samples from Gran fall within this category. The Galgeberg shale samples and BH2S - 1 m are the most mica rich. The remaining four samples plot toward the calcite corner, with BH1N - 8 m as the

most carbonate rich, containing 95 wt. % calcite. All the samples from borehole 2 fall within the carbonate category except BH2S - 1m.
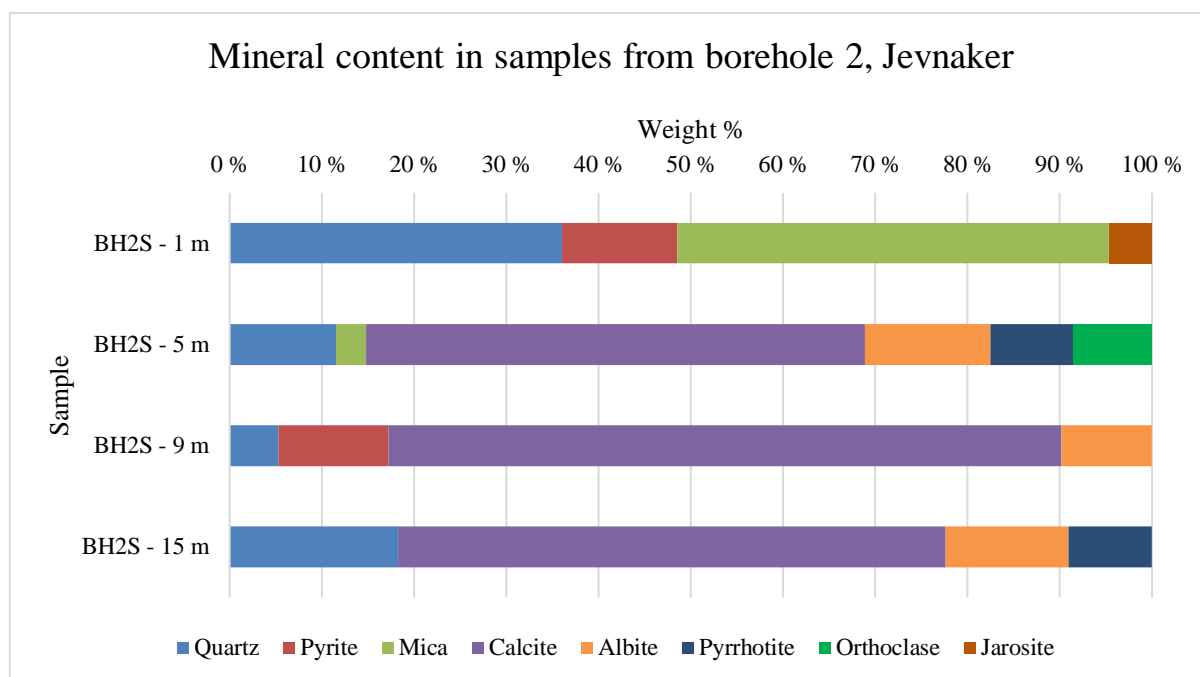
Figure 12: Mineral content detected by XRD in the samples from borehole 2, Jevnaker. Content is given as weight %.
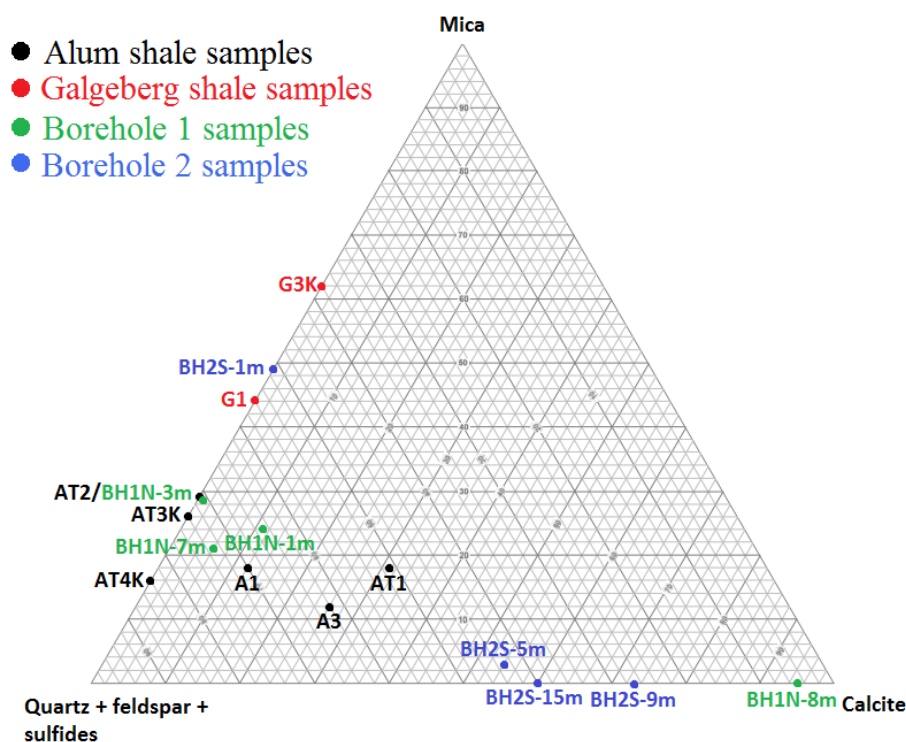
Figure 13: Ternary plot of the XRD results showing the variation in the bulk mineralogical composition of the different samples. The samples are plotted according to three categories based on the wt. % content of calcite, mica minerals and quartz + feldspar and sulfides. The Galgeberg, alum shale and borehole 1 samples generally show a shale composition, while the samples from borehole 2 are more indicative of a "dirty" limestone.

4.2 Scanning electron microscopy

Due to difficulties in producing good thin-sections from some of the shale samples, only the best samples were selected for SEM. Samples identified as limestones in XRD or through microscopy were discarded, this included BH2S – 5 m, BH2S - 15 m, BH1N - 8 m and BH1N - 1 m.

4.2.1 Alum shale (A1, A3, AT1, AT3K, AT4K)

Figure 14 shows a backscatter SEM image of sample AT3K. The image represents the typical appearance of the alum shale samples. Matrix minerals are mostly mica and quartz. Light grey larger mineral grains are either feldspar, calcite, quartz or large grains of mica. Pyrite is distributed throughout the matrix as either framboidal aggregates or euhedral grains, in the image they stand out as bright white. Some occasional small grains of other sulfides and heavier minerals were also found.
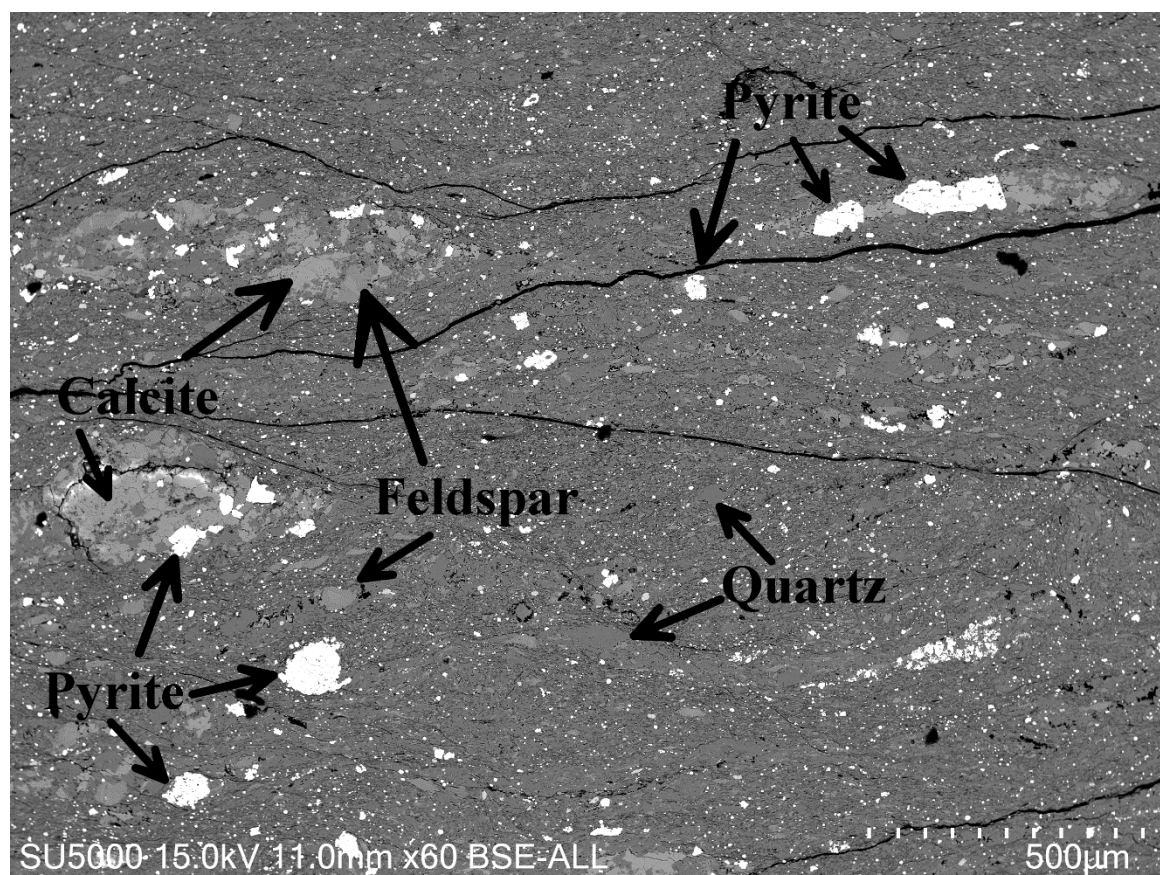
Figure 14: Representative backscatter image of sample AT3K with some of the main mineral constituents highlighted. Heavy minerals appear with a brighter color, exemplified by the pyrite grains in this image. Image taken at x60 magnification.

Figure 15 shows a mapping of S, Na, Si, Ca, K and P distribution in sample AT3K. Notice the distribution of Na and K, areas with high Na content likely represent albite, areas with high K content is likely K-feldspar, while the less intense areas are probably K bound in mica. S and Ca distribution correlate with the bright white and light grey areas in Figure 14 and represent pyrite and calcite crystals.
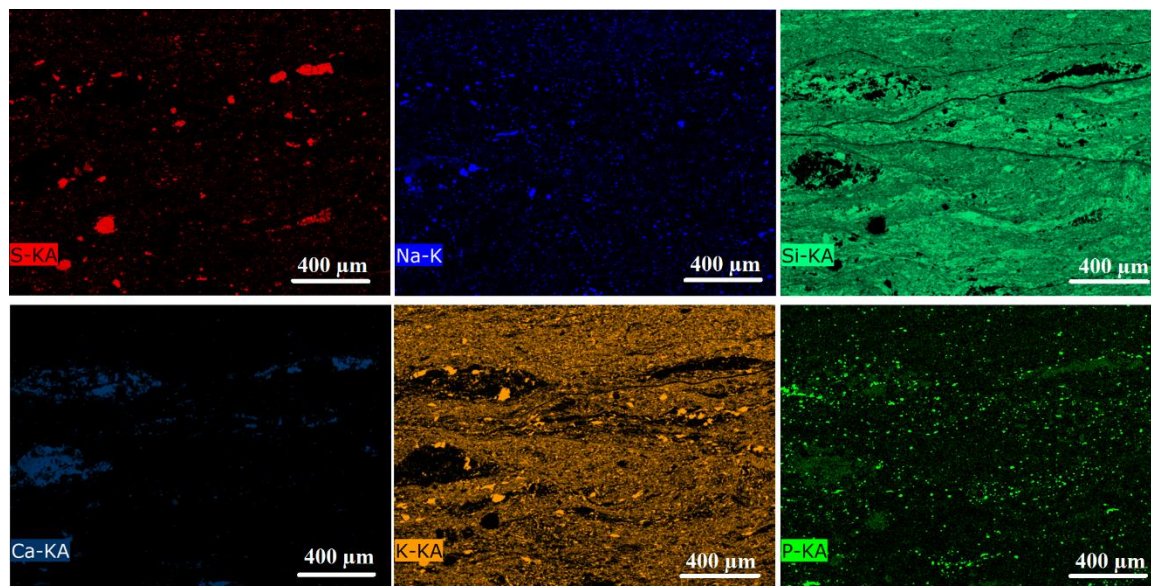
Figure 15: SEM mapping images of major elements in sample AT3K. Scale is the same as in Figure 14. Top left: S, Na and Si. Bottom left: Ca, K and P. Image taken at x500 magnification.

Figure 16 shows two backscatter images of sample AT1, the framboidal and euhedral pyrite (spectrum 2) grains typical for the alum shale samples are clearly visible. Baryte ($BaSO_4$) is shown in spectrum 1, occurring as needle like crystals forming thin lines in cracks in the shale matrix. Some Si, Al and K occur in the spectrum, but due to the size of the electron beam this is likely from the matrix grains around the mineral.

Sphalerite, a Zn sulfide (ZnS) was detected in all the samples from the tunnel (AT1, AT3K, AT4K). Figure 17 shows how sphalerite (spectrum 2) appears as brighter colored areas included in pyrite crystals (spectrum 1). The spectrum indicates that the sphalerite contains a small amount of Cd. This was the case for all the sphalerite grains analyzed in the alum shale samples. Quantification of two grains was performed and gave a Cd content of 0.4 - 0.5 atomic %, while Zn content was at 48 atomic %.
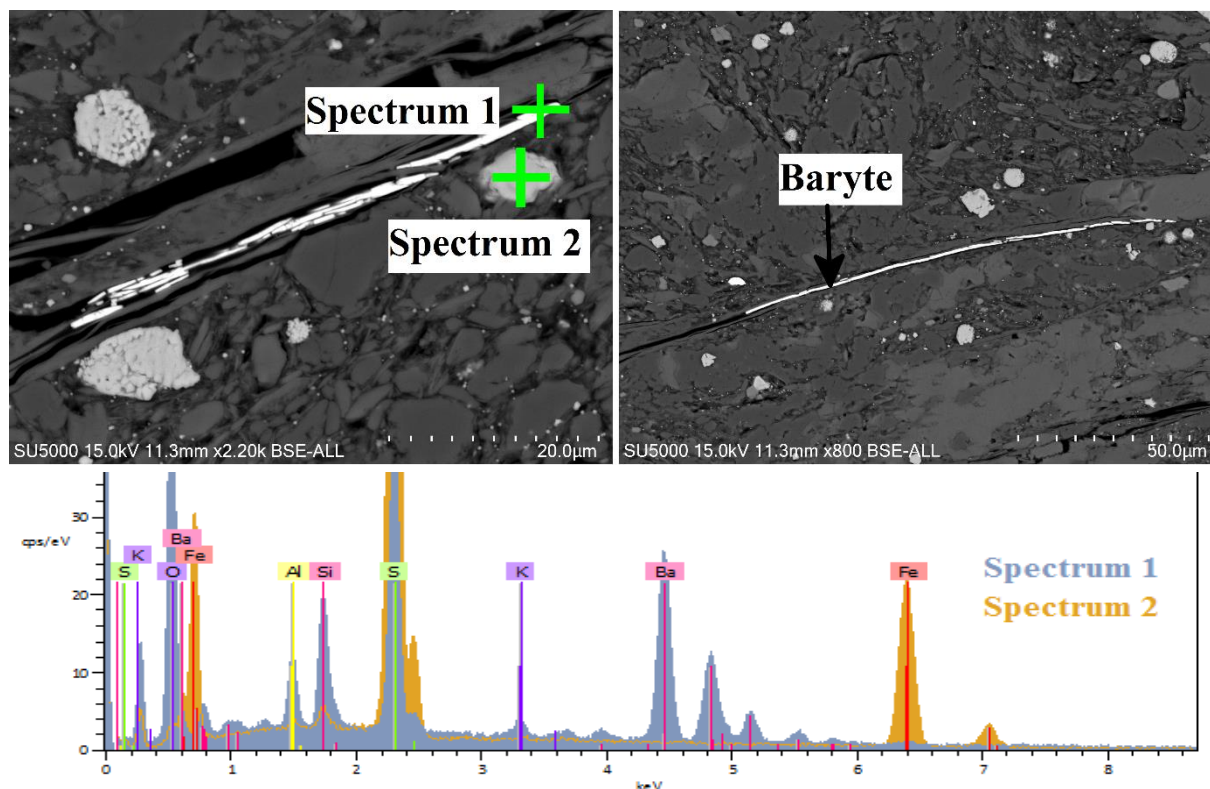
Figure 16: Backscatter images and two mineral spectra from sample AT1. Spectrum 1 has large peaks for Ba, S and O indicating baryte. Spectrum 2 has large peaks from Fe and S indicating pyrite. The right image is from a different part of the sample, and also shows baryte occurring in veins. Note different magnification in the images, x2200 in the left, and x800 in the right.
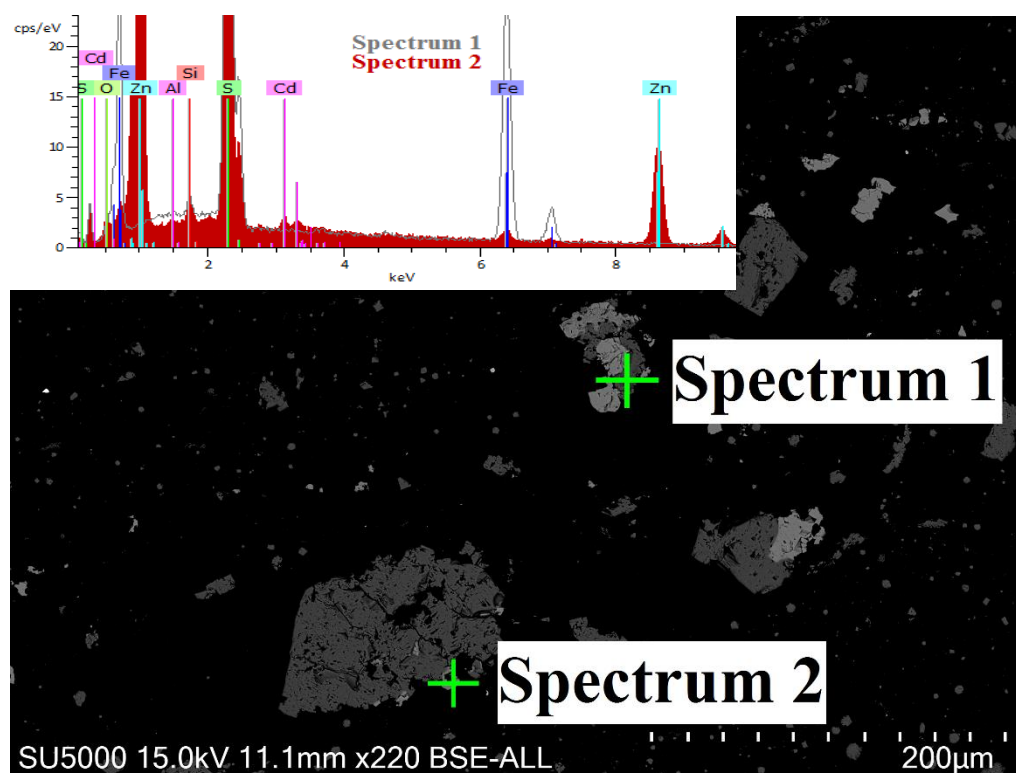
Figure 17: Cd bearing sphalerite in pyrite crystals from AT4K. Spectrum 1 shows large peaks for Fe and S, indicating pyrite. Spectrum 2 displays large peaks for Zn, S and a small peak for Cd, indicating sphalerite. Image taken at x220 magnification.
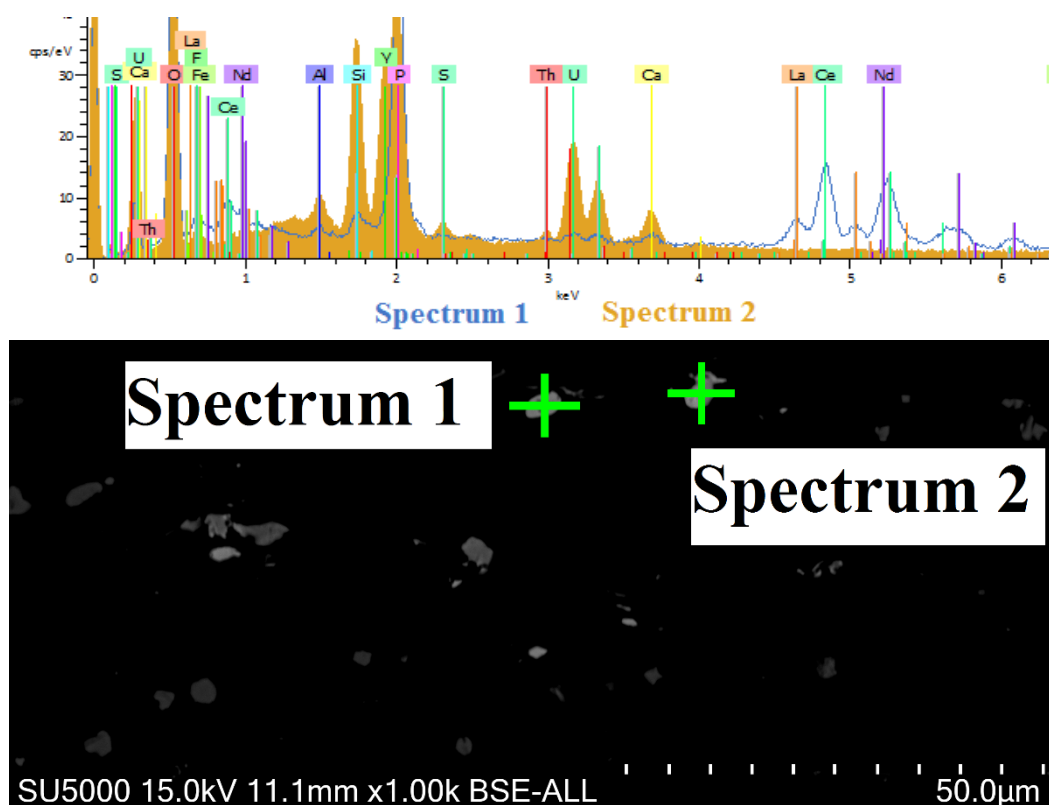
Figure 18: Non-Th/U bearing monazite (spectrum 1) and an unknown U-bearing phosphate or phosphate-associated phase (spectrum 2) in sample AT4K. Notice how spectrum 1 and 2 are quite similar, but spectrum 1 lacks the U and Y peak and spectrum 2 lacks the La, Ce, and Nd peaks Image taken at x1000 magnification.

Some heavier minerals were found in the samples, the most common being monazite ((Ce, La, Nd, Th)PO_4) shown as spectrum 1 in Figure 18. The monazite grains are rich in REE and the quantified grains contain (in atomic %) 3 – 7 % La, 8 – 10 % Ce, 2 – 5 % Nd and U and Th between 0 and 2.5 % (Table 6). An unidentified U-bearing phosphate/phosphate-associated phase (Figure 18, spectrum 2) was found in A3, AT1 and AT4K. Notice how the lanthanide peaks are lacking compared to the monazite spectrum. The U-bearing phosphate/phosphate-associated phase contains much more U (3.93 – 18.59 atomic %) compared to the monazite (0.2 – 0.26 %).

Table 6: Summary of the chemical composition of monazite and U-phosphate/phosphate-associated phase crystals in alum shale samples. All units in atomic %.

Mineral	O	F	Al	Si	P	S	Ca	Fe	Y	La	Ce	Nd	Th	U
Monazite	63.47	-	-	1.28	16.67	-	0.69	-	-	4.45	9.62	3.57	-	0.26
Monazite	62.68	-	0.44	1.18	16.61	-	0.87	-	-	4.66	9.54	3.57	0.27	0.2
Monazite	62.4	-	-	1.67	16.5	-	1.45	-	-	5.01	9.07	2.87	1.04	-
Monazite	62.17	-	0.8	1.78	16.4	-	-	-	-	6.69	8.44	3.54	0.19	-
Monazite	64.74	-	0.05	0.91	14.5	-	-	-	-	5.23	9.77	4.22	0.57	-
Monazite	62.65	-	0.38	1.36	17.41		0.53	-	-	4.85	8.79	3.41	0.61	-
Monazite	60.61	-	0.76	7.44	14.88	-	0.83	-	-	3.26	8.12	3.79	-	0.31
Monazite	62.43	-	0.69	1.57	17.87	-	0.84	-	-	3.14	8.58	4.52	-	0.36
U-phosphate	22.16	-	2.54	10.59	5.07	-	2.56	1.15	-	-	-	-	-	18.69
U-phosphate	64.62	-	1.7	7.62	5.5	0.65	3.82	3.35	4.71	-	-	-	0.78	7.25
U-phosphate	61.74	2.92	2.14	8.55	8.14	0.87	3.6	1.77	6	-	-	-	0.33	3.93

4.2.2 Galgeberg shale

SEM analyses of the Galgeberg shale indicate that both samples mainly consist of quartz, mica and feldspar. The samples are both low in calcite, and most of the Ca is associated with P in apatite. Both samples contain sulfides, mainly pyrite in both euhedral and framboidal form (exemplified in Figure 19a and 20a). The sulfides appear to be more concentrated in aggregates/crystals as shown in Figure 20a rather than finely distributed throughout the shale matrix. Sample G3K has numerous cracks, many of which seem to have occurred along weakened weathering zones, it is also covered with small "cavities" (Figure 19b), the origin of which are uncertain. The edges of the weathering zones contain iron oxides together with baryte, rutile and sulfides (Figure 20b and 21)
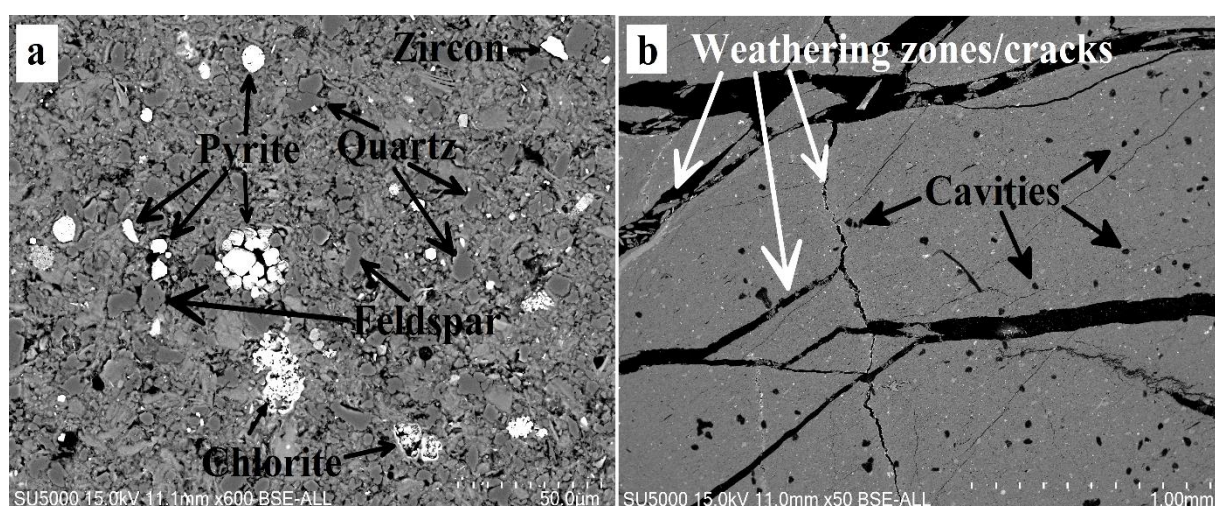
Figure 19: a) Representative backscatter images of G2, showing the distribution of pyrite, feldspar, quartz and chlorite. **b):** Backscatter image of G3K showing cracks, weathering zones and cavities. Images taken at x600 (a) and x50 (b).
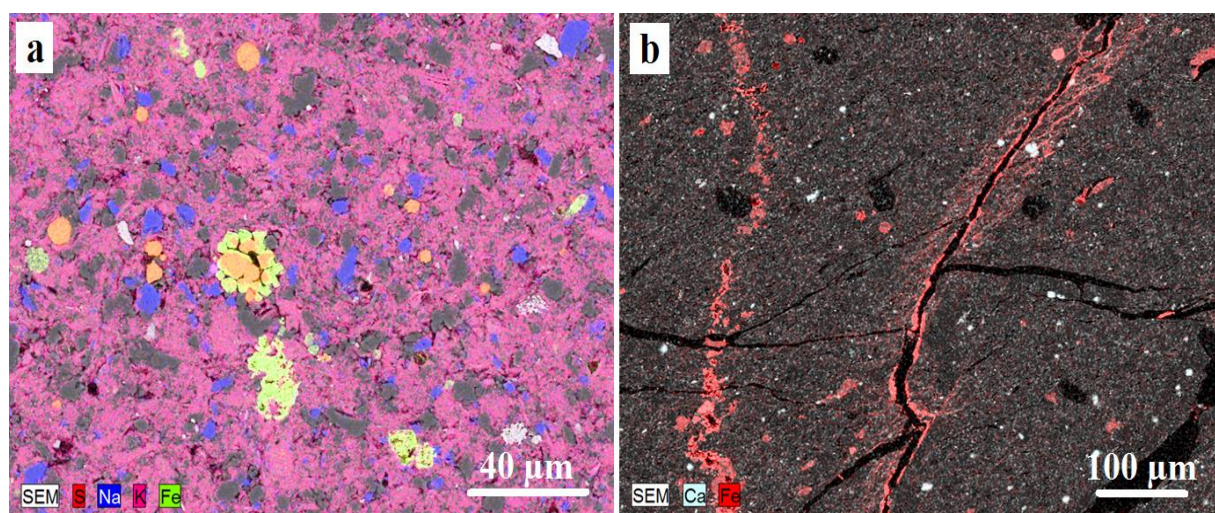
Figure 20: a) Mapping of sample G2, showing the distribution of S (red), Na (blue), K (pink) and Fe (green). S is representative of pyrite. Areas with high Na shows the distribution of albite. Fe not associated with S is Fe-oxides or chlorite. Grey areas are quartz. **b)** Mapping of sample G3K showing the distribution of Fe (red) in iron oxides along the edges of a fracture. Images taken at x600 (a) and x110 (b) magnification.

Monazite was found in both samples, occurring as tiny grains distributed in the shale matrix. Another REE containing mineral, xenotime (YPO_4) was found in sample G2, occurring as a brighter area on a zircon (appendix IV-II).
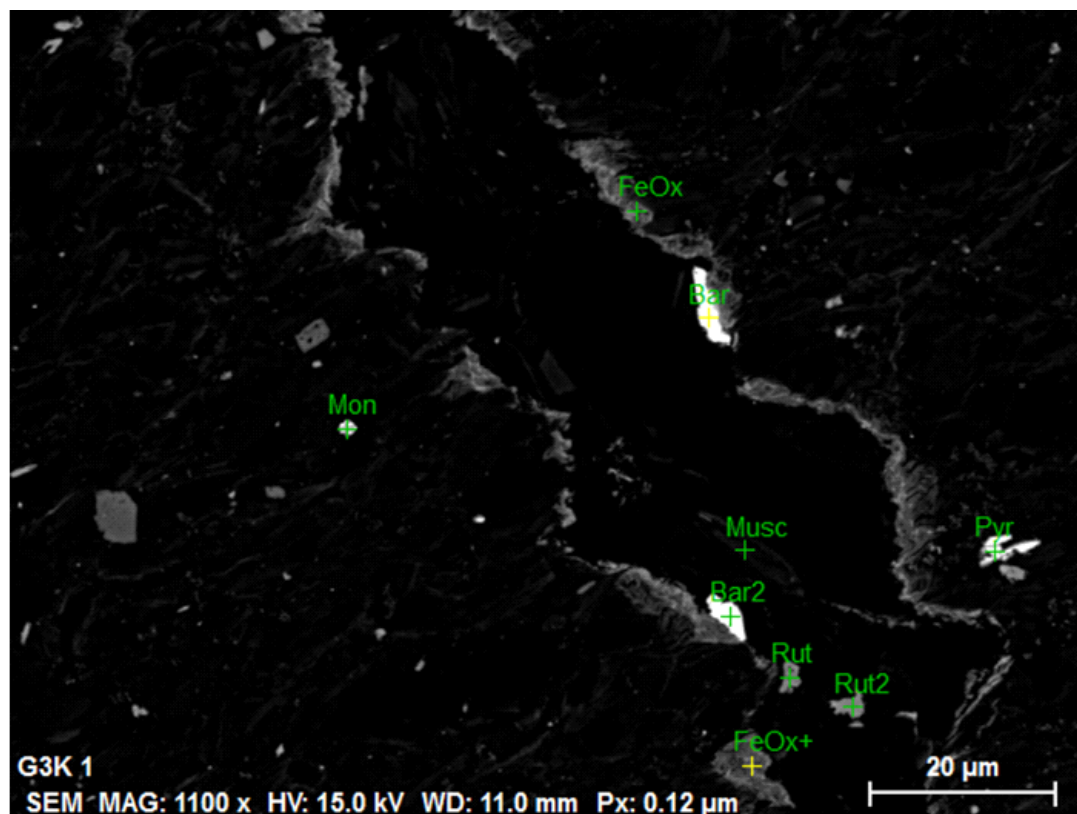
Spec.	O	Na	Mg	Al	Si	P	S	K	Ca	Ti	Fe	Sr	Ba	La	Ce	Nd	Mineral
Mon	60.41	-	0.52	3.75	6.81	9.55	-	1.03	11.55	-	0.78	-	-	1.32	2.24	1.11	Monazite
Bar	64.00	0.68	-	0.54	0.94	-	14.55	0.55	0.75	-	-	2.44	15.25	-	-	-	Baryte
FeOx	55.28	-	3.94	4.16	10.37	-	0.19	0.39	0.33	-	22.34	-	-	-	-	-	Fe-oxide
Bar2	61.17	0.45	-	0.45	1.11	-	16.54	-	0.31	-	1.2	2.03	16.23	-	-	-	Baryte
Musc	60.62	-	1.29	12.91	18.68	-	-	4.94	-	-	1.55	-	-	-	-	-	Muscovite
Rut	66.05	-	-	1.64	2.43	-	-	0.4	-	29.12	0.37	-	-	-	-	-	Rutile
FeOx+	61.04	-	3.55	2.59	9.35	-	0.2	0.06	0.22	-	22.36	-	-	-	-	-	Fe-oxide
Rut2	68.25	-	-	-	0.54	-	-	-	-	31.21	-	-	-	-	-	-	Rutile
Pyr	21.9	-	-	1.04	1.49	-	35.73	-	-	-	39.54	-	-	-	-	-	Pyrite

Figure 21: Closeup of a crack with weathering zonation from sample G3K. The figure shows how Fe- and Ti-oxides and baryte occur along the edges of the crack. The chemical compositions of the minerals are listed in the table (unit is atomic %). Image taken at x1100 magnification.

Apart from pyrite, two other sulfides were found in the samples. Sphalerite was found in G2 (appendix IV-II), while a Cu-bearing sulfide identified as chalcopyrite ($CuFeS_2$) was found in both samples. In G2 the chalcopyrite was found as a small grain associated with a larger pyrite grain (Figure 22), while in G3K it was found as a larger massive crystal (appendix IV-II).

42
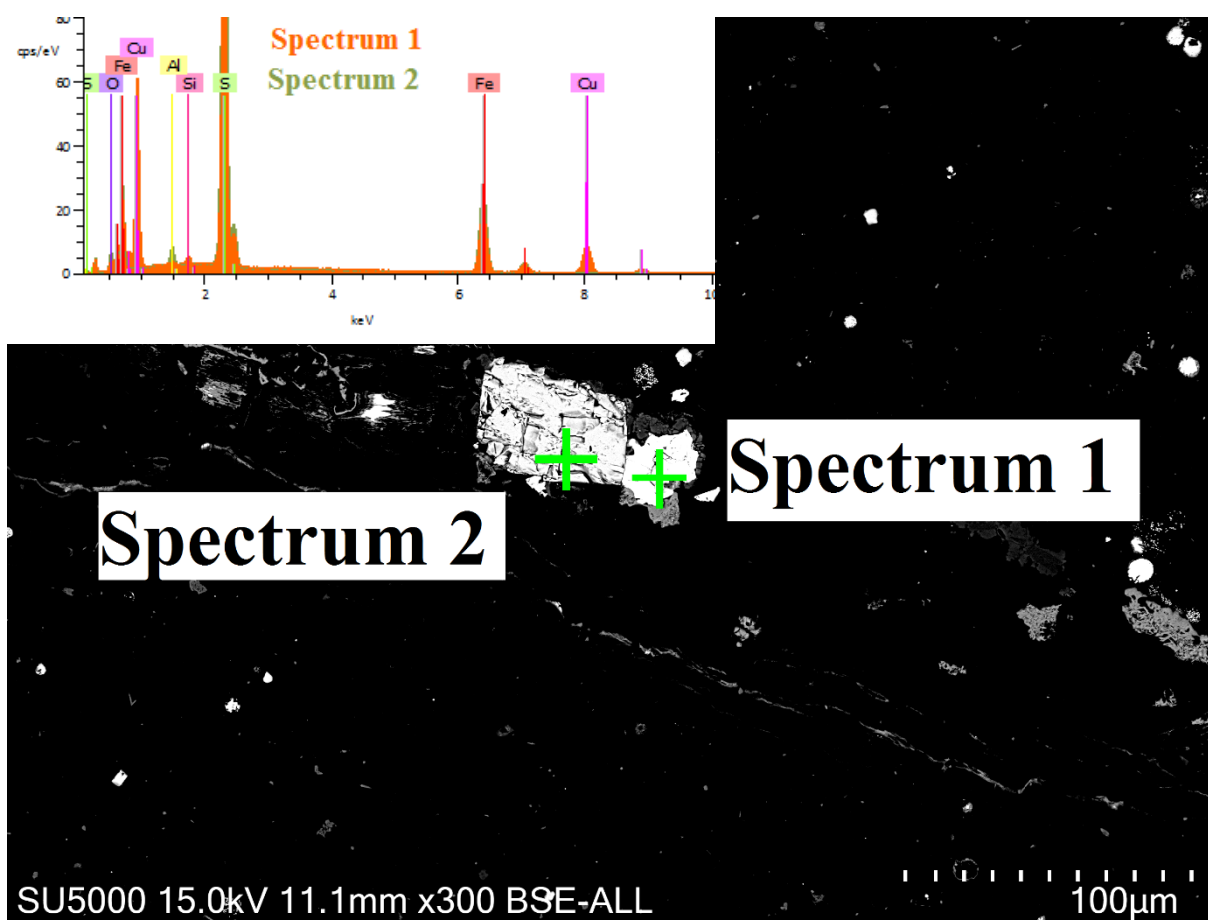
Figure 22: Chalcopyrite inclusion in pyrite crystal. Spectrum 1 shows large peaks for Fe, S and a small Cu peak, indicating chalcopyrite. Spectrum 2 is similar but lacks the Cu peak, indicating pyrite. Image taken at x300 magnification.

4.2.3 Borehole 1

BH1N - 8 m was not analyzed because both XRD (Figure 11) and reflected light microscopy (appendix IV-III) indicated that it was primarily limestone. BH1N - 1 m was characterized as shale in the XRD, but the sample that was used for the thin section only contained limestone (appendix IV-III).

Samples BH1N - 3 m and BH1N - 7 m were both similar in appearance with pyrite occurring as aggregates of massive pyrite in veins (indicated by Fe/S distribution in Figure 23b and d) or as clusters together with calcite (Figure 23a and c). The mappings (Figure 23c and d) indicate that the matrix minerals consist of mica, quartz and feldspar (albite and K-feldspar) (see appendix IV-IV for more mapping images). Two monosulfides were detected in the samples, lead sulfide (PbS) (Figure 24a) containing rhenium and selenium and a Co, As and Ni bearing sulfide identified as cobaltite (CoAsS) (Figure 24b). Both minerals occur as inclusions in larger pyrite crystals as shown in the figures.

U and Th bearing phosphates/phosphate-associated phases were detected in BH1N - 7 m, occurring both as small crystals in the shale matrix and as aggregates of small crystals included in a larger apatite crystal. Two of these apatites were analyzed and one is shown in Figure 25a. The aggregates contained some interesting minerals, a Pb, U and Ti bearing silicate or oxide (listed as unknown in the table in Figure 25), with U content at 17 atomic %. Allanite, a REE bearing silicate was detected in both samples, associated with pyrite grains (Figure 25b).
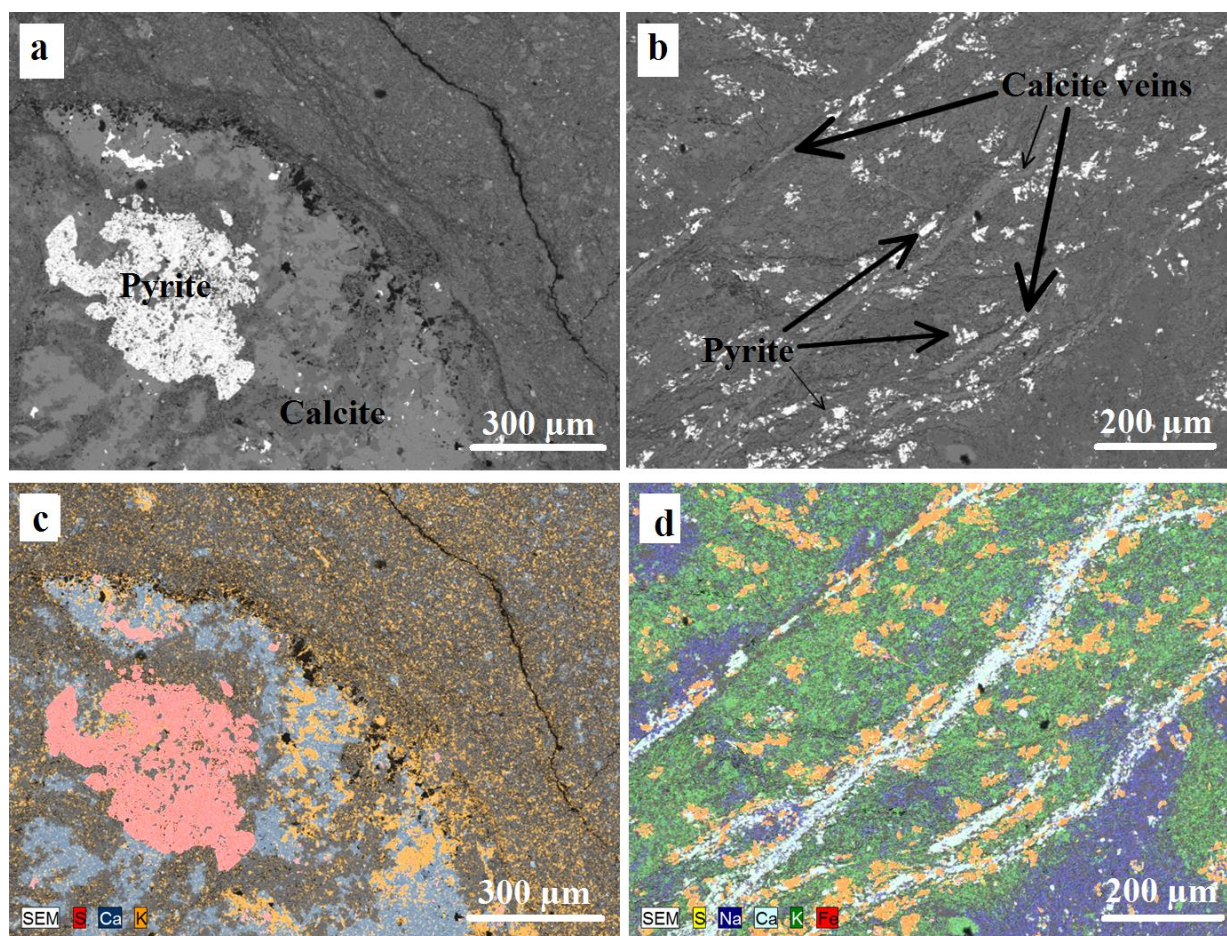
Figure 23: a) Backscatter image of BH1N-3m. **b)** Backscatter image of BH1N-7m. **c)** Element mapping of **a** showing S (red), Ca (blue) and K (orange). **d)** Element mapping of **b** showing S (yellow), Na (blue), Ca (light blue), K (green) and Fe (red). Images taken at x90 (a and c) and x110 (b and d) magnification.

Spec.	O	Al	Si	S	Fe	Re	Pb	Co	Ni	As	Mineral
1	9.53	0.44	-	43.03	12.8	2.36	31.84	-	-	-	Galena
2	3.88	-	0.58	60.64	34.89	-	-	-	-	-	Pyrite
3	4.08	-	0.65	48.01	47.26	-	-	-	-	-	Pyrrhotite
4	4.33	-	1.26	29.89	3.47	-	-	26.6	3.82	30.63	Arsenopyrite
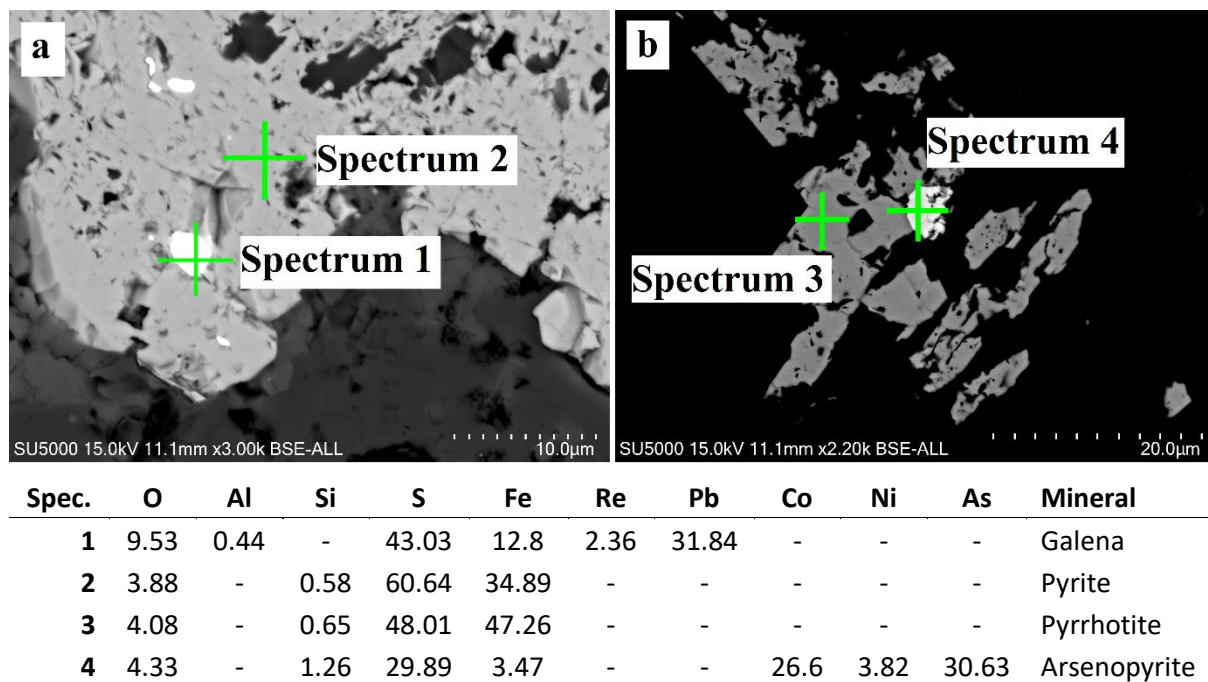
Figure 24: a) Galena inclusion in a pyrite crystal from sample BH1N-3 m. **b)** Arsenopyrite inclusion in a pyrite crystal from sample BH1N-7 m. Images taken at x3000 (a) and x2200 (b) magnification. The table in the figure shows the chemical composition of the different minerals.

Spec.	O	Al	Si	P	S	Ca	Ti	Fe	Pb	U	La	Ce	Nd	Mineral
1	67.96	1.38	6.73	2.1	-	-	1.07	2.29	1.2	17.26	-	-	-	U-oxide?
2	53.67	5.12	11.8	-	6.28	-	8.04	6.17	8.04	1.54	-	-	-	Unknown
3	3.47	-	-	-	48.17	-	-	48.36	-	-	-	-	-	Pyrrhotite
4	57.68	11.19	15.36	-	-	7.14	-	3.8	-	-	1.08	2.1	0.55	Allanite
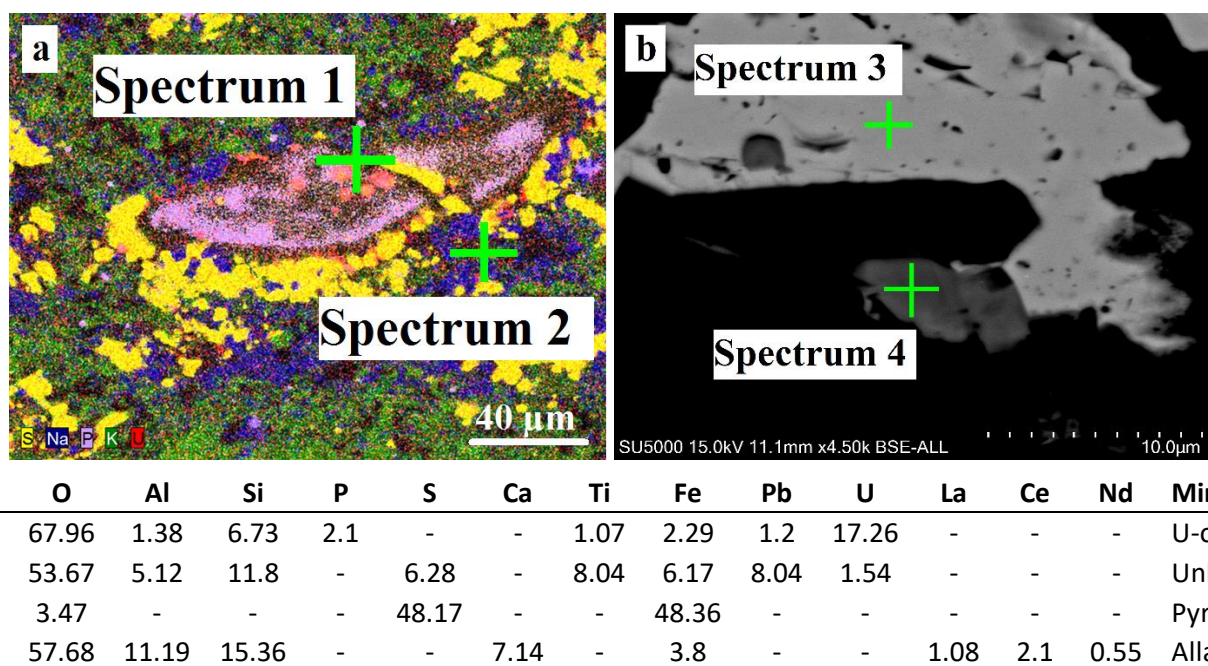
Figure 25: a) Mapping of S (yellow), Na (blue), K (green) and U (red) in a U-bearing apatite crystal in sample BH1N- 7 m. **b)** Allanite crystal attached to a larger pyrite crystal in sample BH1N - 3 m. Chemical composition of the different spectra listed in table below. Images taken at x600 (a) and x4500 (b) magnification.

The Fe:S ratio of all the pyrite grains quantified in BH1N – 3 and 7 m are listed in Table 7. Although the selection is small, all the iron sulfides quantified in BH1N – 7 m have an Fe:S ratio of 1, which indicate that they are pyrrhotite and not pyrite.

Table 7: List of S and Fe content of some pyrite crystals in samples BH1N - 3m and BH1N - 7 m.

Sample:	Fe (atomic %)	S (atomic %)	Fe:S	Mineral
BH1N 3m	48.36	48.17	1.0	Pyrrhotite
	34.89	60.64	0.6	Pyrite
BH1N 7m				
	43.35	44.47	1.0	Pyrrhotite
	47.26	48.01	1.0	Pyrrhotite
	46.31	47.55	1.0	Pyrrhotite
	47.42	47.86	1.0	Pyrrhotite
	46.53	48.02	1.0	Pyrrhotite
	45.02	43.07	1.0	Pyrrhotite

4.2.4 Borehole 2

BH2N - 5 m and BH2N - 15 m were not analyzed because both XRD (Figure 12) and reflected light microscopy (appendix IV-V) indicated that they were primarily limestone. BH2S – 9 m was classified as a limestone based on the XRD results, however both the reflected light microscopy and SEM showed a very different mineralogy with low calcite content.

Figure 26a and b show a representative selections of samples BH2N - 1 m and BH2N – 9 m. The matrix minerals consist mainly of quartz, mica and feldspar (see mapping in appendix IV-VI). In both samples sulfides occur in veins, (indicated by the S and Fe distributions in Figure 26c and d). In BH2S – 9 m the sulfide veins contain some calcite, which is not the case for BH2S – 1 m. In addition to pyrite, four different sulfides were found in the samples (appendix IV-VI). Sphalerite, arsenopyrite and chalcopyrite was found in BH2S – 1 m, while arsenopyrite and Se bearing galena was found in BH2S – 9 m. Four of the arsenopyrite crystals found contained Co at levels of 3.5 – 7.6 atomic %. It is not enough to classify them as cobaltite, instead they could be classified as danaite, a cobalt rich variety of arsenopyrite. All the sulfides except galena were found as inclusions in pyrite crystals. Monazite, allanite and U-bearing phosphate/phosphate-associated phase was found in BH2S – 1 m, but not in BH2S – 9 m.
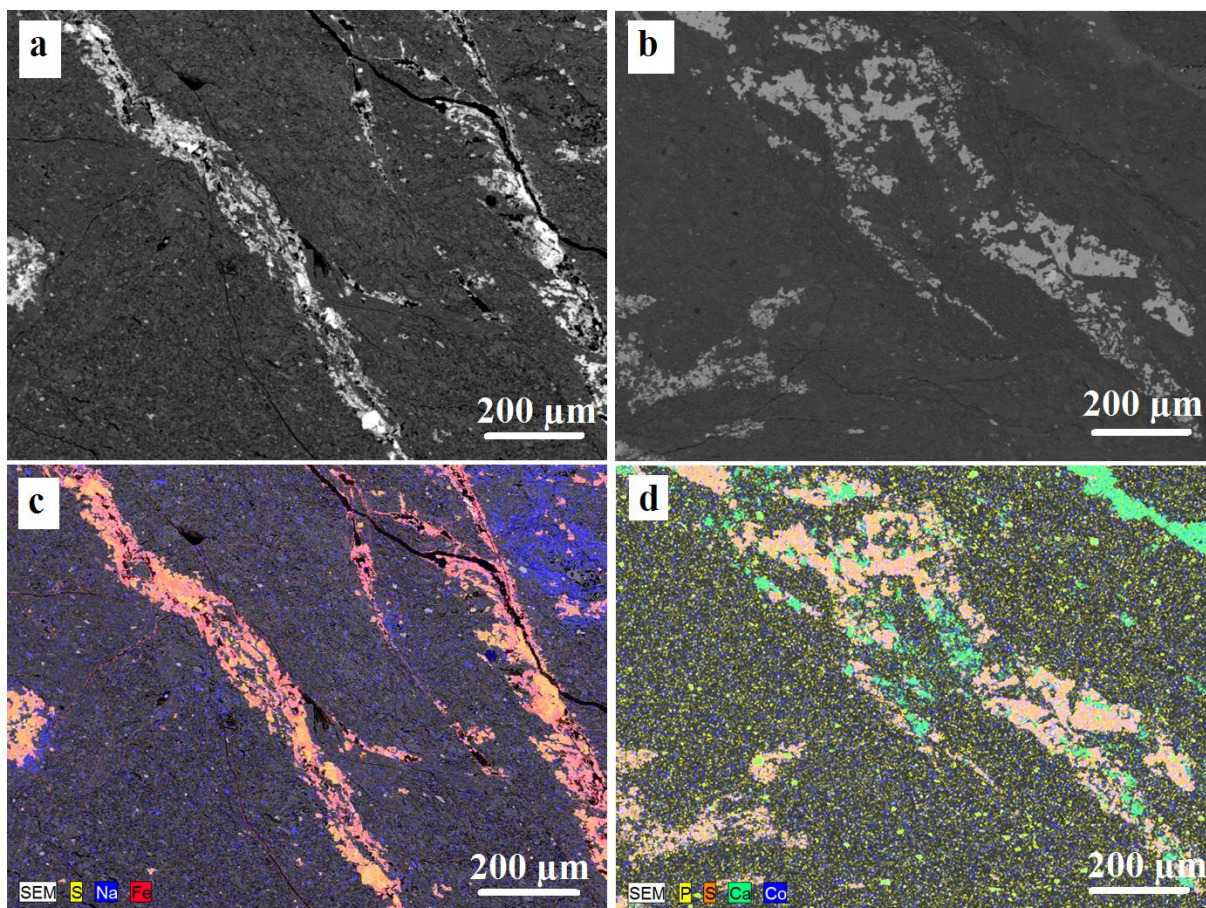
Figure 26: a) Backscatter image of sample BH2S - 1 m. **b)** Backscatter image of sample BH2S - 9 m. **c)** Element mapping of the area shown in (a), S (yellow), Na, (blue) and Fe (red). The pyrite veins can easily be distinguished from the Fe and S distribution. **d)** Element mapping of the area shown in (b), P (yellow), S (orange), Ca (green) and Co (blue). The Ca and S distributions easily identify the pyrite and calcite veins. Notice the P distribution indicated in yellow which is likely apatite and monazite grains.

4.3 Bulk experiment

4.3.1 Alum shale (A1, A2K, A3, AT1, AT2, AT3K, AT4K)

Tables 8 and 9 show the result of the ICP-MS analyses of the water samples from the alum shale containers. In the three experiments with alum shale from the roadcut (Table 8), Sr is the element with the highest concentration, averaging at 2500 – 6500 µg/l. U and Ni are relatively abundant with average concentrations of 530 – 1150 and 311 – 1150 µg/l respectively. Zn, Mo and Fe all have average concentrations above 100 µg/l. Al, Cr and Co concentrations are relatively low at around 5 – 37 µg/l, while the lowest concentrations are found for V. Pb. Mo, Co, U, Sr and Ni follow the same pattern, with the lowest concentrations in the period with least precipitation, and vice versa (illustrated by U in Figure 27). Al concentrations are stable irrelevant of precipitation. In sample A3, Fe, Cu and Cr concentrations are highest when the

precipitation is lowest (Figure 28), while Cd is opposite. For sample A1 the pattern is the exact opposite. Zn shows a general decrease in all samples.

In the four experiments with alum shale from the tunnel (Table 9) the elements with the highest concentrations are Sr, Zn and Ni which average from 3200 – 21600 µg/l. U, Cd, Co, and Fe concentrations are lower, averaging from 33 – 1200 µg/l. Al, V, Cr, Cu, Mo and Pb concentrations are low at 0.2 – 107 µg/l, with V and Pb averaging below 1 µg/l. Co, Cu, Cd, Ni, Zn, Mo, U and Sr concentrations all decrease towards the last sampling as illustrated by U in Figure 29. Fe and Cr both show low concentrations in the period with the least precipitation illustrated by Cr in Figure 29, while the behavior of Pb is the opposite. Th and Hg were below detection limit (< 0.004 and < 0.006 µg/l) in all samples.

Of the major cations and anions (Table 10 and Table 11) Ca and SO_4 are the most abundant in the water samples from containers A1 - A3. In the samples from the tunnel shale, SO_4 is still the most dominant anion, but for cations Mg levels are higher than the Ca levels. In general, the anion/cation concentrations are higher in the water samples from the tunnel shale.

The field measured pH levels are stable between 7 and 8 in the water samples from containers A1 - A3 with the highest values occurring in the period with least precipitation. The pH is slightly lower between 6.6 and 7.6 in the samples from AT1 - AT4K, increasing towards the last sampling (Table 10, 11 and Figure 27).
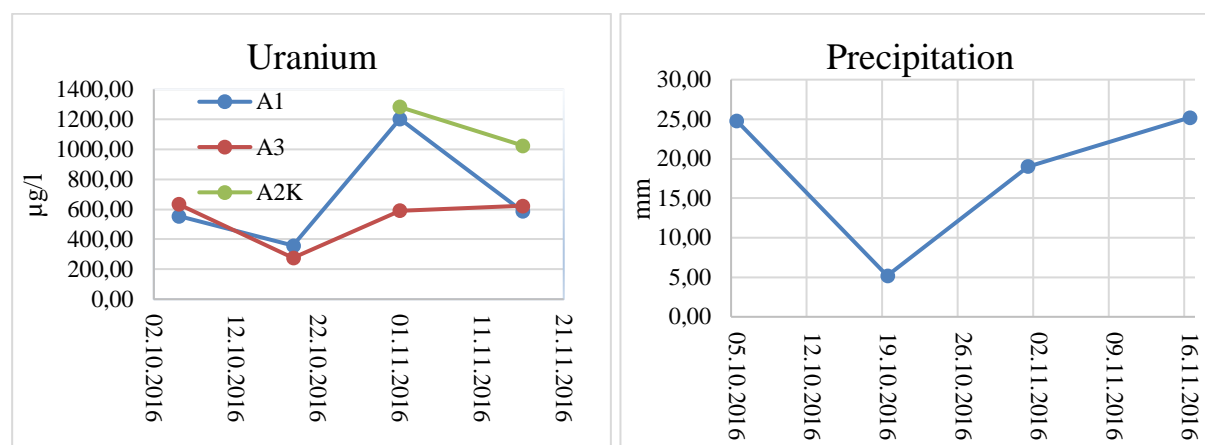
Figure 27: Plot of U concentration in samples A1, A3 and A2K and precipitation. Notice the lowest concentrations coinciding with the lowest precipitation. Cu, Cd, Co, Mo, Pb and Sr all follow the same pattern. Precipitation data taken from www.eklima.met.no
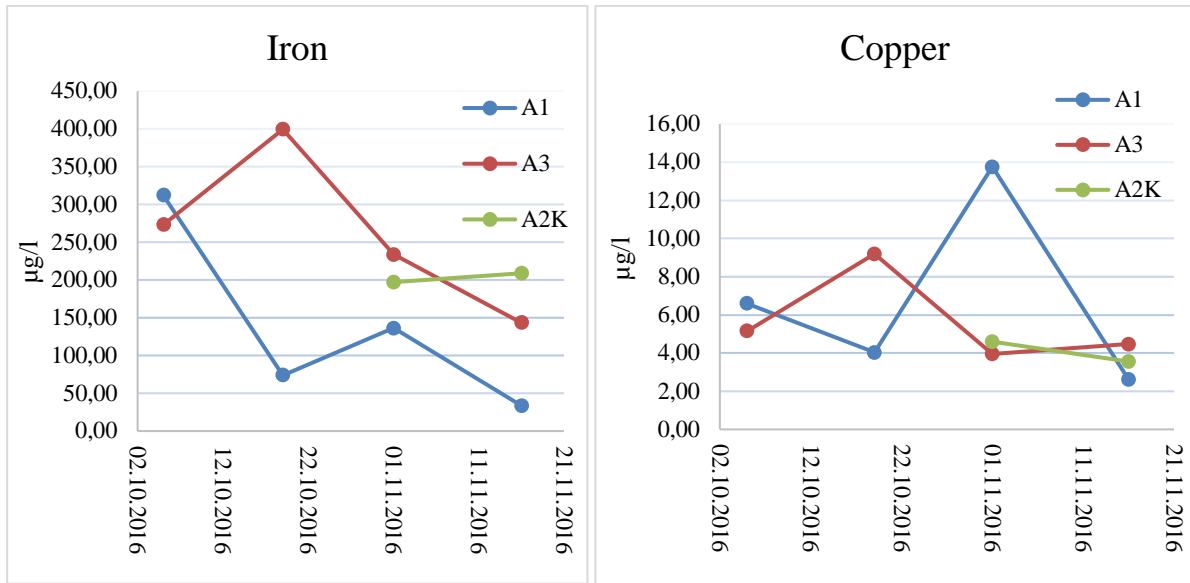
Figure 28: Plot of Fe and Cu concentrations from containers A1, A3 and A2K. Notice how the concentrations vary with the precipitation data in Figure 27.
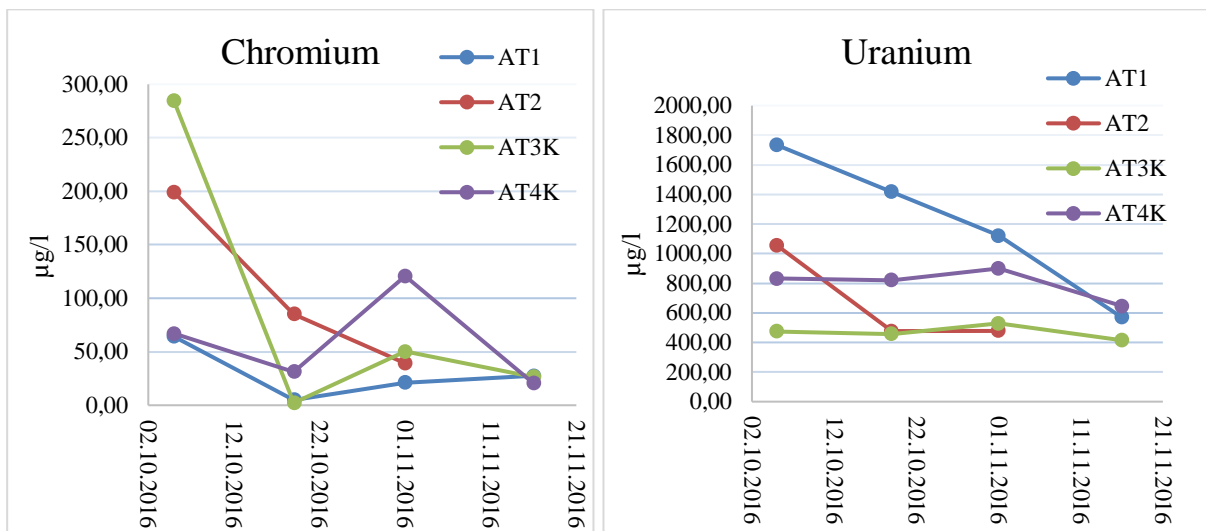
Figure 29: Plot of Cr and U concentrations in samples from containers AT1, AT2, AT3K and AT4K. Notice how the Cr concentrations vary with the precipitation shown in Figure 27, while U is steadily decreasing.

Table 8: Results from the QICP-MS analysis of water samples from the alum shale containers. All units in µg/l. ICP-MS detection limit in parenthesis (µg/l).

	Al (0.303)	V (0.005)	Cr (0.066)	Fe (1.990)	Co (0.012)	Ni (2.860)	Cu (0.015)	Zn (0.230)	Sr (0.130)	Mo (0.050)	Cd (0.002)	Pb (0.002)	U (0.020)
A1													
05.10.2016	44.2	0.51	105.9	312.4	3.7	362.2	6.6	594.4	2971.3	434.3	0.9	0.4	554.7
19.10.2016	25.4	0.10	19.2	73.9	2.3	210.5	4.0	201.9	1729.0	216.2	1.5	0.1	358.2
01.11.2016	23.2	0.07	25.2	136.2	2.6	385.9	13.8	56.6	3733.2	422.1	0.8	0.1	1202.7
16.11.2016	30.9	0.01	0.2	33.6	12.3	289.1	2.6	45.9	1657.9	351.3	0.9	0.5	585.4
A3													
05.10.2016	24.4	0.20	53.9	273.4	29.2	1492.1	5.2	186.3	9121.0	47.7	3.0	0.7	633.6
19.10.2016	26.0	0.47	137.2	399.4	5.5	749.5	9.2	174.7	4547.9	38.5	1.4	0.3	275.8
01.11.2016	27.9	0.13	56.9	233.6	30.8	1429.1	4.0	177.7	7262.1	32.1	2.8	0.1	591.5
16.11.2016	29.6	0.08	22.8	143.3	46.0	911.3	4.5	86.8	4939.6	40.4	1.7	0.1	622.4
A2K													
01.11.2016	27.2	0.06	13.0	197.1	4.4	765.3	4.6	70.9	6680.3	140.5	0.9	0.6	1281.9
16.11.2016	30.4	0.14	31.9	208.9	30.9	711.3	3.6	91.5	4526.3	92.9	1.2	0.1	1024.8

50

Table 9: Results from the QICP-MS analysis of water samples from the alum shale containers. All units in µg/l. ICP-MS detection limit in parenthesis (µg/l).

	Al (0.303)	V (0.005)	Cr (0.066)	Fe (1.990)	Co (0.012)	Ni (2.860)	Cu (0.015)	Zn (0.230)	Sr (0.130)	Mo (0.050)	Cd (0.002)	Pb (0.002)	U (0.020)
AT1													
05.10.2016	26.4	0.5	64.2	330.8	774.3	22441.1	17.0	22176.0	16331.7	61.1	409.4	0.2	1734.6
19.10.2016	46.3	0.3	4.9	81.7	620.4	18086.8	14.4	17619.9	12139.9	47.9	291.8	0.8	1417.2
01.11.2016	36.3	0.2	21.0	129.1	260.7	14280.0	22.3	13774.2	12163.4	26.2	263.1	0.2	1121.5
16.11.2016	52.9	0.1	27.4	161.6	155.3	7902.7	8.9	8264.9	7872.4	18.2	199.1	0.3	569.9
AT2													
05.10.2016	36.7	2.1	199.1	551.4	514.2	26684.7	112.2	34719.4	20804.3	29.4	737.3	0.5	1057.4
19.10.2016	28.6	2.2	85.3	247.7	233.4	12319.7	43.5	15923.3	9690.5	16.7	352.2	0.5	476.7
01.11.2016	31.1	2.1	39.2	133.2	218.2	11416.5	38.2	14262.5	8751.1	18.4	325.9	0.3	478.6
AT3K													
05.10.2016	30.9	1.0	284.4	967.9	110.8	8353.1	16.3	7429.1	11272.0	35.5	205.6	0.2	474.4
19.10.2016	31.6	0.1	2.2	83.2	104.0	7661.9	8.1	6963.0	10267.5	16.9	198.9	1.2	457.0
01.11.2016	55.5	0.2	50.1	311.5	89.5	11678.1	18.0	12968.8	10712.7	15.2	276.7	0.2	529.0
16.11.2016	38.6	0.1	26.4	165.6	56.7	4610.3	8.2	4822.9	5738.5	12.8	130.5	0.5	414.7
AT4K													
05.10.2016	31.6	0.4	67.0	263.5	47.9	4456.6	8.8	3673.8	12019.5	66.8	105.7	0.2	830.6
19.10.2016	29.2	0.3	31.2	152.1	47.2	4116.8	9.6	3380.8	9698.8	59.7	96.1	0.1	821.1
01.11.2016	31.7	0.6	120.8	396.5	19.3	5125.7	8.8	3659.1	11180.0	54.7	76.5	0.1	900.0
16.11.2016	29.3	0.1	20.4	134.1	19.7	2987.8	4.9	2357.6	6929.6	29.4	59.4	0.2	646.4

Table 10: Results from the anion/kation analysis of water samples from alum shale containers, and the pH measured in field. All units except pH is in mg/l.

	Na	K	Mg	Ca	F	Cl	SO4	pH
A1								
05.10.2016	1.0	12.1	8.0	261.0	0.15	12.1	623.3	7.73
19.10.2016	1.8	5.0	6.6	170.4	1.55	3.7	510.7	8.02
01.11.2016	1.9	6.0	14.2	379.1	0.09	3.2	1060.3	7.67
16.11.2016	1.5	3.0	5.1	175.3	0.65	3.0	4085.0	7.92
A3								
05.10.2016	4.6	14.1	78.2	605.5	0.19	0.5	1552.9	7.45
19.10.2016	2.9	8.9	36.0	308.0	n/a	4.7	854.2	8.05
01.11.2016	4.0	9.2	68.2	538.1	0.09	3.2	1451.9	7.7
16.11.2016	2.9	7.8	43.2	466.6	0.51	2.6	1414.4	7.68
A2K								
01.11.2016	4.1	12.0	122.4	475.7	0.59	3.8	1596.0	8.05
16.11.2016	3.2	8.7	111.6	419.0	n/a	2.6	1542.1	7.73

52

Table 11: Results from the anion/kation analysis of water samples from alum shale containers, and the pH measured in field. All units except pH is in mg/l.

	Date	Na	K	Mg	Ca	F	Cl	SO4	pH
AT1	05.10.2016	24.4	55.1	766.0	492.9	0.3	10.9	3931.1	7.19
	19.10.2016	20.7	113.3	683.5	416.8	2.0	132.6	7423.0	7.26
	01.11.2016	19.7	45.7	736.9	415.0	0.2	10.5	3697.7	7.02
	16.11.2016	10.0	24.1	321.8	391.3	0.6	4.0	2306.8	7.72
AT3K	05.10.2016	28.1	74.8	902.4	506.2	0.3	0.5	4576.6	6.66
	19.10.2016	13.1	61.1	484.7	316.6	1.9	46.3	5241.6	6.77
	01.11.2016	12.7	33.1	473.1	281.0	0.1	3.4	2533.8	7.30
AT2	05.10.2016	12.0	36.0	377.6	494.1	0.2	0.4	2631.5	6.74
	19.10.2016	12.0	35.5	381.9	430.8	1.7	3.4	4973.6	7.24
	01.11.2016	14.0	32.8	506.6	427.0	0.1	3.1	2952.2	7.34
	16.11.2016	2.7	7.3	79.2	342.5	0.5	2.5	1306.7	7.50
AT4K	05.10.2016	31.5	52.6	578.5	486.3	0.2	0.4	3137.2	7.05
	19.10.2016	28.6	49.2	572.7	403.8	1.7	3.8	6324.9	7.16
	01.11.2016	24.9	37.5	545.4	405.6	0.2	3.2	3031.1	7.44
	16.11.2016	10.2	24.1	226.0	397.9	0.7	2.7	1928.5	7.59

Statistical analysis

Table 12 shows the Spearman correlation matrix for the analysis results from A1, A2K and A3. Strong positive correlations (> 0.7) are marked in blue, moderately positive (> 0.5) are marked in green, while strong negative and moderately negative correlations are marked in red and yellow respectively. Correlations that have a p-value of 0.01 or lower are marked with one asterisk, while a p-value between 0.05 and 0.01 are marked with a double asterisk.

V, Cr and Fe all have a strong positive correlation with each other and a p-value less or equal to 0.01. Zn and K can also be included in this group. Zn has a strong positive correlation with V and a moderate positive correlation with Cr and Fe. K has a strong positive correlation with Fe and moderate positive correlation with V, Cr and Zn. All the moderate correlations have a p-value of more than 0.05.

Ni, Sr, Cd and Co all have a strong to moderate correlation with each other. Ni has a strong positive correlation with Sr ($p \leq 0.01$), a moderate positive correlation with Co ($p \leq 0.05$) and Cd ($p > 0.05$). Sr shows a moderately positive correlation with Co and Cd ($p > 0.05$). Sr and Ni correlate with all the large cations Na, K, Ca and Mg.

U shows a moderately positive correlation with all the large cations except K, as well as with SO_4. Only the correlation with Mg has a p-value less than 0.05.

Mo stands out as it is the only element for which all the correlations that have p-values ≤ 0.05 are negative. It has a strong negative correlation with Sr and Ni and a moderate negative correlation with Co.

Table 12: Spearman correlation matrix for water analysis results from containers A1, A2K and A3. Fluorine is not included due to missing data.

	Al	V	Cr	Fe	Co	Ni	Cu	Zn	Sr	Mo	Cd	Pb	U	Na	K	Mg	Ca	Cl	SO4	pH
Al	1																			
V	0.08	1																		
Cr	-0.02	0.9*	1																	
Fe	0.05	0.87*	0.9*	1																
Co	0.37	0.05	0.1	0.18	1															
Ni	-0.22	0.19	0.33	0.49	0.64**	1														
Cu	-0.52	0.36	0.48	0.45	-0.47	0.13	1													
Zn	0.01	0.81*	0.6	0.56	-0.18	0.04	0.16	1												
Sr	-0.32	0.21	0.33	0.52	0.5	0.98*	0.18	0.13	1											
Mo	0.15	-0.21	-0.35	-0.39	-0.66**	-0.75**	0.16	-0.09	-0.72**	1										
Cd	-0.19	0.25	0.19	0.2	0.55	0.6	-0.31	0.38	0.58	-0.78*	1									
Pb	0.22	0.13	0.04	0.38	0.15	0.35	-0.05	0.07	0.35	-0.07	0.13	1								
U	-0.21	-0.44	-0.36	-0.21	0.2	0.38	0.03	-0.5	0.41	0.09	-0.22	0.05	1							
Na	-0.41	0.07	0.14	0.36	0.44	0.84*	0.01	-0.02	0.9*	-0.67**	0.52	0.37	0.52	1						
K	-0.01	0.61	0.59	0.82*	0.14	0.64**	0.38	0.52	0.7**	-0.24	0.2	0.61	0.18	0.55	1					
Mg	-0.14	0.1	0.14	0.39	0.49	0.76**	0.01	-0.04	0.82*	-0.52	0.26	0.28	0.66**	0.89*	0.6	1				
Ca	-0.24	0.07	0.2	0.37	0.58	0.95*	0.07	-0.03	0.95*	-0.59	0.47	0.33	0.61	0.88*	0.64**	0.84*	1			
Cl	0.14	0.26	0.3	0.32	-0.64**	-0.39	0.36	0.31	0.25	-0.28	-0.48	0.03	-0.43	-0.35	0.16	-0.25	-0.44	1		
SO4	0.18	-0.5	-0.45	-0.21	0.49	0.37	-0.47	-0.6	-0.14	0.31	0.08	0.6	0.56	0.48	0.08	0.43	0.48	-0.5	1	
pH	0.22	-0.09	-0.17	-0.01	-0.34	-0.43	-0.15	-0.04	-0.04	-0.34	-0.27	0.16	-0.37	-0.16	-0.16	-0.11	-0.49	0.68**	-0.07	1

* p-value <0.05
** p-value <0.01

Strong negative
Moderate negative
Moderate positive
Strong positive

Table 13 shows the correlation matrix for water sample analyses from containers AT1, AT2, AT3K, AT4K. V has a strong positive correlation with Cr and Cu with $p \leq 0.01$. Cr has a strong positive correlation with Fe. Both V and Cr has a moderately negative correlation with pH.

Ni, Zn, Co, Cd and Cu all show a strong to moderate positive correlation with each other. Co only has a moderate correlation with Cu, but at 0.68 it borders with strong. All these elements show a moderate correlation with K and Mg.

Mo has a moderately positive correlation with Sr and U and a moderately negative correlation with Pb. Both U and Mo show a strong to moderate correlation with Na, K and Mg.

From the above described results, the trace elements can be divided into groups according to how they correlate with each other. The two suggested groups are:

1. V, Cr, Fe, Zn, Sr and Cu.
2. Ni, Zn, Sr, Co, Cu and Cd

Mo, U and Pb are treated separately as they only correlate with individual elements.

The large cations are not divided into the groups as the correlations are varied, but in general the elements in group one correlate with K, while the elements in group two correlate with Na, K, Ca and Mg.

Table 13: Spearman correlation matrix for water analysis results from containers AT1, AT2, AT3K and AT4K.

	Al	V	Cr	Fe	Co	Ni	Cu	Zn	Sr	Mo	Cd	Pb	U	Na	K	Mg	Ca	F	Cl	SO4	pH
Al	1																				
V	-0.44	1																			
Cr	-0.25	0.75*	1																		
Fe	-0.12	0.46	0.91*	1																	
Co	0.03	0.01	0.22	0.01	1																
Ni	0.16	0.33	0.43	0.22	-0.09	1															
Cu	-0.04	0.22	0.48	0.13	0.25	0.95*	1														
Zn	0.12	0.48	0.46	0.25	0.13	0.8*	0.8*	1													
Sr	0.01	0.38	0.34	0.3	0.08	0.65*	0.45	0.53**	1												
Mo	-0.41	0.34	0.3	0.15	-0.02	0.9*	-0.08	0.52**	0.57**	1											
Cd	0.02	0.52**	0.28	0.23	0.15	0.93**	0.85*	0.98*	0.53**	0.58**	1										
Pb	0.37	0.28	-0.41	-0.37	0.23	0.5	0.11	-0.1	0.47	-0.14	0.48	1									
U	-0.01	-0.2	0.21	0.02	0.3	0.42	0.24	0.45	-0.11	0.48	0.51	-0.26	1								
Na	-0.19	0.21	0.41	0.27	0.37	0.2	0.31	0.33	0.7*	0.75*	0.12	-0.44	0.69*	1							
K	-0.25	0.47	0.32	0.12	0.06	0.55**	0.5	0.14	0.71*	0.69*	0.21	0.03	0.62**	0.75*	1						
Mg	-0.05	0.59**	0.26	0.14	0.5	0.61**	0.55**	0.31	0.85*	0.89*	0.48	-0.14	0.83*	0.86*	0.83*	1					
Ca	0.04	0.42	0.33	0.45	0.24	0.35	0.09	0.24	0.81*	0.47	0.22	-0.07	0.37	0.46	0.43	0.54**	1				
F	-0.19	0.08	-0.41	-0.38	0.45	-0.12	-0.32	-0.05	-0.21	0	-0.09	0.43	-0.04	-0.12	0.27	-0.12	-0.14	1			
Cl	-0.11	-0.24	-0.38	-0.52**	0.08	0.42	0.29	0.43	-0.05	0.05	0.36	0.23	0.35	0.03	0.36	0.36	-0.36	0.41	1		
SO4	-0.21	0.27	-0.02	-0.19	0.4	0.4	0.32	0.37	0.37	0.35	0.34	0.16	0.42	0.03	0.62**	0.85*	0.31	-0.54**	0.48	1	
pH	0.37	-0.59**	-0.5	-0.31	-0.43	-0.45	-0.58**	-0.41	-0.65*	-0.31	-0.47	0.07	-0.17	-0.52**	-0.71*	-0.57**	-0.54**	0.03	0.07	-0.58*	1

Legend:
* p-value <0.01
** p-value <0.05

- Strong negative (red)
- Moderately negative (yellow)
- Moderately positive (green)
- Strong positive (blue)

57

4.3.2 Galgeberg shale

Table 14 and Table 15 show the result from the trace element- and anion/cation analysis of water samples from the Galgeberg shale containers.

Sr is the element with the highest concentrations (3409 – 9886 µg/l), followed by Ni (322 – 1227 µg/l) and Zn (336 – 1239 µg/l). The general pattern for these three trace elements is that the concentrations are highest in the first (5/10) and third (1/11) samplings as illustrated in Figure 30.

Fe and Mo both have concentrations above 100 mg/l. Mo concentrations are highest in the first and third sampling, while Fe concentrations are lowest in the first and last sampling (Figure 31).

Al, Cr, Co and U concentrations in the water are quite low. Al concentrations are stable around 30 µg/l. Cr concentrations vary from 0.2 to 73 µg/l, and displays the same pattern as Fe. Co and U have maximum concentrations of 54 and 39 µg/l respectively, but display no discernable trend.

Cd and Cu concentrations are low, between 2 and 7 µg/l. The lowest concentrations are found for V and Pb at around 0 - 0.5 µg/l. Th and Hg were below detection limit (< 0.004 and < 0.006 µg/l) in all samples.

Figure 30: Plot of Ni and Zn concentrations in the Galgeberg shale water samples. Sr has not been included due to the high concentration relative to Ni and Zn.
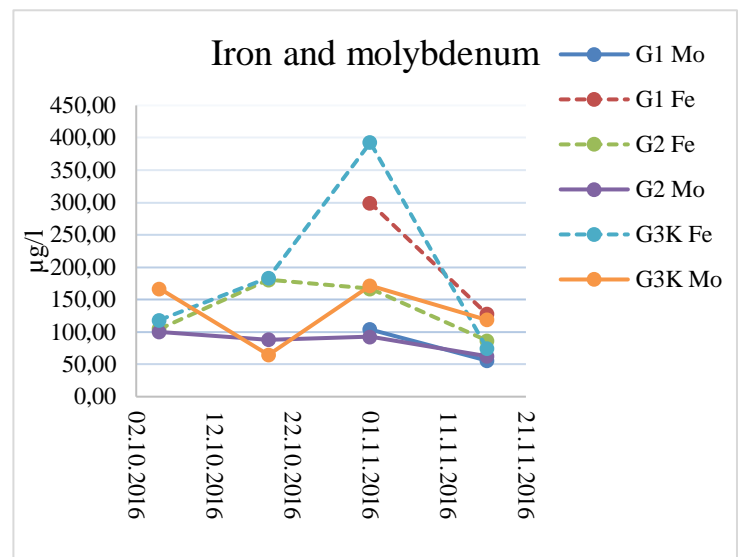
Figure 31: Plot of Fe and Mo concentrations in the Galgeberg shale water samples.

Ca and Mg are the dominant cations with concentrations between approx. 200 and 1000 mg/l (Table 15), displaying the same behavior as Zn, Ni and Sr with the highest concentrations in the first and third sampling. SO_4 is the anion with the highest concentration, reaching up to 5854 mg/l. The field measured pH level is slightly basic, fluctuating between 7.2 and 7.9.

Table 14: Results from the QICP-MS analysis of water samples from the Galgeberg shale containers. All units in µg/l. ICP-MS detection limit in parenthesis (µg/l).

		Al (0.303)	V (0.005)	Cr (0.066)	Fe (1.990)	Co (0.012)	Ni (2.860)	Cu (0.015)	Zn (0.230)	Sr (0.130)	Mo (0.050)	Cd (0.002)	Pb (0.002)	U (0.020)
G1														
	01.11.2016	30.6	0.2	68.8	299.6	54.3	1227.1	6.3	1239.2	9626.8	103.9	7.0	0.4	35.0
	16.11.2016	30.0	0.1	18.9	127.7	42.1	853.9	3.6	790.9	6089.8	55.7	4.4	0.1	18.9
G2														
	05.10.2016	31.9	0.1	4.8	104.7	34.0	946.9	2.7	795.7	9886.0	100.0	5.3	1.3	15.2
	19.10.2016	26.2	0.2	41.6	180.7	28.7	798.3	5.9	681.4	7323.8	88.2	4.4	0.1	16.2
	01.11.2016	30.6	0.1	18.1	166.8	27.5	1027.3	4.1	839.2	9452.2	92.7	4.4	0.2	21.1
	16.11.2016	31.4	0.0	0.2	86.7	23.7	746.3	3.5	542.1	5990.0	62.6	3.0	0.5	15.7
G3K														
	05.10.2016	25.4	0.2	6.7	118.1	34.0	679.9	2.4	644.1	9216.8	166.5	6.3	0.1	37.2
	19.10.2016	25.9	0.3	67.2	183.6	13.3	322.0	6.1	267.2	3409.7	64.6	3.1	0.1	18.3
	01.11.2016	32.7	0.3	73.9	392.6	27.9	727.2	7.2	493.9	8615.8	171.5	3.0	0.3	39.4
	16.11.2016	30.5	0.0	0.2	74.5	19.2	421.5	3.3	336.0	4792.4	118.7	2.1	0.4	27.0

Table 15: Results from the anion/kation analysis of water samples from the Galgeberg shale containers, and the pH measured in field. All units except pH is in mg/l.

		Na	K	Mg	Ca	F	Cl	SO4	pH
G1	01.11.2016	20.3	51.3	1016.9	418.5	0.2	3.2	4753.6	7.6
	16.11.2016	10.7	27.5	515.8	339.1	0.5	2.5	2848.6	7.62
G2	05.10.2016	16.0	65.3	659.9	462.5	0.1	7.8	3641.8	7.24
	19.10.2016	13.9	53.5	571.4	320.0	1.3	3.8	5854.1	7.84
	01.11.2016	20.4	52.4	902.7	422.2	0.1	3.2	4370.9	7.46
	16.11.2016	15.4	39.0	618.8	346.5	0.5	2.5	3244.0	7.51
G3K	05.10.2016	15.1	54.6	568.4	512.2	0.2	10.0	3312.1	7.35
	19.10.2016	5.5	17.5	187.8	201.1	1.2	3.3	2624.6	7.89
	01.11.2016	19.8	41.3	807.5	451.3	0.1	3.7	4048.0	7.67
	16.11.2016	14.6	27.8	532.2	335.4	0.5	2.7	2891.1	7.51

Statistical analysis

Table 16 shows the correlation matrix for the water analyses from the Galgeberg shale experiments.

V, Cr and Fe show a strong positive correlation with each other ($p \leq 0.01$). Cu correlates positively with these three elements, strong with Cr and Fe ($p \leq 0.01$) and moderate ($p \leq 0.05$) with V. All these elements also show a moderate to strong positive correlation with pH.

Ni has a strong positive correlation with Zn ($p \leq 0.01$) and Sr ($p \leq 0.05$) as well as a moderate correlation with Co ($p \leq 0.05$) and Cd ($p > 0.05$). Co also displays a strong positive correlation with Zn, and Cd, and a moderately positive correlation with Sr.

Ni, Zn and Sr all have a moderate positive correlation with sulfate, but only Zn has a p-value less than 0.05.

Mo shows a strong positive correlation with U ($p \leq 0.05$).

The elements that show a correlation with each other can be divided in two groups:

    1: V, Fe, Cr and Cu.

    2: Ni, Zn, Sr, Co, Cd and SO_4.

The cations are not distributed between the groups, but the elements in group 2 seem to correlate more with the cations Na and Mg and to some degree also Ca and K.

Table 16: Spearman correlation matrix for water sample analyses from containers G1, G2 and G3K.

	Al	V	Cr	Fe	Co	Ni	Cu	Zn	Sr	Mo	Cd	Pb	U	Na	K	Mg	Ca	F	Cl	SO4	pH
Al	1																				
V	-0.22	1																			
Cr	-0.02	0.91*	1																		
Fe	0.03	0.89*	0.98*	1																	
Co	0.01	0.19	0.26	0.21	1																
Ni	0.41	0.19	0.13	0.18	0.67**	1															
Cu	0.2	0.67**	0.88*	0.89*	0.13	0.76**	1														
Zn	0.21	-0.12	0.09	0.13	0.19	0.69**	-0.01	1													
Sr	0.38	0.08	0.13	0.19	0.1	0.56	-0.07	0.39	1												
Mo	0.19	0.35	0.15	0.16	0.16	-0.15	0.01	-0.08	0.08	1											
Cd	-0.26	0.31	0.28	0.26	0.86*	0.56	-0.09	0.72**	0.71**	0.08	1										
Pb	0.81*	-0.5	0.13	0.18	0.05	0.43	-0.04	-0.08	0.33	0.12	0.15	1									
U	-0.08	0.56	0.09	0.43	0.16	0.25	0.15	0.27	0.12	0.72**	0.08	0.2	1								
Na	0.68**	-0.04	0.07	0.07	0.18	0.25	0.15	0.58	0.82*	0.77*	0.47	0.18	0.2	1							
K	0.15	-0.08	-0.13	-0.07	0.18	0.46	-0.35	0.55	0.75**	0.42	0.18	0.2	0.05	0.95*	1						
Mg	0.67	0.04	0.22	0.32	0.35	0.31	0.38	0.65**	0.55	0.38	0.58	0.3	0.26	0.5	0.54	1					
Ca	0.39	0.03	0.08	0.08	0.32	0.33	0.41	0.41	0.45	0.43	0.18	0.2	0.33	0.54	0.68**	0.55	1				
F	0.65**	-0.12	-0.09	-0.16	-0.26	-0.37	-0.01	-0.36	-0.41	-0.53	-0.68**	-0.29	-0.33	-0.82*	-0.44	-0.68**	-0.88*	1			
Cl	-0.19	0.43	0.21	0.24	0.19	-0.1	-0.14	0.04	0.04	0.52	0.44	0.28	0.12	0.05	0.71**	0.08	0.45	0.25	1		
SO4	0.28	0.16	0.33	0.41	0.41	0.62	0.32	0.15	0.61	0.35	0.37	0.26	0.14	0.64**	0.7**	0.79**	0.31	0.31	0.36	1	
pH	-0.26	0.57	0.68**	0.63**	-0.23	-0.3	0.77*	-0.41	-0.57	-0.29	0.26	0.37	0.06	-0.5	-0.61	-0.33	-0.74**	0.54	0.18	0.09	1

* $p\text{-value} < 0.01$

** $p\text{-value} < 0.05$

4.4 Column experiment

Table 17 and Table 18 show the water analysis results from the column experiment. The results from the control experiment have been subtracted to account for trace elements originating from the sand used to increase permeability. Values marked in red are negative or below detection limit. Nickel is only above detection limit in the first and last sampling. The values for Cu, Cd and Pb are so close to the values from the control experiment that origin of these elements is uncertain. Ni is below detection limit in all columns except for the first and last sampling in all columns.

Cr and Co concentrations are close to the levels in the control samples, but remain steady between 0.15 - 0.2 µg/l and 0.01 – 0.2 µg/l respectively. The same is true for Fe, which is varying between approximately 0.5 – 3 µg/l, before increasing to 31 µg/l in the last sampling.

Zn concentrations in the control samples are generally higher than the experiment samples, especially in the first three to four samplings. This is evident by the negative values in Table 17 and Table 18. The concentrations increase in all columns after the first three to four samplings. (Figure 32).

The trace elements with the highest concentrations are Al, Sr, Mo and U. Al and V have a general decreasing trend in all samples, and the samples from 16/1 with the longest residence times have the lowest concentrations (Figure 33).
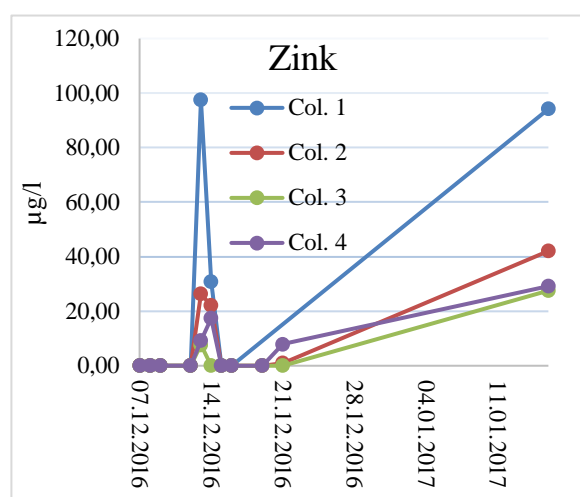
Figure 32: Plot of Zn concentration vs. sampling date for the column leaching experiment. Negative values have been replaced with "0" (ref. tables 17 and 18).

The behavior of Mo, Sr and U share some similarities (Figure 34). The concentrations of all these elements are high in the first sampling, then decrease before making a slight increase in the samples taken 16/12 and finally increasing even more on the last sampling.

Hg was below detection limit in all samples, and Th data could not be used due to contamination carried over from the 68A standard used.
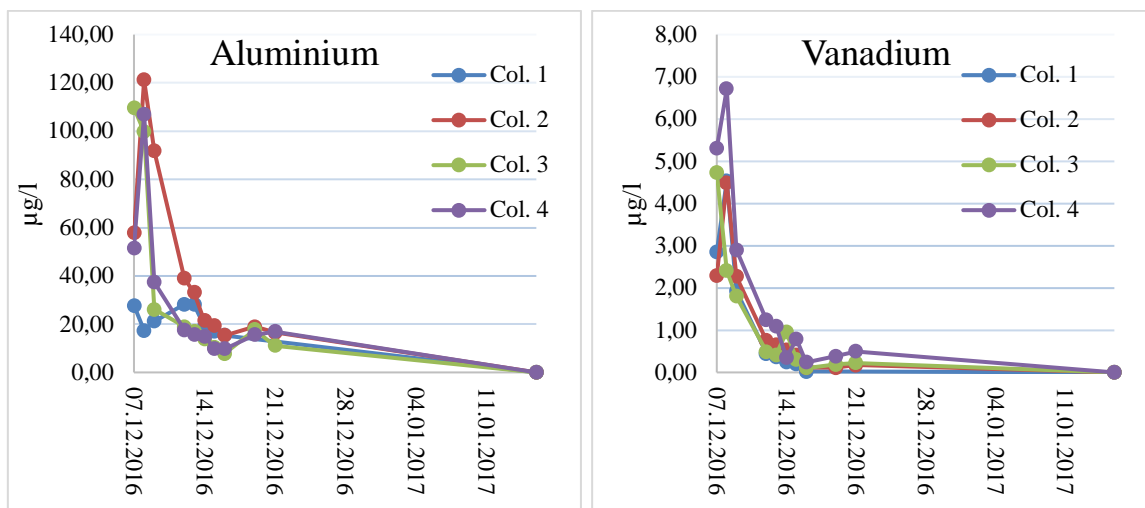
Figure 33: Plot of Aluminium and Vanadium concentrations from the column experiment vs. sampling date. Both elements show a decreasing concentration, with the lowest concetntrations in the sample with the longest residence time. Note: Negative values have been replaced with "0" (ref. tables 17 and 18).
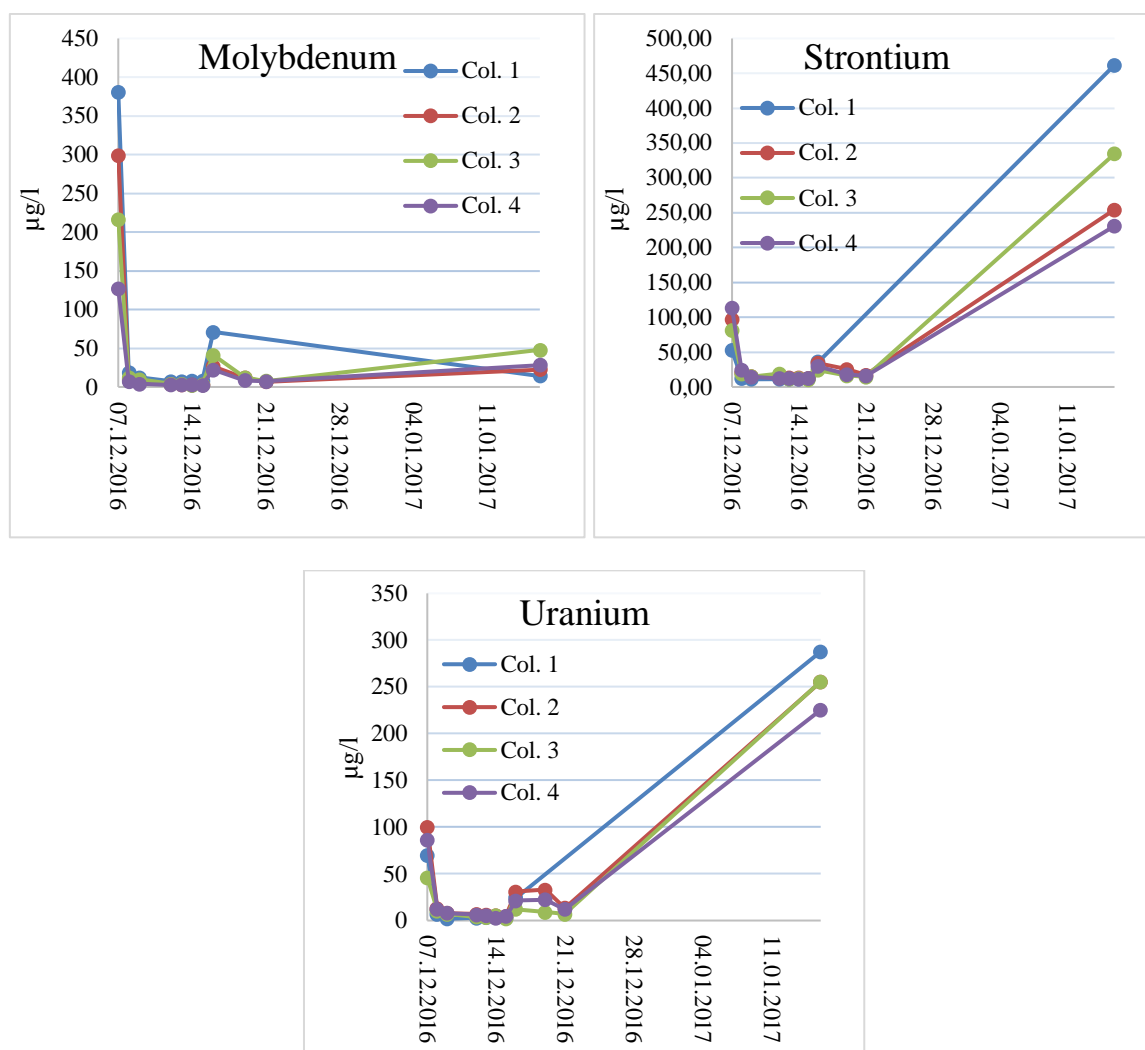
Figure 34: Plot of Molybdenum, strontium and uranium concentrations from the column experiments vs. sampling date. All the three elements show increasing concentrations, and the highest concentrations appear in the sample with the longest residence time.

64

Table 17: Results from the QICP-MS analysis of water samples from the column leaching experiment. All units in μg/l. Numbers marked in red are below detection limit or lower than the control sample concentration. Negative numbers occur due to subtraction of the control experiment concentration. ICP-MS detection limit in parenthesis (μg/l).

|	Al (0.180)	V (0.009)	Cr (0.024)	Fe (0.502)	Co (0.007)	Ni (4.630)	Cu (0.010)	Zn (0.045)	Sr (0.022)	Mo (0.145)	Cd (0.001)	Pb (0.001)	U (0.0140)
Col. 1													
07.des	27.74	2.85	-0.02	0.41	0.19	7.82	-0.46	-4.08	52.64	381.03	0.42	-0.04	70.06
08.des	17.39	4.54	0.19	0.99	0.01	0.83	-0.76	-10.25	12.54	19.00	0.02	0.02	6.56
09.des	21.23	1.93	0.19	0.73	0.00	0.72	-4.85	-39.16	11.45	12.04	-0.23	0.03	1.89
12.des	28.25	0.45	0.10	0.71	0.01	0.91	-0.71	-3.71	11.21	7.33	-0.07	-0.02	2.76
13.des	28.05	0.36	0.13	1.38	0.06	2.13	-0.34	97.51	11.32	7.30	-0.06	0.00	3.43
14.des	19.28	0.25	0.15	1.49	0.03	0.49	0.02	30.87	11.51	7.55	-0.08	0.06	3.21
15.des	17.02	0.20	0.12	1.27	0.01	1.02	-0.85	-1.81	12.31	8.14	-0.05	-0.01	2.93
16.des	15.42	0.02	0.04	2.99	0.05	1.69	-2.29	-4.28	36.11	70.80	-0.17	-0.02	24.50
16.jan	5.05	-0.03	0.11	30.56	3.18	70.63	2.43	100.85	494.07	14.39	-0.01	0.09	288.26
Col. 2													
07.des	57.79	2.28	0.01	1.65	0.13	14.66	-0.53	-11.79	97.30	298.90	0.14	-0.08	100.15
08.des	121.20	4.49	0.29	1.16	0.01	0.71	-0.77	-10.14	21.11	9.09	-0.42	0.00	12.64
09.des	91.73	2.27	0.26	1.94	-0.02	0.64	-4.71	-40.11	15.28	5.35	-0.31	-0.06	7.96
12.des	38.95	0.76	0.15	0.80	0.00	0.71	-1.34	-13.87	13.99	3.37	-0.04	-0.02	7.07
13.des	33.12	0.65	0.14	1.04	0.01	-1.31	-1.63	26.37	12.92	3.02	-0.09	-0.05	6.25
14.des	21.46	0.54	0.16	0.77	0.02	0.10	-0.62	22.08	12.89	2.65	-0.09	0.01	5.38
15.des	19.41	0.42	0.15	1.03	0.01	0.38	-0.90	-2.22	12.59	2.73	-0.06	-0.02	5.02
16.des	15.32	0.11	0.11	2.36	0.01	0.55	-3.87	-5.54	34.16	26.58	-0.24	0.02	30.81
19.des	18.97	0.12	0.15	1.95	0.03	0.43	-0.48	-1.48	25.66	11.71	-0.11	0.01	33.02
21.des	16.50	0.17	0.23	1.31	0.01	0.44	-0.42	0.97	17.30	6.71	-0.08	0.03	13.57
16.jan	-2.17	-0.20	-0.02	15.58	2.28	46.26	-14.70	42.06	254.43	22.65	-0.45	0.07	255.38

	Al (0.180)	V (0.009)	Cr (0.024)	Fe (0.502)	Co (0.007)	Ni (4.630)	Cu (0.010)	Zn (0.045)	Sr (0.022)	Mo (0.145)	Cd (0.001)	Pb (0.001)	U (0.0140)
Col. 3													
07.des	109.7	4.7	0.0	0.3	0.1	10.4	-0.8	-13.3	81.5	215.9	0.0	-0.1	46.0
08.des	99.8	2.4	0.1	0.9	0.0	-0.7	-0.7	-11.3	19.1	11.6	-0.4	0.0	10.5
09.des	26.1	1.8	0.2	3.4	0.1	0.6	-3.2	-38.1	15.0	9.9	-0.3	0.1	6.8
12.des	19.0	0.5	0.0	0.7	0.1	3.9	-1.4	-9.2	19.0	4.0	0.1	0.0	3.9
13.des	16.9	0.4	0.0	0.9	0.0	-1.3	-1.9	7.7	11.5	3.8	-0.1	-0.1	3.2
14.des	13.9	1.0	0.1	0.8	0.0	0.1	-0.9	-2.8	12.3	2.4	-0.1	0.0	5.3
15.des	10.5	0.3	0.1	0.9	0.0	0.1	-0.8	-2.1	10.9	3.2	-0.1	0.0	2.3
16.des	7.8	0.1	0.1	1.6	0.0	0.2	-3.9	-5.0	24.3	41.2	-0.2	0.0	12.3
19.des	17.7	0.2	0.1	1.0	0.0	0.3	-0.5	-1.4	16.2	12.2	-0.1	0.0	9.0
21.des	11.1	0.2	0.1	0.9	0.0	0.1	-0.2	-0.9	14.3	7.8	-0.1	0.0	6.9
16.jan	-4.5	-0.2	-0.1	18.4	4.5	49.2	-15.7	27.5	334.5	47.9	-0.4	0.0	255.7
Col. 4													
07.des	51.5	5.3	0.0	2.2	0.1	19.9	-0.4	-10.5	113.2	126.8	0.0	0.0	86.0
08.des	107.1	6.7	0.2	1.6	0.0	0.8	-0.7	-10.9	24.5	7.0	-0.4	0.0	12.6
09.des	37.3	2.9	0.1	0.8	0.0	0.8	-4.8	-40.0	14.3	4.0	-0.3	-0.1	8.1
12.des	17.6	1.2	0.1	0.8	0.0	0.2	-1.5	-14.7	12.3	2.8	-0.1	0.0	6.3
13.des	15.7	1.1	0.1	1.0	0.0	-1.0	-1.6	9.2	12.4	2.6	-0.1	0.0	5.5
14.des	14.9	0.4	0.1	0.8	0.0	0.6	-0.5	17.5	11.5	3.3	-0.1	0.0	2.7
15.des	9.9	0.8	0.1	1.1	0.0	0.0	-0.9	-2.4	12.0	2.4	-0.1	0.0	4.6
16.des	9.8	0.2	0.0	2.0	0.0	0.9	-3.6	-4.7	29.8	22.0	-0.2	0.0	21.2
19.des	15.6	0.4	0.2	1.5	0.0	0.0	-0.4	-1.0	18.3	8.5	-0.1	0.0	22.5
21.des	16.9	0.5	0.2	1.0	0.0	0.5	-15.8	7.9	15.6	7.3	-0.1	0.1	12.0
16.jan	-3.7	-0.2	-0.1	14.9	3.1	80.2	0.8	29.2	231.0	28.4	-0.4	0.0	225.3

Results from the anion/cation analysis of the water samples are given in appendix VI. Anions were not analyzed due to miscommunication on the authors behalf. In general, Ca is the dominant cation with concentrations between 5 and 25 mg/l. K, Mg and Na levels are generally lower (0 – 5 mg/l), and close to the values from the control experiment. All the cations have a higher concentration in the first sample as exemplified by Ca and K in Figure 35 and 36. The Ca concentrations increase from around 5 to 7 - 15 mg/l in the sample taken the 16/12, as was the case with some of the trace elements. Na, Mg and K concentrations are generally below 1 mg/l in all samples except the first and last. In the last sample, the concentration has increased for all the cations except Ca, which was not detected.
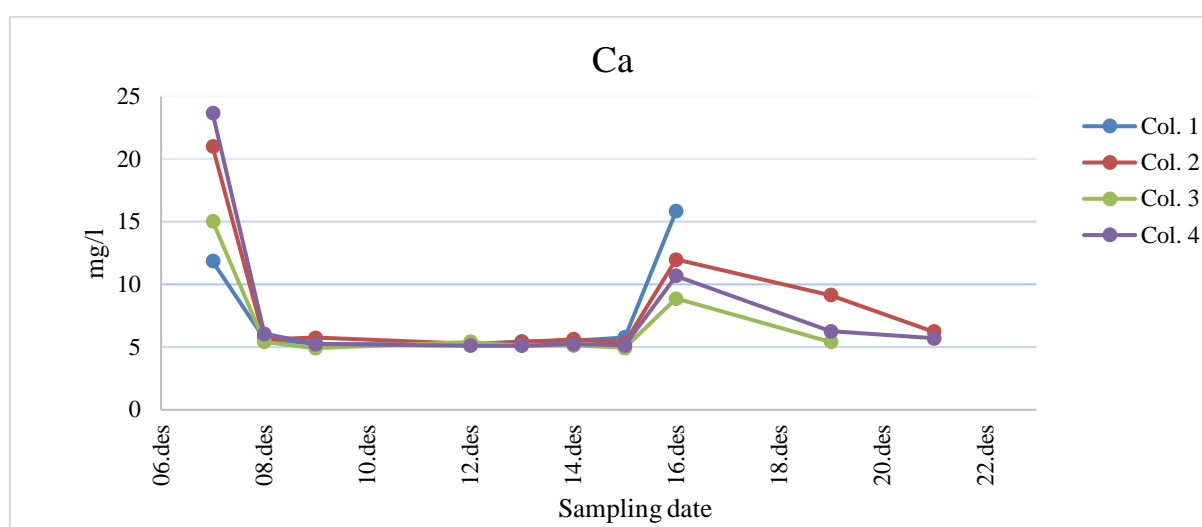
Figure 35: Plot of Ca concentrations from the column experiment. The concentrations decrease to almost zero after the first sampling before increasing in the 16/12 samples. No Ca was detected in the 16/1 samples.
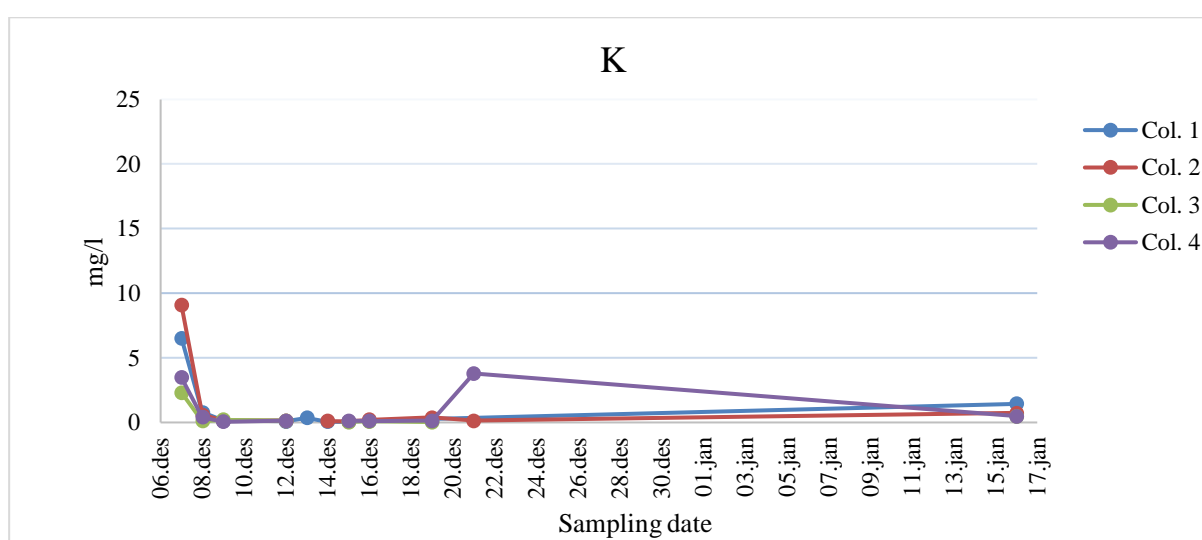
Figure 36: Plot of K concentrations from the column experiment. The concentrations decrease to almost zero after the first sampling and concentrations are mostly below 1 mg/l.

Statistical analysis

Table 19 gives the Spearman correlation matrices for the four columns in the experiment. Elements with concentrations below detection limit, or close to the values in the control experiment have not been included.

Al is positively correlated to V in all the experiments. In columns 2, 3 and 4 they correlate strongly with $p \leq 0.01$, and in column 1 the correlation is moderate with $p \leq 0.05$. Fe correlates negatively with Al and V in all columns, but only moderate in columns 1 and 3.

U has a strong positive correlation with Sr and Mo ($p \leq 0.01$) in all columns except column 1 where it has a moderate correlation with Mo. U correlates positively with Co in columns 1, 2 and 4 and Fe in columns 1 and 2. Sr has a strong positive correlation with Mo.

The trace element concentrations were also checked for correlation against the residence time of the water in each column for each sampling. This only yielded a strong negative correlation with V and strong positive correlation with Fe in column 1. All other correlations were below 0.5 and the results were therefore not included. Cations were also not included in the correlation due to the many gaps in the data (appendix V).

Table 19: Spearman correlation matrix for water anaylsis results from the column leaching experiment.

Col. 1

	Al	V	Cr	Fe	Co	Sr	Mo	U
Al	1							
V	0.62	1						
Cr	0	0.3	1					
Fe	-0.72**	-0.83*	0.06	1				
Co	-0.22	-0.41	-0.58	0.42	1			
Sr	-0.73**	-0.27	-0.38	0.33	0.59	1		
Mo	-0.48	0.13	-0.35	-0.07	0.25	0.83*	1	
U	-0.48	-0.25	-0.48	0.4	0.85*	0.85*	0.86*	1
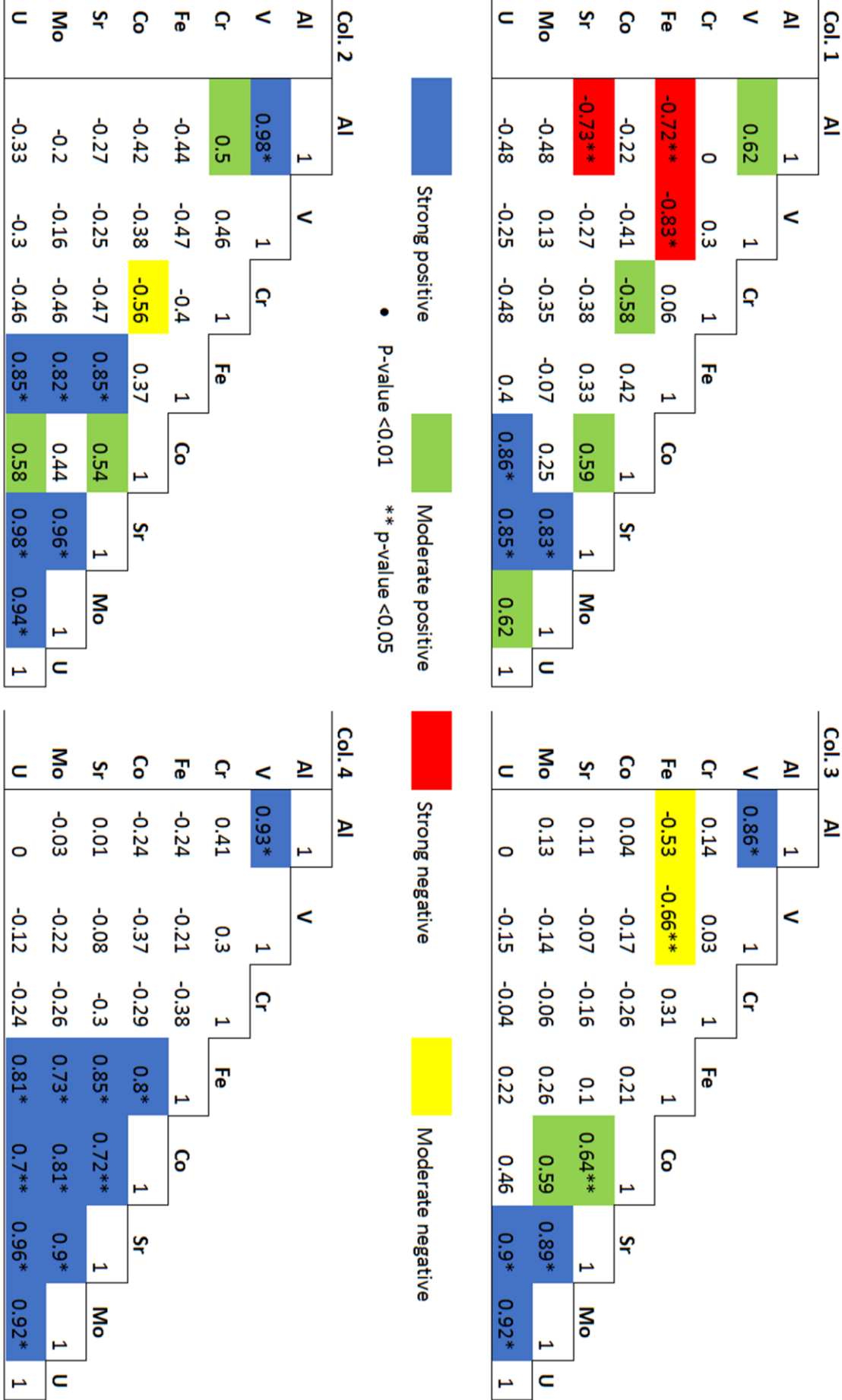
Col. 2

	Al	V	Cr	Fe	Co	Sr	Mo	U
Al	1							
V	0.98*	1						
Cr	0.5	0.46	1					
Fe	-0.44	-0.47	-0.4	1				
Co	-0.42	-0.38	-0.56	0.37	1			
Sr	-0.27	-0.25	-0.47	0.85*	0.54	1		
Mo	-0.2	-0.16	-0.46	0.82*	0.44	0.96*	1	
U	-0.33	-0.3	-0.46	0.85*	0.58	0.98*	0.94*	1

Col. 3

	Al	V	Cr	Fe	Co	Sr	Mo	U
Al	1							
V	0.86*	1						
Cr	0.14	0.03	1					
Fe	-0.53	-0.66**	0.31	1				
Co	0.04	-0.17	-0.26	0.21	1			
Sr	0.11	-0.07	-0.16	0.1	0.59	1		
Mo	0.13	-0.14	-0.06	0.26	0.64**	0.89*	1	
U	0	-0.15	-0.04	0.22	0.46	0.9*	0.92*	1

Col. 4

	Al	V	Cr	Fe	Co	Sr	Mo	U
Al	1							
V	0.93*	1						
Cr	0.41	0.3	1					
Fe	-0.24	-0.21	-0.38	1				
Co	-0.24	-0.37	-0.29	0.8*	1			
Sr	0.01	-0.08	-0.3	0.85*	0.72**	1		
Mo	-0.03	-0.22	-0.26	0.73*	0.81*	0.9*	1	
U	0	-0.12	-0.24	0.81*	0.7**	0.96*	0.92*	1

Legend

- Strong positive (blue)
- Moderate positive (green)
- Strong negative (red)
- Moderate negative (yellow)
- * $P\text{-value} < 0.01$
- ** $p\text{-value} < 0.05$

4.5 PHREEQC modelling

To simplify the modelling process, only a few phases were included in the model. Quartz, feldspar and the mica minerals are very stable minerals in atmospheric conditions and neutral pH. Weathering rates for these minerals are therefore very low, on the order of 80000 – 34000000 years for 1 mm crystals (Appelo and Postma, 2005) and are not included in the models. Calcite was added as an equilibrium phase, together with goethite, gypsum and oxygen. The purpose of the model was to simulate the long-term leaching potential of alum shale exposed to water and oxygen. Modelling all the mineral phases that are potential sources of trace elements is too complicated, so only two phases were included (full PHREEQC code in appendix VI).

Sphalerite was used as a main source of Zn. The leaching experiments show that Zn is easily mobilized. Apatite was used as a source of uranium, and a phase where 10 % of Ca was replaced with U was used. It is not known if apatite can be a major source of leachable U in alum shale, so the purpose was also to test if this is possible. To calibrate the model, the average Zn and U concentrations from containers AT1-AT4K were calculated for 2015 and 2016 from the values in Table 9 and appendix II and plotted against the model results. From this, the 1st-order rate constant k (eq. 3.5.1) was established by trial and error

To replicate the pH conditions, the pyrite oxidation rate was tweaked until a best fit with experimental data was obtained. Figure 37 shows the result of pyrite oxidation on pH with modelled data plotted together with experimental data (average pH) from AT1 - AT4K. The rate constant (eq. 2.2.3) had to be changed from $10^{-8.19}$ to $10^{-10.19}$ mol/m^2/s to give a reasonable fit to the experiment data. The left figure shows how pH develops when 0.99 moles of calcite is in equilibrium with water. The right figure shows the model without calcite and the buffering effect of calcite is clearly visible, as the pH drops to less than 2 in 100 days.
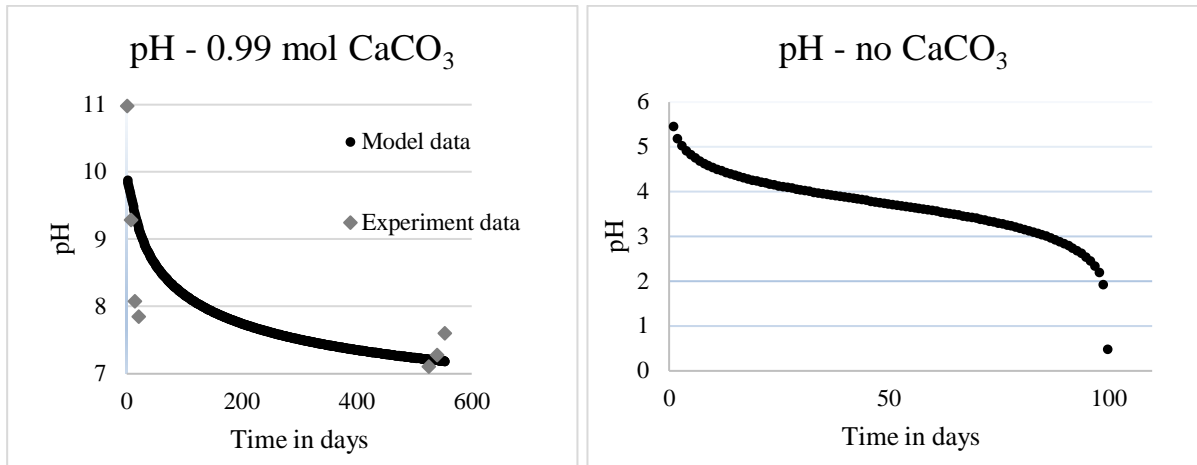
Figure 37: Model of pH in water in contact with alum shale with and without calcite. The pH decreases drastically without the buffering effect of calcite and the pH is 2 within 100 days.

Figure 38 shows the SO_4 and Ca concentrations in the water, plotted with average experiment data from AT1 - AT4K. The experiment data concentrations are four to five times higher for Ca and 50 to almost 400 times higher for SO_4.
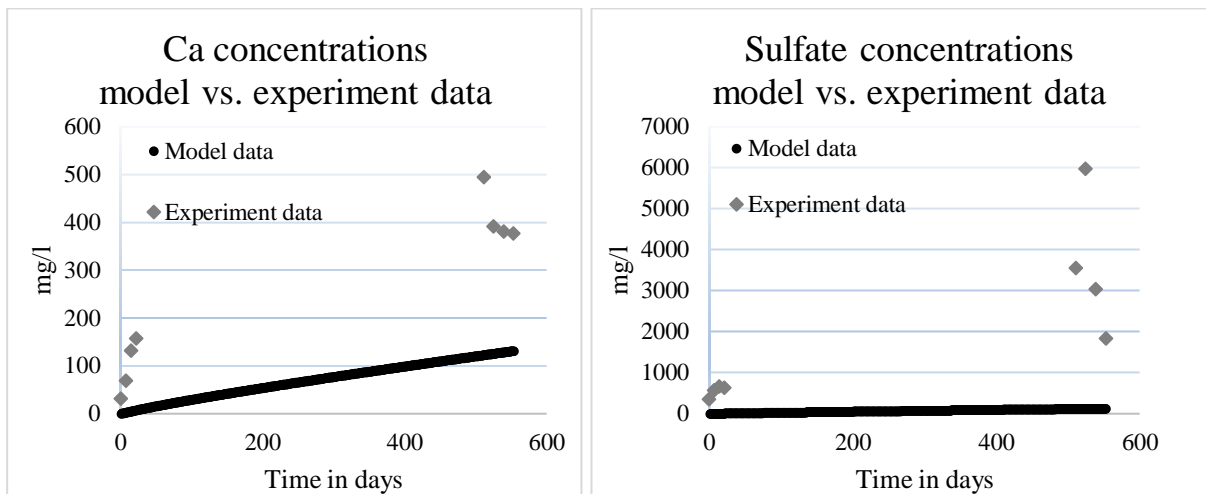
Figure 38: Plots of modeled Ca and SO_4 concentrations vs. average experimental data from containers AT1-AT4K. The modelled Ca concentrations are four to five times lower than the experiment values. For SO_4 the difference is even larger, with experiment concentrations 50 to 400 times higher than the model.

Figure 39 shows a model with fluorapatite as the U-bearing phase, using two different rate constants k. Even though the rate constant is 100000 times higher in the right figure, the rate remains the same.
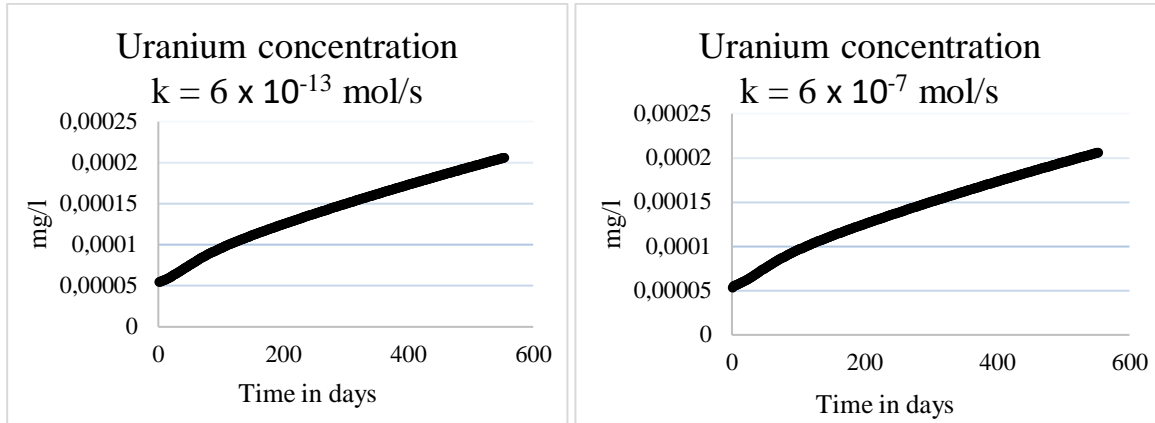
Figure 39: Plots of modeled uranium concentrations, using two different rate constants and fluorapatite as source. Increasing the rate constant from 6 x 10^{-13} to 6 x 10^{-7} mol/s had no effect on the dissolution rate.

This is an indication that the rate is affected by a limiting factor. The data shows the solution being saturated with fluorapatite, this in turn will affect the rate due to the $(1 - \Omega)$ factor in eq. 3.5.1, where Ω at saturation approaches 1. Figure 40 shows a model with hydroxylapatite instead of fluorapatite as the U-bearing phase with k=6 x 10^{-13} mol/s,
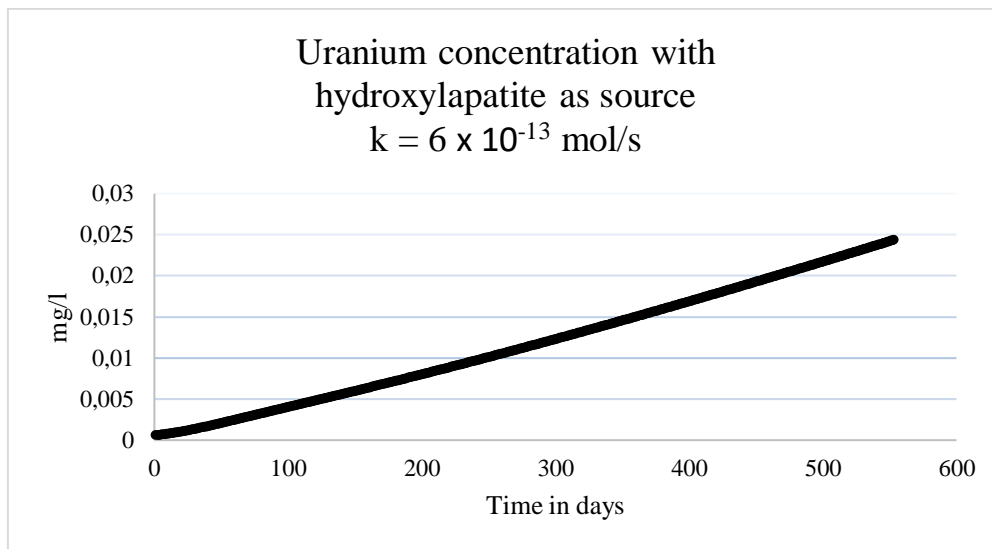
Figure 40: Plot of modeled uranium concentration with hydroxlapatite as U-source.

Using the same rate as in Figure 39, the concentrations are much higher, but still lower than the experimental data from AT1 - AT4K, which show average concentrations between 0.5 and 1 mg/l. Changing the rate to k=6 x 10^{-7} mol/s gave no effect, this is due to the rate being limited by hydroxylapatite saturation. The normalized rate will then be 1.7 x 10^{-18} mol/g/s, where g is grams of shale material (200 L shale, assuming 30 % porosity and average density 2500 g/dm^3).

72
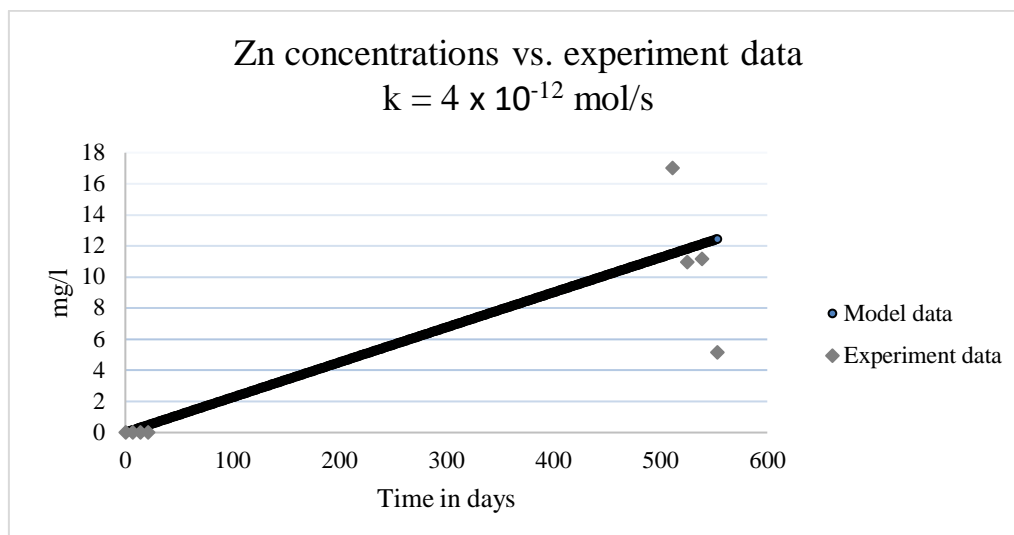
Figure 41: Plot of modeled Zn concentrations vs. average bulk experiment water concentrations from containers AT1-AT4K.

Figure 41 shows a plot of modeled Zn concentrations vs. experiment data using the rate established. A good fit to the data was obtained with $k = 4 \times 10^{-12}$ mol/s. This gives a normalized rate of 1.1×10^{-17} mol/g/s.

By applying the rate equations established, the model was used to simulate the potential leaching behavior of Zn and U over longer periods of time. Table 20 shows the modeling results for 10, 20 and 50 years, with 0.99 mol of calcite. It is evident that the SO_4 and Ca rates are too low when comparing to the leaching experiment.

Table 20: Zn, U, Ca, SO_4 concentrations and pH for selected timesteps over 50 years in a geochemical model with 0.99 mol calcite.

Time (years)	pH	U (mg/l)	Zn (mg/l)	Ca (mg/l)	Sulfate (mg/l)
1	7.65	0.02	8.23	64.30	91.69
5	6.84	0.09	40.63	216.78	375.81
10	6.55	0.20	80.00	361.45	696.77
20	6.30	0.40	155.11	609.54	1297.48
30	6.18	0.61	225.65	728.05	1599.78
40	6.11	0.84	291.92	739.68	1641.47
50	6.06	1.08	354.17	749.34	1680.67

Table 21 shows the modeling result without calcite. The pyrite oxidation model breaks down when pyrite saturation is reached which is evident by the very high and constant SO_4 concentration. The Zn mobilization is the same as with calcite, as there is no pH dependency defined in the rate equation. Ca levels are naturally much lower, as the only source of Ca is the apatite. U mobilization is also higher, likely due to Ca being the limiting factor in precipitating apatite out of solution.

Table 21: Zn, U, Ca, SO_4 concentrations and pH for selected timesteps over 50 years in a geochemical model without calcite.

Time (years)	pH	U (mg/l)	Zn (mg/l)	Ca (mg/l)	Sulfate (mg/l)
1	< 2	0.7	8.4	3.8	413327.0
5	< 2	3.5	41.6	18.8	413375.0
10	< 2	6.9	81.9	37.6	413432.6
20	< 2	13.8	158.9	75.1	413547.9
30	< 2	20.7	231.1	112.5	413653.6
40	< 2	27.5	298.9	149.7	413749.6
50	< 2	34.3	362.6	186.7	413836.1

5   Discussion

5.1   Mineralogical composition

The XRD results (Figure 9, 10, 11 and 12) indicate that the samples analyzed in this study does not differ greatly from alum shales in the studies mentioned in chapter 3. A few possible sources of error were observed during the XRD analysis process along with those already mentioned in chapter 3. Bjørlykke (1974) gives an average sulfur content of 2.6 % in alum shales, the analysis programs can therefore seem to have overestimated the amount of sulfides present in some of the alum shale samples (Figure 9). It was difficult to distinguish between the different feldspar endmembers in the diffractograms. Due to these uncertainties, the weight percentages of the minerals should only be considered as an indicator of relative abundances.

Major mineralogical constituents are similar in most of the samples, with quartz, mica, calcite, feldspar and pyrite being the most abundant. The Galgeberg shale composition (Figure 10) is quite similar to the alum shale samples (Figure 9), but the mica content is higher and the sulfide content is lower. The sulfides in the Galgeberg shale seem to be gathered in larger aggregates and crystals than in the alum shale (Figure 19a and b), where they are more finely distributed in the matrix (Figure 14). The samples from borehole 1 and 2 differed from the Gran samples in that the sulfides occur in veins together with calcite (Figure 23b and 26a and b). This could be due to contact metamorphism, as the borelogs (Figure 6) indicate intrusives at four and approximately nine meters. Another indicator of heat exposure is that seven out of eight analyzed sulfide crystals have a Fe:S ratio of 1:1 (Table 7), which indicate that they consist of pyrrhotite and not pyrite. Pyrrhotite can be formed from pyrite when it is exposed to heat (Antun, 1967, Vokes, 1993). Pyrrhotite was also detected by XRD in both these samples, and in two samples from borehole 2 (Figure 11 and 12).

The mappings done in SEM did for the most part reflect the results from the XRD. Sample BH1N - 1 m and BH2S – 9m were the only samples that differed greatly. XRD showed that BH1N – 1 m had a shale composition with about 10 % calcite (Figure 11), while the thin section contained mostly calcite (appendix IV-III). BH2S – 9 m seemed to contain mostly calcite (60 – 70 wt. %) in the XRD (Figure 12), but the thin section (appendix IV-III) showed almost no calcite. This shows that even though care is taken in collecting representative samples, the heterogeneity of the rock material can have a large impact on the observed results. The detection

limit of bulk XRD is around 5 %, which does not allow for detection of minor mineral constituents. SEM enables the identification of such phases which can be important sources of many of the trace elements found in the water samples from the leaching experiments. As an example, Abreham (2007) identified sphalerite and chalcopyrite (which are sources of Zn and Cu) in SEM, both of which were not detected with XRD.

Trace element content measured with handheld XRF by Fjermestad et al. (2017) show that the average trace element content in the alum shale from the tunnel is higher than in the alum shale from the roadcut. The only exceptions are U and Mo which are higher in the roadcut samples.

Uranium

Some U-bearing mineral phases were discovered with SEM, shown in Figure 25 and Table 6. The phases include U-bearing monazite, U-bearing phosphate/apatite, and possibly U-oxide and U-silicate. The analyzed monazite crystals are typically between 2 – 5 µm and contain between 0.2 and 0.4 atomic % of U and occasionally appear in the matrix. When comparing the total amounts of U in alum shale (Table 1) with the size and distribution of monazite crystals) in the examined samples (Figure 18 and appendix IV), it is unlikely that detrital minerals are the main source of U. U is a known trace element in phosphorite rock and in apatite (Altschulter et al., 1958). However, the amount of U normally found in apatite is less than 1 %, while the levels found in U-bearing phosphate/phosphate-associated phase are up to 18 atomic % (Table 6). Looking closer at the chemical composition of this mineral, the P level is very low compared to O and U, and could therefore come from the surrounding apatite crystal. This suggests this could instead be inclusions of UO_2 or UO_3 in the apatite crystal. Swanson (1961) postulated that organic carbon and phosphate are major U bearing phases in modern marine basins and black shales. Association between U and P in alum shales has earlier been demonstrated by Armands (1973), and a recent study by Lecomte et al. (2017) further supports this link between U and P. The 2017 study suggested that apatite phases containing as much as 1500 µg/cm^3 U could exist in immature alum shales. They also found that U exists as a U-Ti oxides or phospho-silicates clustered in biogenic phosphate nodules in more mature shales, this might explain spectrum 1 and 2 observed in Figure 25.

Zink and cadmium

Sphalerite was the only zinc bearing mineral discovered with SEM, in the analyzed samples it was found as minor inclusion (~5 µm) in pyrite crystals (Figure 17 and appendix IV). Earlier studies have suggested that Zn is bound in a sulfide phase separate from pyrite (Lavergren et al., 2009a, Fjermestad, 2013), but Zn only shows a positive correlation with SO_4 in the Galgeberg shale samples. Zn concentrations are highest in the water samples from AT1 - AT4K (Table 9), in which the rock samples all have sulfide contents above 20 % (Figure 9). The sulfide content in the Galgeberg shale rock samples are lower than the content in the rock samples from A1, A2 and A3K (Figure 9 and 10). However, the Zn concentration in water samples from the Galgeberg shale containers are higher than the concentration in the water samples from A1, A2 and A3K (Table 8 and 14). This might be a coincidence, and the XRD may not really represents the bulk mineralogy of all the rock volume in the container, or it is an indicator that Zn is also bound in a separate phase in the shale. All the sphalerite crystals found with SEM in alum shale contained Cd, and Zn correlates with Cd in the water samples from G1 - G3K and AT1 - AT4K (Table 13 and 16). Cd was not found in any other phases so this can indicate that sphalerite is a Cd source in alum shale. Cd is known to be associated with calcite either as replacement for Ca or sorbed to calcite surfaces (Papadopoulos and Rowell, 1988, Rimstidt et al., 1998), but no indication of this was found in any of the experiments.

Copper

Copper was identified in chalcopyrite using both SEM and XRD. The mineral was found in the Galgeberg shale and BH2S using SEM (Figure 22 and appendix IV-II and IV-VI), but was also detected in AT4K and BH1N – 3 m by XRD (Figure 9 and 11). SEM shows that the chalcopyrite mainly occurs as small inclusions in larger pyrite crystals, but one example of a larger chalcopyrite crystal was also found. Earlier studies such as Armands (1973), Lavergren et al. (2009a) and (Fjermestad, 2013) have linked the Cu in alum shale with a sulfide phase. Cu concentrations are low in the water samples from both the bulk experiment and the lab experiment (Table 8, 9, 14, 17 and 18). Cu does not show a significant correlation with any other elements except in samples AT1 - AT4K where it correlates with V, Co, Zn, Cd and Mg (Table 13). The correlation with Zn and Cd might further support the binding to sulfide, as both these elements were also detected in sphalerite (a sulfide phase).

Lead

Galena (PbS) was detected by SEM in samples from both boreholes (Figure 24a and appendix IV-VI), and a lead bearing U-P associated oxide or silicate was detected in BH1N - 7 m (Figure 25). These were the only Pb bearing mineral phases detected. Galena occurs both as small single crystals ~2 µm and as inclusions in larger pyrite crystals.

Arsenic and cobolt

Arsenic and cobalt were both found in the sulfide arsenopyrite, some of which contained enough Co to be classified as cobaltite (Figure 24b and appendix IV-VI). Co is not found in any significant concentrations in the lab experiment (Table 17 and 18), but occurs in relatively high concentrations in the water samples from AT1 - AT4K (Table 8, 9 and 14). Lavergren et al. (2009a) and Fjermestad (2013) suggested a binding to sulfides, and these finding support that theory.

Strontium

Strontium shows a strong positive correlation with Na, K, Mg and Ca in all samples from the bulk experiment (Table 12, 13 and 16). Sr was not identified in any minerals analyzed with SEM, but is one of the elements with the highest concentrations in the water samples (Table 8, 9 and 14). The ionic radii of Sr (1.18 Å), Ca (0.99 Å), Na (0.97 Å) and K (1.33 Å) are quite similar and Sr can substitute for Ca in calcite (Pingitore et al., 1992) and for K, Na and Ca in feldspar (Heier, 1962). Sr can also sorb to clay minerals and Fe-oxides/hydroxides (Trivedi and Axe, 1999). The water samples from AT1 and AT2 have the highest average Sr content, but only AT1 contains calcite according to XRD (Figure 9). Even though the XRD yields no calcite in some of the samples, the sampled material is only a small part of the volume used in the experiment and might not be representative for the actual mineralogy of all the shale material. The water samples from AT1 and AT2 do not have the highest average Ca concentrations, but they do have the highest average Mg and K concentrations (Table 11). The samples with the lowest average Sr concentration are from A1 (Table 8), which also have the lowest Ca, Mg and K concentrations (Table 10). It can therefore be considered likely that Sr in alum- and Galgeberg shale mainly occurs as substitutions in calcite or feldspar, and possibly sorbed to Al- and Fe-oxides.

Molybdenum and vanadium

No molybdenum, nickel or vanadium bearing mineral phases were identified in either SEM or XRD, so the mineralogy of these are uncertain. Both V and Mo is known to bind strongly to organic matter in modern anoxic ocean basins (Emerson and Huested, 1991) and previous studies such as Armands (1973) and Lavergren et al. (2009a) have indicated that this is also the case for these elements in alum shales. Ni and Mo concentrations in the water samples are relatively high (Table 8, 9 and 14), which suggests that these elements should be abundant in the shale.

Thorium

Thorium was only found in small amounts (< 2.5 atomic %) in monazite grains (Table 6). This is in support of the findings by Bjørlykke (1974) and Fjermestad (2013) described in chapter 2.

5.2 Trace element mobility for the case studies

Trace metal mobility has been assessed through both the bulk- and column leaching experiments. The analyzed water samples from the bulk experiment do not show any clear trends, the time period is too short and the number of samplings too low to not discard the variations as "natural" fluctuations due to external factors. The rock material in the different containers vary in grainsize and the permeability in each container is therefore different. Variations in permeability and precipitation lead to differing residence times for water in the containers. The conditions in the containers will normally be unsaturated except for periods with high precipitation. During periods with unsaturated conditions, some residual water will remain in the containers that will react with the rock material. This water will then be flushed during precipitation and a spike in the trace metal concentrations will occur. This can be observed to some degree in the water samples from the alum shale containers, by examining Figure 27, 28 and 29 you can see that some minerals have an increase in concentration when the precipitation is low, while others show an increase in concentration when precipitation is high. Variations in grainsize will also give differences in reactivity. Finer grain size means larger surface area, which will lead to higher reactivity for surface controlled mineral dissolution reactions.

pH

The pH of the water samples has been stable at neutral conditions (pH 6 – 8) for all the samplings in the bulk experiment (Table 10, 11 and 15). Even though the oxidation of sulfides is relatively high judging from the high sulfate concentrations, the pH has not yet reached acidic conditions. This is likely due to sufficient amounts of calcite being able to buffer the acid producing pyrite oxidation as demonstrated in the PHREEQC model (Figure 37). No pH data was collected for the column experiment, but the pH was measured in some samples during the experiment and it was stable between 6 – 7.

Observed errors

Some small errors were observed during the QICP-MS analysis. Aluminum was detected in acid blanks containing HNO_3, the acid was confirmed free of Al, so it is likely that it comes from the sample tubes themselves. The concentrations were between 0.42 and 2.6 µg/l which is low compared to the level in the samples, so the impact on the results is likely low. Some of the blanks containing only deionized water also contained some trace metals in relatively high concentrations (Fe, Al, Ni, Zn, Cr) and this is likely due to an error in the sampling process or some unclean equipment. Since all the equipment was washed between each sampling and the concentrations in the other blanks were low, the impact of this error is assumed to be low, but might have affected the first samples taken 5/10 and 19/10.

When examining the results from the bulk experiment alone it is hard to find a discernable pattern for trace element mobility. This is due to the many uncontrollable factors mentioned at the start of this chapter. However, when they are compared to the results from the NPRA and with the column experiment, it is possible to see how the leaching of trace elements evolves over time. It should be noted though, that the gap of almost 17 months between the last sampling by NPRA and the first sampling means there is no way to know the behavior of the trace metals in this period of time. Due to this time gap, the results from the NPRA were not included in the correlation analyses. A thorough report on the NPRA results was published a few days before the completion of this thesis (Fjermestad et al., 2017).

Uranium

The behavior of uranium is somewhat divided. In samples G1, AT1, AT2, AT3K and AT4K the U concentrations are low in the first samplings by the NPRA (appendix II), but show a

80

significant increase in the samples from 2016 (Table 9 and 14). In samples A1, A3, A2K, G2 and G3K the pattern is the opposite, with increasing concentrations in the first samplings (appendix II) and then drastically decreasing in the subsequent samples (Table 8 and 14). In the column experiment (Table 17 and 18) the concentrations decrease from the first sampling, but increase drastically in the last sampling (Figure 34), reaching levels comparable to the 2015 samplings from the tunnel shale containers (appendix II) which contain a considerably larger amount of rock. The highest U concentrations in the 2016 samples from the bulk experiment are 60 times higher than the WHO recommended drinking water limit (WHO, 2012).

Fjermestad (2013) found that most of U in alum- and black shale was bound in the residual fraction, but that small amounts were mobilized by oxidation of organic matter/sulfides and ionic exchange. The SEM results show that U exists in monazite, and is associated with apatite/phosphate either as substitutions or as U-oxide occurring together with apatite. Previous studies indicate that a large part of the U bound in marine sedimentary apatite is U^{4+} (Clarke and Altschuler, 1958), and the suggested mechanism for binding of U in anoxic sediments involves reduction of U^{6+} to U^{4+} (Klinkhammer and Palmer, 1991). Based on this, a large part of U existing in alum shale could be bound as U^{4+}. U^{4+} has a very low mobility due to the insolubility of its associated mineral phases (Elless and Lee, 1998), which means that it must be oxidized to the more mobile U^{6+} in order for mobilization to occur. U^{6+} reacts with oxygen to form uranyl (UO_2^{2+}), uranyl can form negatively charged carbonate complexes which increase U mobility under near neutral conditions (Echevarria et al., 2001).

The alum shale samples with the highest calcite content from XRD (A1, A2K, A3K and AT1) (Figure 9) also show the highest initial mobility (appendix II). Helmers (2013) observed that the highest mobility of U in neutral-alkaline conditions occurred in the black shale with the highest calcite content. This indicates that the easily mobilized fraction could be previously oxidized U bound as uranyl carbonate which is easily flushed into solution. It can also be due to oxidized U from other mineral phases or organics, which again reacts with carbonate formed from calcite dissolution.

The samples from AT1 - AT4K with the highest pH also have the lowest U concentrations, suggesting higher mobilization with lower pH (Table 9 and 11). The behavior of U in water is complex and highly dependent on pH and Eh, and at the pH conditions observed in this experiment it can be expected that the mobility of U is controlled by uranyl complexation with carbonate or phosphate (Langmuir, 1978).

The lack of direct identification of any major U bearing mineral phases in SEM compared to the relatively high U concentrations in the water samples suggests that U exists abundantly in a phase not directly observable with the methods employed in this study, such as organic carbon.

Trace elements with increasing concentration (Zn, Ni, Co, Cu, Cr, Cd, Sr)

Zn, Ni, Co, Cu, Cr and Cd all show a general low mobility in the column experiments, with levels either below detection or similar to the control sample (Table 17 and 18). Ni, Zn, Co and Cu concentrations are markedly higher in the last sampling, indicating a higher mobility with increased residence time. In the bulk experiments, Ni and Zn are among the elements with the highest concentrations (Table 8, 9 and 14), especially in the samples from AT1 - AT4K, where the highest concentrations (26684 and 34719 µg/l) of Ni and Zn are 398 and 578 times higher than what is considered Class V: "Very poor" according to threshold values for water quality assessment given by the Norwegian Environment Agency (appendix I) (Miljødirektoratet, 2016). Comparing the 2016 results with the 2015 and 2014 results (appendix II) it is apparent that both Ni and Zn are largely immobile when the shale is first exposed to water and oxygen, but the concentrations increase drastically with time and exposure. Cd, Cr and Co concentrations in the bulk experiments are lower than Ni and Zn, but the mobilization pattern is similar. The highest Cr, and Cd concentrations (284 and 737 µg/l) are 83 and 50 times higher than the limit for Class V (appendix I). All these elements tend to correlate with each other as shown in chapter 4.3. Cu follows much of the same pattern as the others, but the concentrations are much lower, still the highest concentration (132 µg/l) is 8 times the Class V limit (appendix I). The SEM results show that these elements are related to different sulfide phases and it is likely that the mobilization can be due to sulfide oxidation. The sulfate levels in the water samples follow the same trend as the trace elements, with very high concentrations (Table 10, 11 and 15) in the 2016 samples. The previous studies by Armands (1973), Bjørlykke (1974), Lavergren et al. (2009a) and (Fjermestad, 2013) have also indicated that sulfides are the major source of these elements in alum- and black shales.

After Zn, Sr is the element with the highest concentrations in the water samples from the leaching experiments (Table 8, 9 14, 17 and 18). As discussed earlier, Sr can substitute for Ca in calcite and for K in K-feldspar. Sr shows a strong correlation with Ca, Mg, Na and K in all the water samples from the bulk experiment (Table 12, 13 and 16) indicating that Sr is

mobilized due to calcite or dolomite dissolution. The correlation with K and Na could also indicate feldspar as a source, but considering the aforementioned slow rate of feldspar weathering it is not likely to be a large contributor. In the column experiments, Sr shows a strong correlation with both U and Mo (Table 19), and the concentration is highest in the first and last sampling (Figure 34). This suggests that Sr is mobilized through different processes, one fraction possibly sorbed to organic matter or Al/Fe-oxides and easily mobilized by flushing/ion exchange. The other fraction is bound in calcite and mobilized through calcite dissolution.

Trace elements with decreasing concentrations (V, Mo, Pb)

In the column experiment vanadium concentrations are higher in the first samplings and decrease in the subsequent samples (Figure 33). The same is true for the bulk experiments when comparing the samples from 2016 to the samples from 2014 and 2015 (Table 8, 9 and 14 and appendix II). V concentrations are of the same magnitude in both the bulk experiments and column experiments (Table 17 and 18). When considering the amount of material used (200 L of rock vs. a few grams), and the abundance of V in alum- and black shale it is obvious that V is largely immobile. V shows a strong positive correlation with Fe and Cr in the bulk experiments (Table 12, 13 and 16), but correlates negatively with Fe and positively with Al in the column experiment (Table 19). V sorbs strongest to goethite in the pH range 8 - 2 (Peacock and Sherman, 2004), and the same is true for Cr (Ajouyed et al., 2010) which might explain the correlation between these elements and Fe. This will hinder the mobilization of V, but also indicates that the small amount mobilized could be due to desorption from iron oxides together with Cr. The positive correlation with Al in the column experiment could mean that the initial spike in concentration is due to mobilization of V bound to clay minerals.

Mo displays much the same pattern as V in both the column experiment and the bulk experiments, with a spike in concentrations at the start of the experiment before decreasing (Table 8, 9, 14, 17, 18 and appendix II). The concentrations increased again with higher residence time (Figure 34). This indicates that Mo could be present in two fractions, one that is easily mobilized and one bound to more weathering resistant minerals as suggested by Lavergren et al. (2009a) and Fjermestad (2013). Mo was not found in any specific mineral phases in XRD or SEM. Correlation with other elements is inconsistent when comparing the different leaching experiments, except for Sr and U with whom Mo shows a moderate to strong

positive correlation (Table 12, 13 and 16). In the column experiment the correlation is strong with a p-value of less than 0.01 (Table 19). Earlier studies by Armands (1973), and McManus et al. (2006) have suggested that U and Mo are related to organic carbon in both modern marine sediments and in alum/black shale, which might explain the correlation.

It is therefore likely that the easily mobilized fraction of Mo is bound to organic matter or sulfides, as suggested by (Lavergren et al., 2009a). Under prolonged exposure, V and Mo both seem to be largely immobile in neutral and oxidizing conditions.

Lead seems to be largely immobile with concentrations mostly below 1 µg/l in both the bulk (Table 8, 9 and 14) and column experiment (Table 17 and 18), corresponding to Class I: "Background" (appendix I). Pb tends to sorb strongly to Fe-oxides/hydroxides (Hayes and Leckie, 1987), even if lead is released from e.g. oxidation of galena, under neutral pH conditions it will likely adsorb to goethite or other Fe-oxides/hydroxides produced by pyrite weathering. Earlier studies have found Pb to be bound in weathering resistant minerals and any significant mobilization would therefore likely require a lowering of pH.

Mobility of iron and aluminum

Although not considered trace elements, it is important to study the leaching of Fe and Al. As mentioned in chapter 2, Fe mobilization from alum- and black shales is mostly due to oxidation of sulfides and can serve as an indicator of pyrite oxidation rate. The bulk experiment results from the NPRA show a general decreasing trend in Fe concentrations in the first year (appendix II). The concentrations in the samples from this study are generally higher, but vary between 30 and 1000 µg/l (Table 8, 9 and 14). Results from the column experiment show low concentrations which increase drastically with residence time (Table 17 and 18). Fe^{2+} is the stable form of iron in aqueous solutions with pH 6 - 8, but in oxidizing conditions it will precipitate as iron hydroxide or oxidize to Fe^{3+} and precipitate as ferrihydrite, goethite or hematite (Hem, 1972, Beverskog and Puigdomenech, 1996) and thus decreasing Fe mobility.

Aluminum can be very toxic to aquatic organisms (Gensemer and Playle, 1999) and understanding its leachability from alum shale is important. Aluminum mobility trends are somewhat differing from container to container in the bulk experiment. In the samples from 2016 the concentrations are relatively stable around 30 µg/l (Table 8, 9 and 14). In the samples from the NPRA (appendix II) the behavior is varied, in the A1 - A3K samples the concentrations

increase, while in the G1 - G3K and AT1 - AT4K samples the concentrations decrease. The decrease in concentration is also seen in the column experiment, and the lowest concentrations occur in the sample with the longest residence time (16/1) (Figure 33). Al does not show any discernable correlation pattern with other elements in the leaching experiments (Table 12, 13 and 16). The only exception is V in the column experiments (Table 19), which has been discussed earlier. As mentioned in chapter 2, Al in alum shale is mostly bound in weathering resistant minerals such as feldspars and silicates, which upon weathering form relatively insoluble compounds such as kaolinite, montmorillonite and gibbsite (Appelo and Postma, 2005). These secondary minerals are very stable and their solubility is controlled by pH (Bache, 1986). Thus, Al will be immobile until a significant acidification of water has occurred.

5.3 Mobility simulations with PHREEQC

By combining a 1st-order kinetic reaction rate with the data from the bulk experiments it was possible to establish a simple model capable of simulating the leaching of Zn and U from alum shale. The model makes it possible to make a rough estimate of the future leaching potential of these elements from the rock material.

To assess the future development of the trace element mobility it is important to understand the change in pH. Water in contact with alum shale is known experience acidification, causing an increase in trace element mobility due to increased weathering and desorption of metal ions. The results from the two geochemical models presented in Figure 37 gives a rough estimate of the pH development in alum shale in contact with water and oxygen. The presence of calcite will give a significant buffering effect on the pH and even after 50 years the pH will be near neutral. Without calcite, the pH is below 2 after only 100 days. In reality the result will probably be somewhere in between, such as the pH levels measured by Lavergren et al. (2009b) in groundwater near black shale bedrock and burnt black shale deposits. Comparing the Ca and SO_4 concentrations from the model with the experimental data (Figure 38) it is evident that the modelled dissolution rate of both calcite and pyrite is too low. However, any attempts at adjusting the rate equations of either mineral will either give too much SO_4 or a pH that is too high. This could be an indicator of another mineral source of Ca or SO_4.

Modelling of U leaching has been challenging due to the difficulty of identifying specific phases to which U is bound. Based on the SEM results it was decided to define a U-bearing apatite

phase. As discussed earlier in this chapter, U seems to have a relation to phosphate in alum shale. The amount of U in the apatite phase was purposely set higher than the $0.5 - 1$ % proposed by Altschulter et al. (1958) to account for U associated with, but not bound in apatite. This can include among others, U-oxide such as shown in Figure 25. The model indicated that neither fluorapatite or hydroxylapatite can account for all the U released from weathering of alum shale due to saturation acting as a rate limiting process. This was however, not unexpected, as U is known to exist in other phases in the rock.

The dissolution rate constant found for U bearing apatite that gave the most U in solution was 1.7×10^{-18} mol/g/s (Figure 40). For sphalerite, a dissolution rate constant of 1.1×10^{-17} mol/g/s was found (Figure 41). In the literature, experimental dissolution rates are normalized over surface area, using pure mineral phases. This was not possible in the experiments performed for this thesis since crushed shale was used instead of a pure mineral phase. Instead the rate was normalized as mol/g/s, where g is grams of shale material. Since the rate constants established here were calibrated using the concentrations from the leaching experiments they should be considered rates for total Zn and U dissolution from alum shale, and not as rate constants for the dissolution of the mineral phases used in the modeling. The rate constants found can therefore not be directly compared to the rate constant and dissolution rates for apatite found by studies such as Palandri and Kharaka (2004) ($k=10^{-6}$ mol/m^2/s at 25°C and pH=0) and Chairat et al. (2004) ($R=1 \times 10^{-7}$ to $1.6 \times 10^{-11.8}$ mol/m^2/s), or the rate constants and dissolution rates found for sphalerite ($k=3.2 \times 10^{-3}$ mol/m^2/s) (Acero et al., 2007) ($R=5.75 \times 10^{-9}$ to 1.14×10^{-9} mol/m^2/s at 25 °C and pH=1) (Weisener et al., 2003). Such studies employ pure mineral phases that often have a very fine grain size in a controlled environment (typically 25 °C and a set pH), the dissolution rates and rate constants are therefore normally higher than the rate found in this study.

The long-term modelling of Zn and U mobilization (Table 20 and 21) yielded some interesting results even though the rates are simplified. The modelling of Zn shows that there is a potential of a long term high mobilization of this and other elements with a similar behavior and concentration in the alum shale. Modeling of U mobilization from U-bearing apatite did not yield any significant results when it comes to the long-term leaching potential of alum shale. It did however give indications that U-bearing apatite is not a significant source of mobilized U in alum shale because apatite dissolution is limited in aerobic and neutral conditions.

Even though the model has made it possible to make a rough estimate of the future leaching potential of U and Zn, the simplicity of the model has to be taken into account. Alum shale mineralogy is complex, and the fixation of the different elements in the rock is in no way well established. The simple model here only implements two elements, and only one mineral phase as the source of each element. Further on, the model is only a batch simulation and does not incorporate transport and sorption/desorption which is an important factor in the element mobilization. PHREEQC is only capable of doing equilibrium calculations in saturated conditions. In a real-life situation, the conditions in e.g. a shale deposit is likely unsaturated most of the time, and this requires solving Richards equation for transport in the vadose zone.

6 Conclusion

The alum shale material studied in this thesis displays a similar mineralogy as previously studied alum shales from the Oslo region. XRD gave a mineral composition with varying percentages of quartz, feldspars, micas, calcite, pyrite and pyrrhotite. The use of SEM enabled the identification of specific sulfide mineral phases that have previously been suggested as sources of the selected trace elements studied. Easily mobilized elements such as Ni, Zn, Cu, Co and Cd were identified in sphalerite, chalcopyrite, arsenopyrite and cobaltite. Uranium bearing minerals such as monazite was also identified together with U-bearing apatite/phosphate and U-oxide. XRD and SEM revealed that the samples from the boreholes in Jevnaker can contain as much as 20 wt. % pyrrhotite, indicating that alum shale material from this area can be more reactive than shale containing only pyrite.

The mobilization of different trace elements has been examined through the bulk and column leaching experiments. By comparing analyses from 2014, 2015 and 2016 it has been possible to examine the behavior of trace elements over a longer period of time. Ni, Zn, Cd, Co, Cu and Cr all follow a similar pattern, with concentrations increasing throughout the experiment. All these elements show relatively high mobilities. Ni and Zn were found in concentrations 398 and 578 times higher than what can be considered class V "Very poor" according to Norwegian standards (appendix I). Cu, Cd and Cr concentrations were 8, 50 and 83 times the class V limit. U was found in concentrations up to 60 times higher than the WHO drinking water standard and displays relatively high mobility in oxidizing and neutral to alkaline conditions.

In general, the concentrations of trace metals in the water samples are higher in the alum shale experiments compared to the Galgeberg shale experiments, uranium and cadmium in particular. The concentrations are however varying within the alum shale samples, with generally higher trace metal concentrations in the shale taken from the tunnel.

The use of geochemical modeling helped establish a simple dissolution rate for sphalerite, thought to be a major source of Zn in alum shale. A 1st-order rate equation gave a good fit with experimental data using a rate constant of 1.1×10^{-17} mol/g/s. Long term modeling (50 years) showed that Zn will continue to leach from alum shale under neutral conditions. The model allowed for testing of U-bearing apatite as a major source of U in alum shale. This was proved to have a limited effect as it will be naturally hindered by apatite saturation in the solution.

Pyrite oxidation modeling was also used to test the development in pH of the water in contact with alum shale. A good fit to experimental results was found by changing the rate constant of Williamson and Rimstidt (1994) from $10^{-8.19}$ to $10^{-10.19}$ mol/m^2/s. With calcite present, the pH was still neutral after 50 years, without calcite it dropped below two in 100 days. Understanding the processes affecting pH is crucial to understanding the mobilization of heavy metals from the shale.

Depositing alum- and black shale material exposed to meteoric water and oxygen will lead to heavy metal concentrations that can have a negative environmental impact. This study has shown that even at circum-neutral conditions, potentially harmful and environmentally damaging concentrations of heavy metals are mobilized from the alum shale material and can continue to do so for a long time. By combining tools such as a handheld XRF with rate equations based on controlled leaching experiments in a modelling tool like PHREEQC, there is a potential to develop a fast and cheap method to make good assessment of the future long term impact of alum- and black shale depots.

Suggestions for further research on the topic

Much of the current research has focused on sequential chemical extraction or analysis of groundwater in areas with alum shale. Natural leaching experiments involving alum shale like the ones attempted in this thesis are few. Through the work on this thesis a few lessons have been learned about the methods employed that should be considered in any future research. First and foremost, the physical setup of the column leaching experiment should be redesigned to prevent leaks and clogging. The crushed shale material should be sieved in order to have control of the grain size and the grain size itself should be evaluated when considering reactivity. The duration of the experiment should also be increased to a period of 3 - 6 months with more frequent samplings in the beginning, and then increasing the sampling interval to maybe once a week. This should give a better picture of the weathering process and will make it possible to establish empirical rate equations for the mobilization of the different trace elements. XRF and sequential chemical extraction should also be employed, to get a better understanding of the parent rock material.

Controlled leaching experiments in a reducing atmosphere would be valuable in the process of developing a modelling tool to assess the future impact of alum shale deposits. As for the geochemical modelling, the next step would be to include 1D transport and sorption processes

90

in a larger system by implementing the equations from chapter 2.2.4. It will be a step further towards a future 2D or 3D reactive transport model capable of modelling larger systems. To properly understand the shale/water interactions, a vadose zone transport model must be included.

Literature

Stortingsmelding nr. 024 (2003-2004) Nasjonal transportplan 2006-2015.

ABREHAM, Y. 2007. *Reactivity of alum and black shale in the Oslo region, Norway.* Master thesis, University of Oslo.

ACERO, P., CAMA, J. & AYORA, C. 2007. Sphalerite dissolution kinetics in acidic environment. *Applied Geochemistry,* 22**,** 1872-1883.

AJOUYED, O., HUREL, C., AMMARI, M., ALLAL, L. B. & MARMIER, N. 2010. Sorption of Cr(VI) onto natural iron and aluminum (oxy)hydroxides: Effects of pH, ionic strength and initial concentration. *Journal of Hazardous Materials,* 174**,** 616-622.

ALLARD, B., ARSENIE, I., HAKANSSON, K., KARLSSON, S., AHLBERG, A., LUNDGREN, T., COLLIN, M., RASMUSON, A. & STRANDELL, E. 1991. Effects of weathering on metal releases from an engineered deposit for alum shale leaching residues. *Water Air Soil Pollut.,* 57-8**,** 431-440.

ALTSCHULTER, Z. S., CLARKE JR, R. S. & YOUNG, E. J. 1958. Geochemistry of uranium in apatite and phosphorite. *Geological Survey Professional Paper 314-D.* - ed.: USGS.

ANTUN, P. 1967. Sedimentary pyrite and its metamorphism in the Oslo region. *Norsk Geologisk Tidsskrift,* 47**,** 211-235.

APPELO, C. A. J. & POSTMA, D. 2005. *Geochemistry, groundwater and pollution,* Leiden, A.A. Balkema Publishers.

ARMANDS, G. 1973. Geochemical studies of uranium, molybdenum and vanadium in a Swedish alum shale. *Acta Universitatis Stockholmiensis: Stockholm contributions in geology.* Stockholm: Almqvist & Wiksell.

BACHE, B. W. 1986. Aluminium mobilization in soils and waters. *Journal of the Geological Society,* 143**,** 699-706.

BELZILE, N., CHEN, Y.-W., CAI, M.-F. & LI, Y. 2004. A review on pyrrhotite oxidation. *Journal of Geochemical Exploration,* 84**,** 65-76.

BERNER, R. A. 1985. Sulphate reduction, organic matter decomposition and pyrite formation. *Phil. Trans. R. Soc. Lond. ,* Series A**,** 25-38.

BEVERSKOG, B. & PUIGDOMENECH, I. 1996. Revised pourbaix diagrams for iron at 25–300 °C. *Corrosion Science,* 38**,** 2121-2135.

BJØRLYKKE, K. 1974. Depositional History and Geochemical Composition of Lower Palaeozoic Epicontinental Sediments from the Oslo Region. *In:* ÅM, K. (ed.) *Bulletin 24: Norges Geologiske Undersøkelse Nr. 305.* Oslo: Universitetsforlaget.

BOGGS, S. 2011. *Principles of sedimentology and stratigraphy,* Boston, Prentice Hall.

BRAUT, G. S. 2015. *p-verdier* [Online]. Available: https://snl.no/p-verdier [Accessed 30.04.2017.

BRITANNICA, E. 2017. Trace element. *Encyclopædia Britannica.*

BÄCKSTRÖM, M. & SARTZ, L. 2015. Uranium leaching from a burning black shale deposit – present conditions and future scenarios. *In:* MERKEL, J. B. & ARAB, A. (eds.) *Uranium - Past and Future Challenges: Proceedings of the 7th International Conference on Uranium Mining and Hydrogeology.* Cham: Springer International Publishing.

CHAIRAT, C., OELKERS, E., SCHOTT, J. & LARTIGUE, J. 2004. The solubility and dissolution rates of natural apatite. *Geochim. Cosmochim. Acta,* 68**,** A145-A145.

CLARKE, R. S. & ALTSCHULER, Z. S. 1958. Determination of the oxidation state of uranium in apatite and phosphorite deposits. *Geochimica et Cosmochimica Acta,* 13**,** 127-142.

DINNEBIER, R. E., BILLINGE, S. J. L. & BAIL, A. L. 2008. *Powder Diffraction : Theory and Practice,* Cambridge, Royal Society of Chemistry.

ECHEVARRIA, G., SHEPPARD, M. I. & MOREL, J. 2001. Effect of pH on the sorption of uranium in soils. *Journal of Environmental Radioactivity,* 53**,** 257-264.

ELLESS, M. P. & LEE, S. Y. 1998. Uranium Solubility of Carbonate-Rich Uranium-Contaminated Soils. *Water, Air, and Soil Pollution,* 107**,** 147-162.

EMERSON, S. R. & HUESTED, S. S. 1991. Ocean anoxia and the concentrations of molybdenum and vanadium in seawater. *Marine Chemistry,* 34**,** 177-196.

ERLSTRÖM, M. 2014. Skiffergas och biogen gas i alunskiffern i Sverige, förekomst och geologiska förutsättningar - en översikt. Uppsala: Sveriges Geologiska Undersökning.

FALK, H., LAVERGREN, U. & BERGBÄCK, B. 2006. Metal mobility in alum shale from Öland, Sweden. *Journal of Geochemical Exploration,* 90**,** 157-165.

FJERMESTAD, H. 2013. *Mobilitet av Uran og andre metall i bergarter i ny vegtrasé på Gran, Hadeland.* Master Thesis, Universitetet for Miljø- og Biovitenskap.

FJERMESTAD, H., HAGELIA, P. & THOMASSEN, T. 2017. Utlekkingsforsøk med svartskifer fra Rv. 4, Hadeland. Statens Vegvesen.

GAUTNEB, H. & SÆTHER, O. M. 2009. A compilation of previously published geochemical data on the lower Cambro-Silurian sedimentary sequence, including the alum shales in the Oslo region. Trondheim: Norges Geologiske Undersøkelse.

GENSEMER, R. W. & PLAYLE, R. C. 1999. The Bioavailability and Toxicity of Aluminum in Aquatic Environments. *Critical Reviews in Environmental Science and Technology,* 29**,** 315-450.

GOLDBERG, S., CRISCENTI, L. J., TURNER, D. R., DAVIS, J. A. & CANTRELL, K. J. 2007. Adsorption–Desorption Processes in Subsurface Reactive Transport Modeling. *Vadose Zone Journal,* 6**,** 407-435.

GRAHAM, U. & IAN, C. 2008. Spearman's rho. *A Dictionary of Statistics.* Oxford University Press.

HAUKE, J. & KOSSOWSKI, T. 2011. Comparison of values of pearson's and spearman's correlation coefficients. *Quaestiones Geographicae,* 30**,** 87-93.

HAYES, K. F. & LECKIE, J. O. 1987. Mechanism of Lead Ion Adsorption at the Goethite—Water Interface. *In:* HAYES, K. F. & LECKIE, J. O. (eds.) *Geochemical Processes at Mineral Surfaces.* American Chemical Society.

HEIDEL, C. & TICHOMIROWA, M. 2011. The isotopic composition of sulfate from anaerobic and low oxygen pyrite oxidation experiments with ferric iron — New insights into oxidation mechanisms. *Chemical Geology,* 281**,** 305-316.

HEIER, K. 1962. Trace elements in feldspars—a review. *Norsk Geologisk Tidsskrift,* 42**,** 415-466.

HELMERS, T. A. 2013. *The mobility of uranium from U-containing bedrock materials as a function of ph: implications for tunnel construction.* Master Thesis, Norwegian University of Life Sciences.

HEM, J. D. 1972. Chemical Factors That Influence the Availability of Iron and Manganese in Aqueous Systems. *Geological Society of America Special Papers,* 140**,** 17-24.

HILLIER, S. 2000. Accurate quantitative analysis of clay and other minerals in sandstones by XRD: comparison of a Rietveld and a reference intensity ratio (RIR) method and the importance of sample preparation. *Clay Minerals,* 35**,** 291-291.

KARLSSON, L., BÄCKSTRÖM, M. & KARLSSON, S. 2011. *Natural weathering of shale products from Kvarntorp.* Bachelor thesis, University of Örebro.

KLINKHAMMER, G. P. & PALMER, M. R. 1991. Uranium in the oceans: Where it goes and why. *Geochimica et Cosmochimica Acta,* 55**,** 1799-1806.

LANGMUIR, D. 1978. Uranium solution-mineral equilibria at low temperatures with applications to sedimentary ore deposits. *Geochimica et Cosmochimica Acta,* 42**,** 547-569.

LARSEN, B. T., OLAUSSEN, S., SUNDVOLL, B. & HEEREMANS, M. 2007. Vulkaner, forkastninger og ørkenklima - Osloriften og Nordsjøen i Karbon og Perm, 359-251 millioner år. *In:* RAMBERG, I. B., BRYHNI, I. & NØTTVEDT, A. (eds.) *Landet blir til : Norges geologi.* 2. oppl. med rettelser. ed. Trondheim: Norsk geologisk forening.

LASAGA, A. C. 1995. Fundamental approaches in describing mineral dissolution and precipitation rates. *Reviews in Mineralogy and Geochemistry,* 31**,** 23-86.

LAVERGREN, U., ASTROM, M. E., BERGBACK, B. & HOLMSTROM, H. 2009a. Mobility of trace elements in black shale assessed by leaching tests and sequential chemical extraction. *Geochemistry - Exploration, Environment, Analysis***,** 71-79.

LAVERGREN, U., ÅSTRÖM, M. E., FALK, H. & BERGBÄCK, B. 2009b. Metal dispersion in groundwater in an area with natural and processed black shale – Nationwide perspective and comparison with acid sulfate soils. *Applied Geochemistry,* 24**,** 359-369.

LECOMTE, A., CATHELINEAU, M., MICHELS, R., PEIFFERT, C. & BROUAND, M. 2017. Uranium mineralization in the Alum Shale Formation (Sweden): Evolution of a U-rich marine black shale from sedimentation to metamorphism. *Ore Geology Reviews,* 88**,** 71-98.

LEHNER, S., SAVAGE, K., CIOBANU, M. & CLIFFEL, D. E. 2007. The Effect of As, Co, And Ni Impurities on Pyrite Oxidation Kinetics: An Electrochemical Study of Synthetic Pyrite. *Geochim.Cosmochim.Acta 71:2491-2509,2007,* 71.

LOVDATA 2004. Forskrift om begrensning av forurensning (forurensningsforskriften), Kap. 2 §2-3.

MCMANUS, J., BERELSON, W. M., SEVERMANN, S., POULSON, R. L., HAMMOND, D. E., KLINKHAMMER, G. P. & HOLM, C. 2006. Molybdenum and uranium geochemistry in continental margin sediments: paleoproxy potential. *Geochimica et Cosmochimica Acta,* 70**,** 4643-4662.

MILJØDIREKTORATET 2016. Grenseverdier for klassifisering av vann, sediment og biota. Miljødirektoratet.

MULTICONSULT 2014. Kjernelogging, kartlegging av alunskifer - E16 Eggemoen-Olum. Unpublished.

NAKREM, H. A. & WORSLEY, D. 2007. Jordas eldste oldtid - Kambrium, Ordovicium og Silur - Et yrende liv i havet; 542-416 millioner år. *In:* RAMBERG, I. B., BRYHNI, I. & NØTTVEDT, A. (eds.) *Landet blir til : Norges geologi.* 2. oppl. med rettelser. ed. Trondheim: Norsk geologisk forening.

NESSE, W. D. 2012. *Introduction to mineralogy,* New York, Oxford University Press.

NGI 2015. M310/2015 Identifisering og karakterisering av syredannende bergarter - Veileder for Miljødirektoratet.

NICHOLSON, R. V. & SCHARER, J. M. 1993. Laboratory Studies of Pyrrhotite Oxidation Kinetics. *In:* ALPERS, C. N. & BLOWES, D. W. (eds.) *Environmental Geochemistry of Sulfide Oxidation.* American Chemical Society.

NORDSTROM, D. K. 2011. Sulfide Mineral Oxidation. *In:* REITNER, J. & THIEL, V. (eds.) *Encyclopedia of Geobiology.* Dordrecht: Springer Netherlands.

NPRA. 2016a. *Fakta om Rv. 4 Hadeland* [Online]. Available: http://www.vegvesen.no/vegprosjekter/rv4hadeland/Fakta [Accessed 6.2 2017].

NPRA. 2016b. *NORWAT* [Online]. Available: http://www.vegvesen.no/en/professional/Research+and+development/NORWAT [Accessed 6.2 2017].

NRPA. 2016. *Radon - Helserisiko* [Online]. Available: http://www.nrpa.no/fakta/89866/helserisiko [Accessed 6.2 2017].

OFTEDAHL, C. 1955. On the sulphides of the alum shale in Oslo. *Norsk Geologisk Tidsskrift,* 35**,** 117-120.

OWEN, A. W., BRUTON, D. L., BOCKELIE, F. J. & BOCKELIE, T. G. 1990. The Ordovician successions of the Oslo Region, Norway. *Norges Geologiske Undersøkelse Special publication 4.* Trondheim.

PALANDRI, J. L. & KHARAKA, Y. K. 2004. A Compilation of Rate Parameters of Water-Mineral Interaction Kinetics for Application to Geochemical Modelling. California: USGS.

PAPADOPOULOS, P. & ROWELL, D. L. 1988. The reactions of cadmium with calcium carbonate surfaces. *Journal of Soil Science,* 39**,** 23-36.

PEACOCK, C. L. & SHERMAN, D. M. 2004. Vanadium (V) adsorption onto goethite (α-FeOOH) at pH 1.5 to 12: a surface complexation model based on ab initio molecular geometries and EXAFS spectroscopy. *Geochimica et Cosmochimica Acta,* 68**,** 1723-1733.

PINGITORE, N. E., LYTLE, F. W., DAVIES, B. M., EASTMAN, M. P., ELLER, P. G. & LARSON, E. M. 1992. Mode of incorporation of Sr2+ in calcite: Determination by X-ray absorption spectroscopy. *Geochimica et Cosmochimica Acta,* 56**,** 1531-1538.

PUURA, E., NERETNIEKS, I. & KIRSIMÄE, K. 1999. Atmospheric oxidation of the pyritic waste rock in Maardu, Estonia. 1 field study and modelling. *International Journal of Geosciences,* 39**,** 1-19.

RIMSTIDT, J. D., BALOG, A. & WEBB, J. 1998. Distribution of trace elements between carbonate minerals and aqueous solutions. *Geochimica et Cosmochimica Acta,* 62**,** 1851-1863.

RIMSTIDT, J. D. & BARNES, H. L. 1980. The kinetics of silica-water reactions. *Geochimica et Cosmochimica Acta,* 44**,** 1683-1699.

RIMSTIDT, J. D. & VAUGHAN, D. J. 2003. Pyrite oxidation: a state-of-the-art assessment of the reaction mechanism. *Geochimica et Cosmochimica Acta,* 67**,** 873-880.

RUDNICK, R. L. & GAO, S. 2004. 3.01 Composition of the Continental Crust. *In:* RUDNICK, R. L., HOLLAND, H. D. & TUREKIAN, K. K. (eds.) *Treatise on geochemistry : Vol. 3 : The Crust.* Amsterdam: Elsevier.

SCHOENE, B. 2013. U–Th–Pb Geochronology. *In:* HOLLAND, H. D. & TUREKIAN, K. K. (eds.) *Treatise on Geochemistry 2nd edition.* Oxford: Elsevier.

SHOKES, T. E. & MÖLLER, G. 1999. Removal of Dissolved Heavy Metals from Acid Rock Drainage Using Iron Metal. *Environmental Science & Technology,* 33**,** 282-287.

SKIPPERUD, L., ALVARENGA, E., LIND, O. C., TEIEN, H. C., TOLLEFSEN, K. E., SALBU, B. & WÆRSTED, F. M. 2016. Effekter og miljørisiko knyttet til inngrep i områder med sulfidrike mineraler - Deponi i forbindelse med tunnelbygging i alunskiferområder. Statens vegvesen.

SWANSON, V. E. 1961. Geology and geochemistry of uranium in marine black shales: a review. *Geological Survey Professional Paper 356-C.* USGS.

TOURTELOT, H. A. 1979. Black shale - Its deposition and diagenesis. *Clays and clay minerals,* 27**,** 313-321.

TRIVEDI, P. & AXE, L. 1999. A Comparison of Strontium Sorption to Hydrous Aluminum, Iron, and Manganese Oxides. *Journal of Colloid and Interface Science,* 218**,** 554-563.

UIO 2013. Ion Chromatography of Sodium, Magnesium, Potassium and Calcium with Suppression of Eluent. University of Oslo: Department of Geosciences.

UIO 2016. Ion Chromatography of Fluoride, Chloride, Bromide, Nitrate, Sulfate, and Phosphate with Suppression of Eluent. University of Oslo.

VOKES, F. M. 1993. The metamorphism of pyrite and pyritic ores: an overview. *Mineralogical Magazine,* 57**,** 3-18.

WEISENER, C. G., SMART, R. S. T. C. & GERSON, A. R. 2003. Kinetics and mechanisms of the leaching of low Fe sphalerite. *Geochimica et Cosmochimica Acta,* 67**,** 823-830.

WHO. 2012. *Uranium in drinking water - Background document for development of WHO Guidelines for Drinking-water Quality* [Online]. Available: http://www.who.int/water_sanitation_health/publications/2012/background_uranium.p df [Accessed 26.05.2017.

WILLIAMSON, M. A. & RIMSTIDT, J. D. 1994. The kinetics and electrochemical rate-determining step of aqueous pyrite oxidation. *Geochimica et Cosmochimica Acta,* 58**,** 5443-5454.

WOLF, R. E. 2005. *What is ICP-MS?* [Online]. USGS. Available: https://crustal.usgs.gov/laboratories/icpms/intro.htm [Accessed 12 February 2017].

YU, C., LAVERGREN, U., PELTOLA, P., DRAKE, H., BERGBÄCK, B. & ÅSTRÖM, M. E. 2014. Retention and transport of arsenic, uranium and nickel in a black shale setting revealed by a long-term humidity cell test and sequential chemical extractions. *Chemical Geology,* 363**,** 134-144.

Appendix

Appendix I – Threshold limits for environmental quality in freshwater

Threshold values for selected heavy metals. *Cd classification depends on water hardness.
Table modified from (Miljødirektoratet, 2016).

Element	Class I Background	Class II Good	Class III Moderate	Class IV Poor	Class V Very poor
Cd	0.003	≤0.08 - 0.25*	≤0.45 - 1.5*	≤4.5 - 15*	>15
Pb	0.02	1.2	14	57	>57
Ni	0.5	4	34	67	>67
Cu	0.3	7.8	7.8	15.6	>15.6
Zn	1.5	11	11	60	>60
As	0.15	0.5	8.5	85	>85
Cr	0.1	3.4	3.4	3.4	>3.4

Appendix II: Trace element and anion/cation data from NPRA (All tables modified from Fjermestad et al. (2017))

Trace element concentrations from Bulk experiment 1 and 2. All units in µg/l.

	Al	V	Cr	Fe	Co	Ni	Cu	Zn	Sr	Mo	Cd	Pb	U	pH
A1														
14.10.2014	7.76	1.30	0.45	3.90	0.60	23.40	0.90	1.90	510.00	1280.00	1.85	0.09	1070.00	8.92
22.10.2014	20.70	0.94	0.20	7.90	1.22	33.20	1.90	7.36	593.00	1430.00	1.37	0.19	1760.00	8.04
30.10.2014	12.20	0.87	0.10	3.90	0.82	29.10	0.90	4.31	560.00	1550.00	2.28	0.09	1270.00	8.48
12.11.2014	13.10	0.69	0.20	7.90	0.99	42.70	1.90	19.20	689.00	1870.00	3.16	0.19	1550.00	8.32
26.11.2014	9.84	0.72	0.20	7.90	1.78	72.30	1.90	3.90	803.00	2330.00	3.74	0.19	1600.00	8.93
11.03.2015	3.89	0.52	0.05	1.90	1.78	74.30	0.49	4.79	557.00	1420.00	2.74	0.05	1600.00	7.61
19.05.2015	3.56	0.37	0.05	1.90	4.05	235.00	0.49	20.60	1450.00	3250.00	2.09	0.05	1210.00	8.38
A3														
08.10.2014	9.9	0.451	0.049	19.9	12.6	289	4.9	9.9	2660	6260	6.82	0.49	2500	7.68
14.10.2014	19.9	0.49	0.9	19.9	13.6	344	7.59	18.8	2880	6460	10.7	0.9	3170	8.4
22.10.2014	33.2	0.49	0.9	19.9	15.5	303	6.9	13.2	2580	8120	6.21	0.9	3080	8.07
30.10.2014	19.9	0.507	6.73	19.9	16.2	443	6.9	25	3450	10400	18.5	0.9	2890	8.1
12.11.2014	19.9	0.618	0.9	19.9	37.4	1180	11.4	70.6	5350	9770	18.4	0.9	4370	7.61
26.11.2014	9.9	0.517	0.49	19.9	68.4	2210	11.5	134	5290	5660	9.74	0.49	5180	8.24
11.03.2015	1.42	0.176	0.049	1.9	88.5	1390	0.49	78.1	1550	1090	3.24	0.049	3250	6.8
19.05.2015	8.97	0.359	0.597	19	80.4	2150	12.1	73.1	6130	1450	2.16	0.76	4850	8.37
A2K														
08.10.2014	13.80	0.88	0.49	392.00	11.10	385.00	5.20	9.90	3040.00	7930.00	7.42	0.49	4270.00	7.60
14.10.2014	19.90	1.06	4.59	403.00	19.60	542.00	21.30	24.70	3410.00	7690.00	11.60	0.90	6340.00	7.41
22.10.2014	29.50	0.77	0.49	306.00	14.00	392.00	19.70	10.20	2390.00	6470.00	4.99	0.49	5660.00	8.32
30.10.2014	9.90	0.47	0.49	133.00	9.59	296.00	4.90	14.80	1910.00	6640.00	10.10	0.49	4570.00	8.11
12.11.2014	19.90	0.49	0.90	61.60	11.50	293.00	11.40	57.90	2200.00	8870.00	15.10	0.90	4120.00	7.89
26.11.2014	19.90	0.49	0.90	24.10	12.20	356.00	9.37	22.40	2440.00	11900.00	15.70	0.90	3660.00	8.51
19.05.2015	1.90	0.34	0.09	3.90	77.80	2130.00	0.90	168.00	5820.00	5200.00	5.66	0.09	5290.00	8.19

Trace element concentrations from Bulk experiment 1 and 2. All units in µg/l.

AT1	Al	V	Cr	Fe	Co	Ni	Cu	Zn	Sr	Mo	Cd	Pb	U	pH
28.05.2015	38.50	450.00	13.70	19.90	0.29	2.87	9.90	9.90	2110.00	21900.00	24.60	0.49	103.00	10.47
04.06.2015	26.10	300.00	12.30	19.90	0.29	12.10	9.90	9.90	5140.00	30800.00	23.50	0.49	225.00	9.15
11.06.2015	13.60	50.80	1.88	7.90	0.36	41.90	1.90	28.00	6530.00	14600.00	16.80	0.19	267.00	7.42
18.06.2015	10.20	8.84	0.35	7.90	0.09	78.30	1.90	16.00	7560.00	9130.00	7.58	0.19	325.00	7.43
AT2														
28.05.2015	263.00	516.00	31.40	26.40	0.29	2.90	9.90	9.90	3510.00	26500.00	27.40	0.49	0.04	12.13
04.06.2015	201.00	366.00	12.80	19.90	0.29	2.90	32.60	9.90	4780.00	20300.00	18.50	0.71	0.13	10.06
11.06.2015	71.40	145.00	1.30	7.90	0.09	2.96	1.90	3.90	7490.00	15100.00	16.80	0.19	43.70	8.89
18.06.2015	20.30	33.10	0.51	7.90	0.09	15.50	1.90	10.60	8300.00	11200.00	8.74	0.19	97.60	8.15
AT3k														
28.05.2015	80.5	494	7.67	19.9	0.29	2.9	4.9	9.9	2780	22900	26.1	0.49	22.3	10.68
04.06.2015	76	312	8.09	19.9	0.29	7.74	4.9	9.9	4990	21200	18.3	0.49	141	8.96
11.06.2015	26.9	75.7	2.63	7.9	0.228	37.9	1.9	3.9	6210	12600	15.2	0.19	238	8.04
18.06.2015	9.66	10.9	0.376	7.9	0.09	60	1.9	10.5	7130	9050	8.21	0.19	276	7.86
AT4k														
28.05.2015	85.90	369.00	13.00	19.90	0.29	2.90	4.90	9.90	2400.00	22600.00	26.70	0.49	6.74	10.62
04.06.2015	112.00	318.00	15.60	19.90	0.29	3.41	4.90	9.90	5150.00	27300.00	24.20	0.49	30.60	8.95
11.06.2015	34.90	48.00	1.03	7.90	0.46	25.40	1.90	3.90	4650.00	8320.00	10.50	0.19	129.00	7.94
18.06.2015	16.70	10.80	0.31	3.90	0.49	52.50	0.90	11.10	4320.00	5070.00	4.69	0.09	238.00	7.95

Anion/cation concentrations from Bulk experiment 1 and 2. All units in mg/l.

A1	Na	K	Mg	Ca	Cl	SO4
14.10.2014	6.73	4.15	1.93	38.8	<1	64.4
22.10.2014	5.04	3.69	2.33	46.7	<1	75.4
30.10.2014	3.77	3.88	2.19	48.4	n/a	66
12.11.2014	3.5	4.24	2.71	51.5	<1	80
26.11.2014	2.98	4.33	3.08	56.2	<1	86.5
11.03.2015	2.1	3.18	1.96	51.2	<1	55
19.05.2015	2.36	5.7	4.75	148	<1	392
A3						
08.10.2014	23	14.1	19.6	375	<1	997
14.10.2014	20.4	15.1	19.4	383	<1	1090
22.10.2014	13	13	15.9	343	<1	882
30.10.2014	9.45	15.7	18.2	500	n/a	1200
12.11.2014	7.29	17.2	25.9	808	<1	1900
26.11.2014	4.61	14.6	24.8	741	3.94	1730
11.03.2015	1.35	4.52	4.98	264	1.19	508
19.05.2015	2.96	11.3	31	635	<1	1460
A2K						
08.10.2014	38	15	37.6	372	4.2	920
14.10.2014	40.7	16.3	34.9	384	3.78	1000
22.10.2014	29	11.8	24.5	268	5.91	702
30.10.2014	18.7	11	19	234	n/a	530
12.11.2014	15.5	11.2	22.6	265	<1	677
26.11.2014	10.7	11.2	26.9	277	<1	676
19.05.2015	5.88	12.5	79.2	690	<1	1710

AT1	Na	K	Mg	Ca	Cl	SO4
28.05.2015	200	9.41	3.73	16.5	3.71	348
04.06.2015	255	13.3	8.42	52.6	2.16	554
11.06.2015	170	15.2	12.9	99.2	1.31	662
18.06.2015	101	14.8	18.4	132	<1.00	615
AT2						
28.05.2015	225	9.4	0.348	58.6	3.91	366
04.06.2015	195	8.17	<0.5	81.2	1.55	534
11.06.2015	173	13.4	3.28	179	1.56	779
18.06.2015	103	14.2	9.04	232	<1.00	763
AT3K						
28.05.2015	195	7.96	1.85	27.6	2.94	382
04.06.2015	219	9.99	4.65	62	2.04	563
11.06.2015	141	14.1	10.4	136	1.9	650
18.06.2015	88.2	13.7	16.2	156	10.5	650
AT4K						
28.05.2015	193	9.27	1.45	27.5	3.95	364
04.06.2015	269	12.4	3.04	80.7	2.58	688
11.06.2015	136	13	7.44	117	1.36	601
18.06.2015	83.7	11.3	13.3	110	10	504

Trace element concentrations from Bulk experiment 1 and 2. All units in µg/l.

Group	Date	Al	V	Cr	Fe	Co	Ni	Cu	Zn	Sr	Mo	Cd	Pb	U	pH
G1	08.10.2014	162.00	72.10	0.49	19.90	0.32	2.90	4.90	9.90	377.00	5200.00	5.03	0.49	195.00	10.00
	14.10.2014	109.00	73.40	1.90	19.90	0.29	2.90	4.90	9.90	266.00	2840.00	4.48	0.49	233.00	10.20
	22.10.2014	116.00	41.90	0.49	19.90	0.63	4.59	4.90	9.90	295.00	2850.00	2.20	0.49	395.00	10.14
	30.10.2014	80.10	19.40	0.53	7.90	0.90	0.90	1.90	3.90	396.00	2360.00	3.49	0.19	521.00	9.71
	12.11.2014	46.40	6.95	0.19	7.90	0.30	1.80	1.90	7.79	541.00	3090.00	3.96	0.19	690.00	9.42
	26.11.2014	24.80	3.12	0.19	7.90	0.21	1.88	1.90	10.80	546.00	2530.00	3.77	0.19	704.00	9.71
	11.03.2015	6.22	0.24	0.05	1.90	2.18	20.00	1.90	17.10	1430.00	742.00	1.55	0.05	590.00	8.26
	19.05.2015	3.59	0.08	0.02	7.90	6.11	51.60	0.49	28.80	6700.00	1240.00	1.15	0.02	295.00	8.54
G2	08.10.2014	195.00	59.10	0.63	19.90	0.91	2.90	4.90	9.90	277.00	3880.00	4.21	0.49	799.00	10.00
	14.10.2014	113.00	52.60	1.24	7.90	0.09	1.90	1.90	3.90	320.00	1890.00	2.95	0.19	678.00	10.15
	22.10.2014	104.00	29.60	0.36	7.90	0.58	2.08	1.90	3.90	356.00	2090.00	1.52	0.19	727.00	10.08
	30.10.2014	75.60	17.60	0.28	7.90	0.16	1.58	1.90	3.90	383.00	2050.00	3.34	0.19	576.00	9.87
	12.11.2014	51.40	9.42	0.19	7.90	0.25	0.90	1.90	6.37	437.00	2620.00	3.75	0.19	598.00	9.52
	26.11.2014	36.00	4.18	0.19	7.90	0.17	1.68	1.90	10.50	430.00	2170.00	3.18	0.19	487.00	9.80
	11.03.2015	9.94	0.34	0.05	7.90	1.11	10.70	0.63	7.46	906.00	570.00	1.23	0.05	312.00	7.92
	19.05.2015	6.49	0.22	0.05	7.90	2.58	23.00	0.49	17.10	3060.00	1540.00	1.16	0.02	224.00	8.95
G3K	08.10.2014	739.00	62.60	1.51	1720.00	1.44	14.60	132.00	9.90	848.00	4040.00	4.15	4.58	2220.00	10.00
	14.10.2014	890.00	69.90	2.03	1200.00	1.05	12.80	110.00	4.37	630.00	2190.00	3.15	2.50	1790.00	9.95
	22.10.2014	550.00	45.80	0.22	489.00	0.84	7.11	35.00	7.22	353.00	1970.00	1.42	1.33	1210.00	10.22
	30.10.2014	145.00	28.20	0.38	108.00	0.37	3.16	13.30	3.90	298.00	1780.00	2.96	0.45	759.00	10.04
	12.11.2014	107.00	15.40	0.29	46.70	0.40	2.61	5.78	9.02	387.00	2550.00	3.62	0.21	707.00	9.56
	26.11.2014	67.60	8.08	0.19	37.20	0.24	1.98	2.53	5.15	395.00	2230.00	3.34	0.19	533.00	9.92
	11.03.2015	10.80	0.45	0.05	19.90	0.83	9.19	1.04	6.55	770.00	541.00	1.14	0.05	260.00	7.98
	19.05.2015	7.25	0.43	0.15	5.94	1.41	20.00	1.16	16.90	2990.00	2100.00	1.66	0.05	253.00	8.99

Anion/cation concentrations from Bulk experiment 1 and 2. All units in mg/l.

G1	Na	K	Mg	Ca	Cl	SO4
08.10.2014	521	15.4	1.15	2.38	4.9	390
14.10.2014	434	13.4	1.02	2.03	3.46	279
22.10.2014	454	14.3	1.19	1.73	2.64	328
30.10.2014	472	16.9	1.88	2.59	n/a	560
12.11.2014	512	20	2.96	3.82	2.42	781
26.11.2014	501	21.2	3.58	4.02	<1	646
11.03.2015	344	27.1	13.6	19.2	1.36	494
19.05.2015	665	67.4	78.1	102	1.07	2320
G2						
08.10.2014	457	15.3	1.56	1.86	5.79	198
14.10.2014	444	15.5	1.72	2	1.96	152
22.10.2014	468	16.7	2.15	2.18	<1	259
30.10.2014	434	17.4	2.56	2.58	n/a	310
12.11.2014	454	19.5	3.3	3.21	<1	481
26.11.2014	425	19.8	3.68	3.17	1.13	406
11.03.2015	303	21.7	9.28	11.3	<1	255
19.05.2015	476	47.8	37.5	38.9	<1	1500
G3K						
08.10.2014	572	18.7	4.15	6.75	11.9	287
14.10.2014	534	17.4	3.19	4.83	6.87	198
22.10.2014	450	15	2.15	2.99	2.12	175
30.10.2014	381	14.7	1.87	2.71	n/a	280
12.11.2014	429	16.6	2.51	3.4	1.39	444
26.11.2014	414	17.3	2.79	3.4	1.11	382
11.03.2015	249	17.5	8.28	10.3	<1	229
19.05.2015	576	46.1	33.4	37.9	<1	1580

Appendix III: R-code

```
#install "Hmisc" package for correlation and p-value calculation

>install.packages("Hmisc")

#load "Hmisc" library

>library("Hmisc")

#import .txt file with matrix data

>my_data <- read.delim(file.choose())

#perform spearman correlation and p-value calculation on matrix

>res2 <- rcorr(as.matrix(my_data), type =c("spearman"))

#display correlation matrix and p-value matrix

>res2
```

Appendix IV –I: SEM images of alum shale
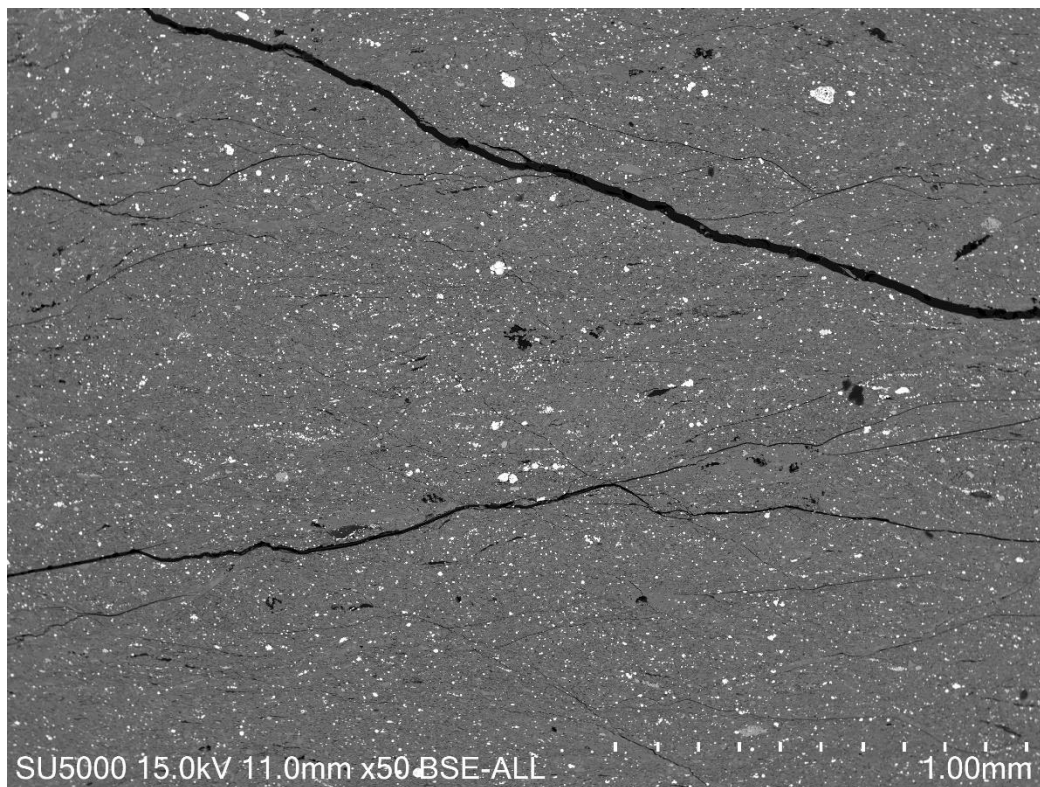
Sample A1
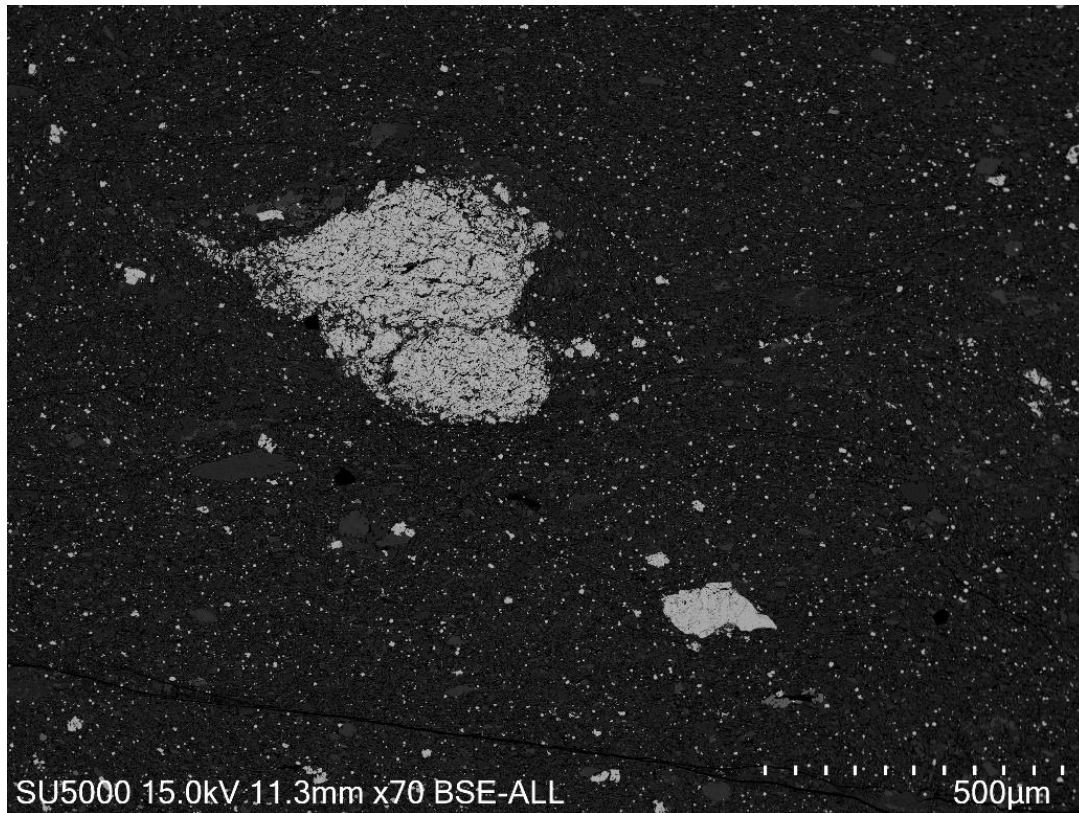
Sample A3
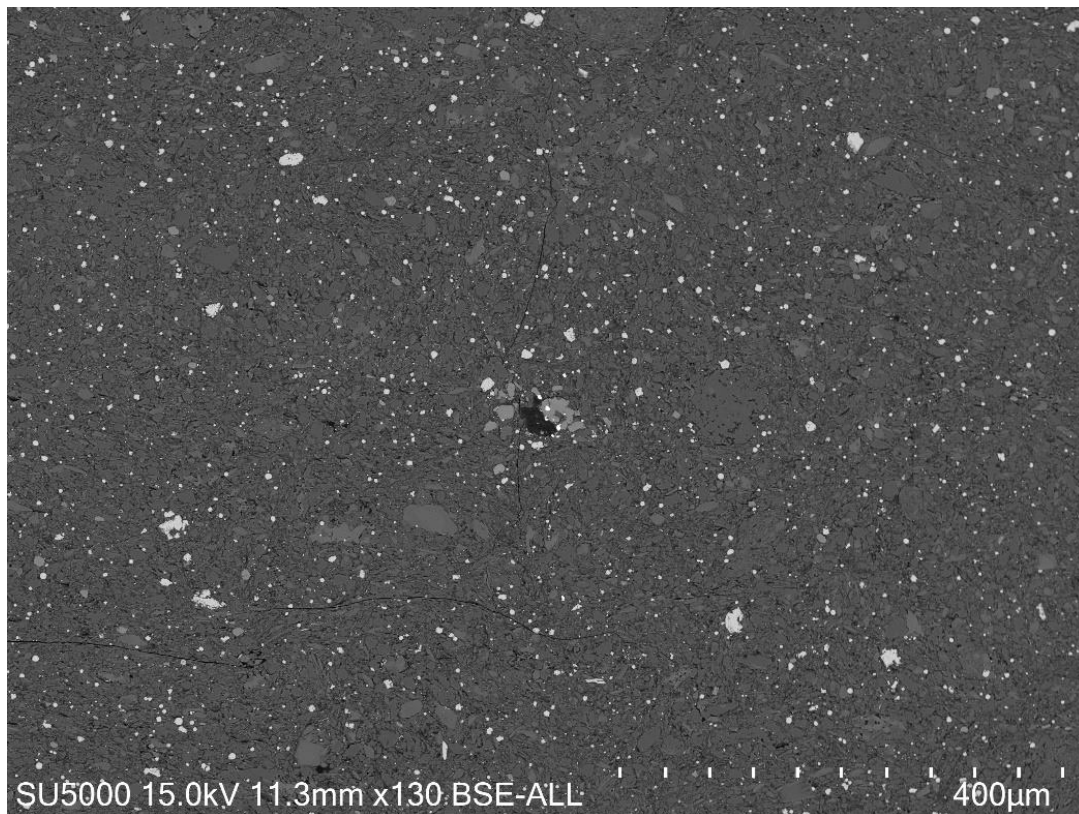
Sample AT1
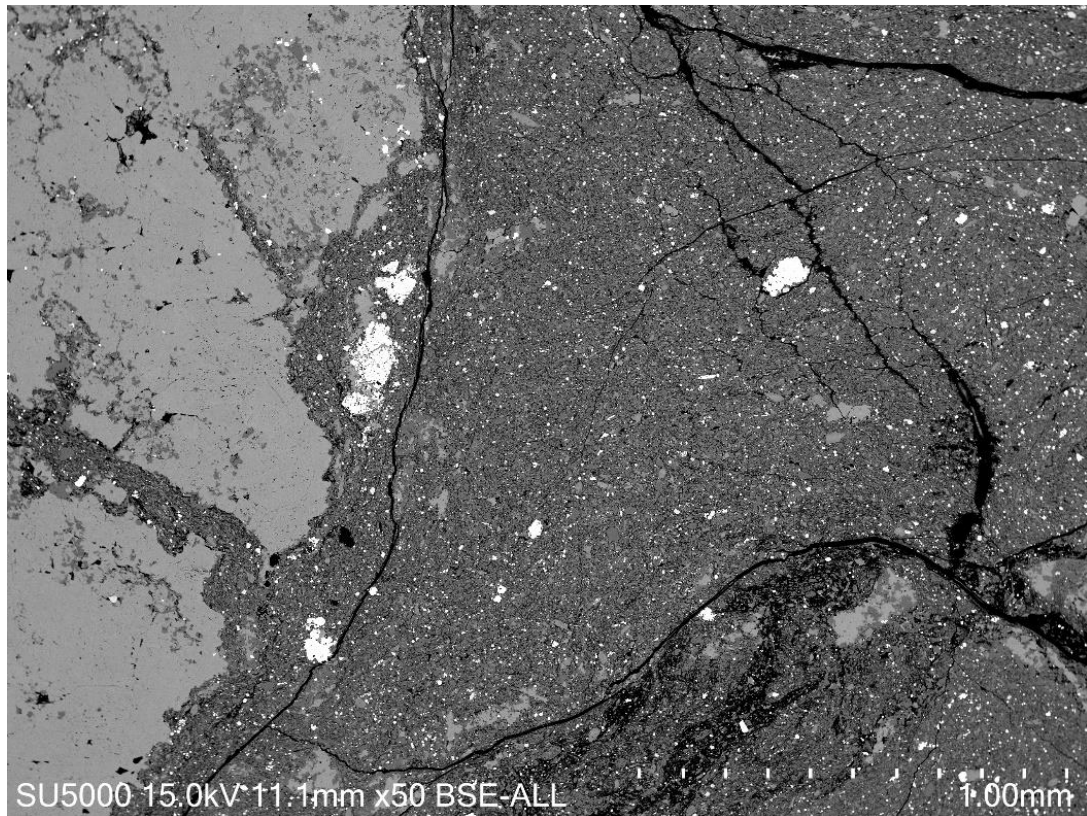
Sample AT4K

Alum shale: sphalerite
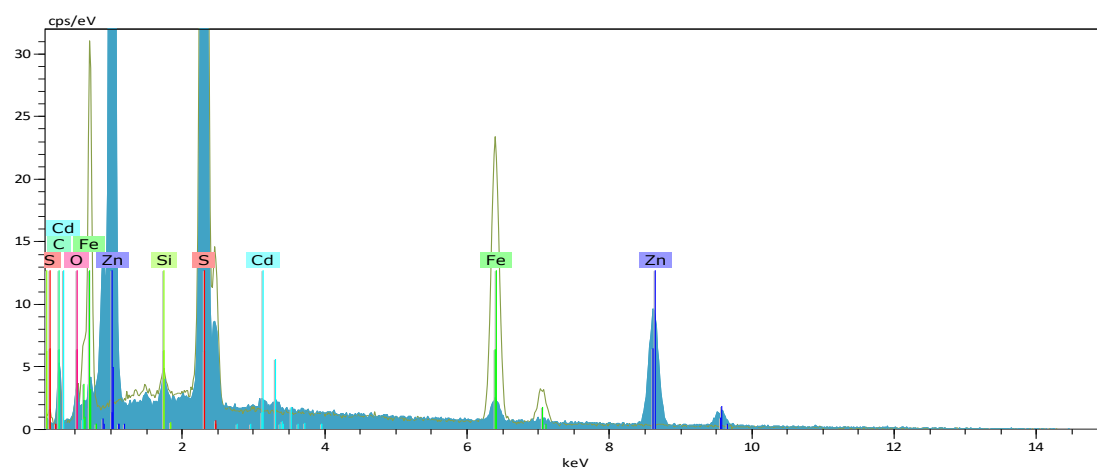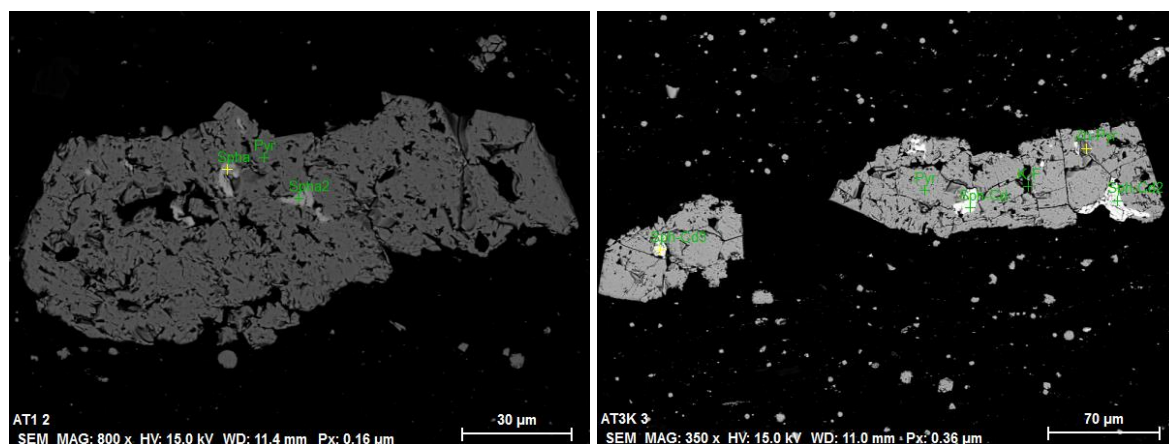
AT1 Spha   Date:22/02/2017 14:40:27   HV:15.0kV   Puls th.:39.43kcps
AT1 Pyr   Date:22/02/2017 14:40:35   HV:15.0kV   Puls th.:38.15kcps
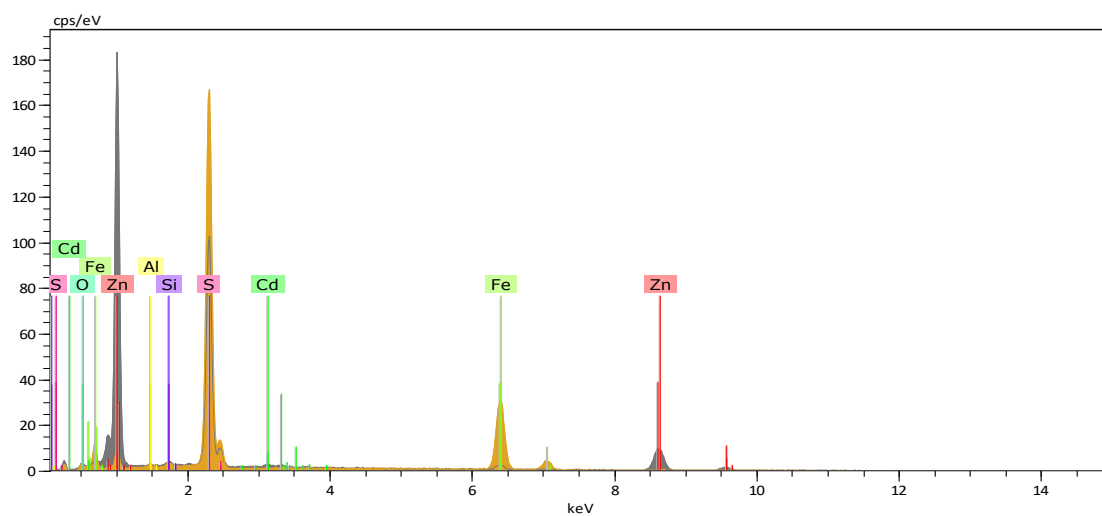
AT3K Zn-Pyr   Date:22/03/2017 13:10:59   HV:15.0kV   Puls th.:38.37kcps
AT3K Sph-Cd3   Date:22/03/2017 13:11:13   HV:15.0kV   Puls th.:44.07kcps

106

Alum shale: monazite
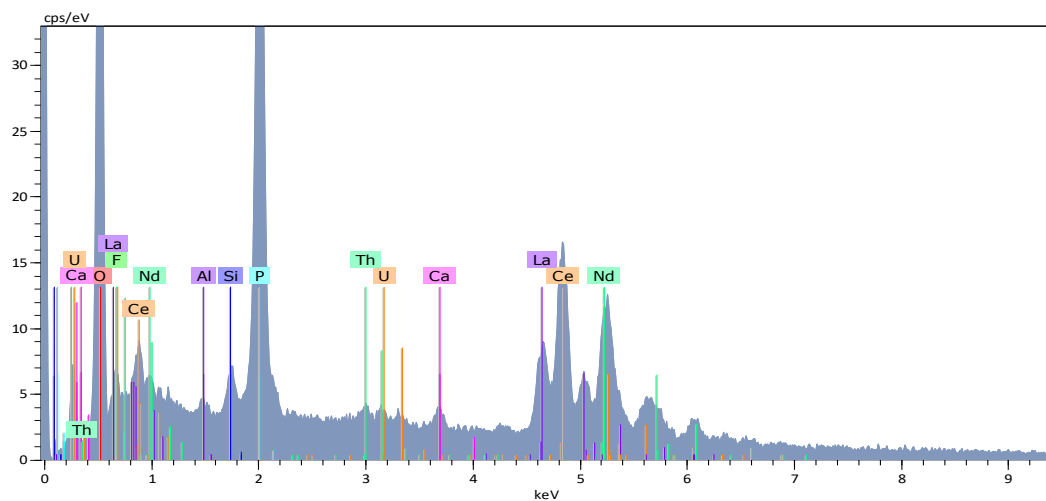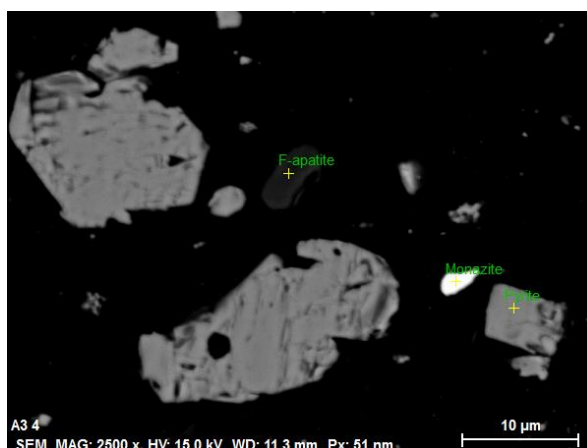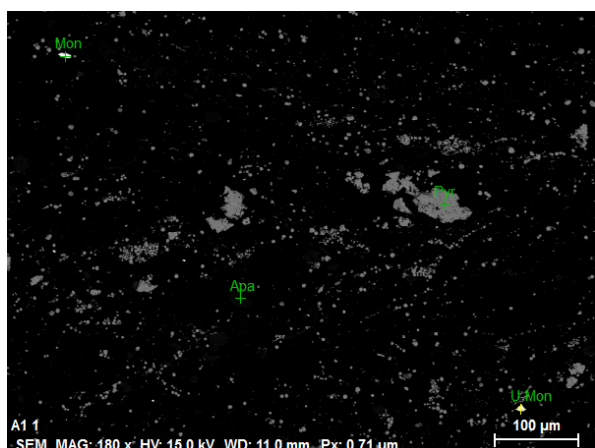
A1 U-Mon   Date:22/03/2017 13:47:14   HV:15.0kV   Puls th.:41.64kcps
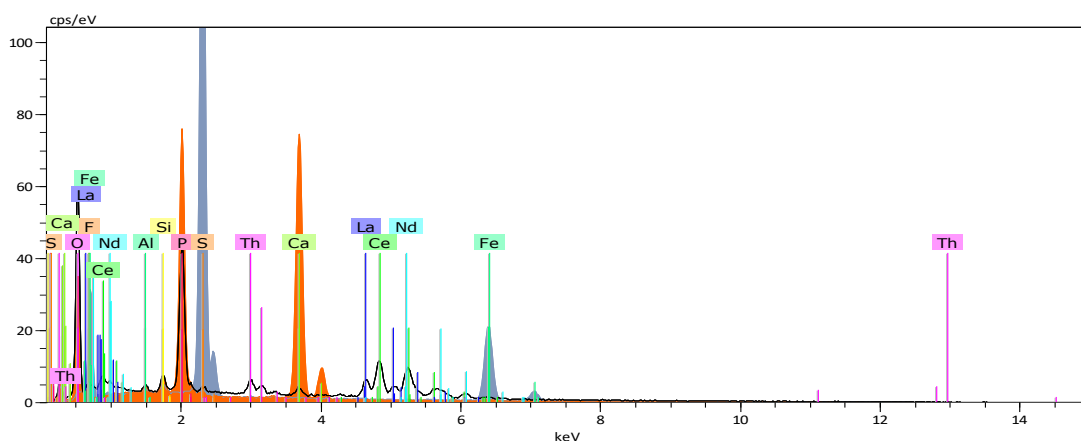
A3 Monazite   Date:22/02/2017 09:46:35   HV:15.0kV   Puls th.:35.41kcps
A3 F-apatite   Date:22/02/2017 09:46:43   HV:15.0kV   Puls th.:32.21kcps
A3 Pyrite   Date:22/02/2017 09:46:52   HV:15.0kV   Puls th.:38.03kcps

107
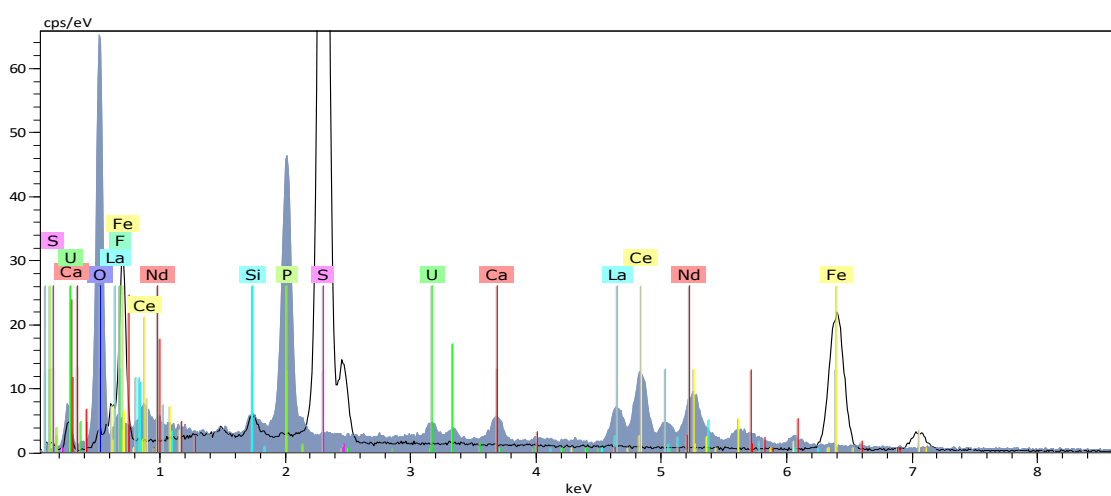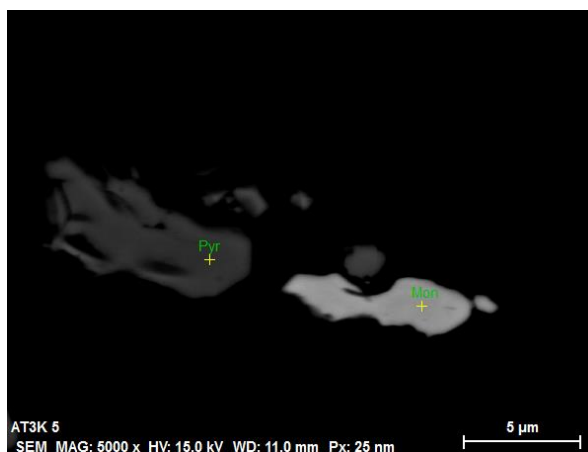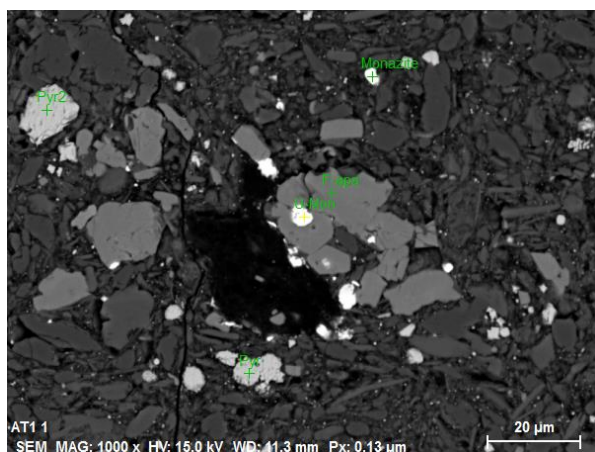
AT1 U-Mon   Date:22/02/2017 14:27:38   HV:15.0kV   Puls th.:35.05kcps
AT1 Pyr   Date:22/02/2017 14:27:47   HV:15.0kV   Puls th.:37.57kcps
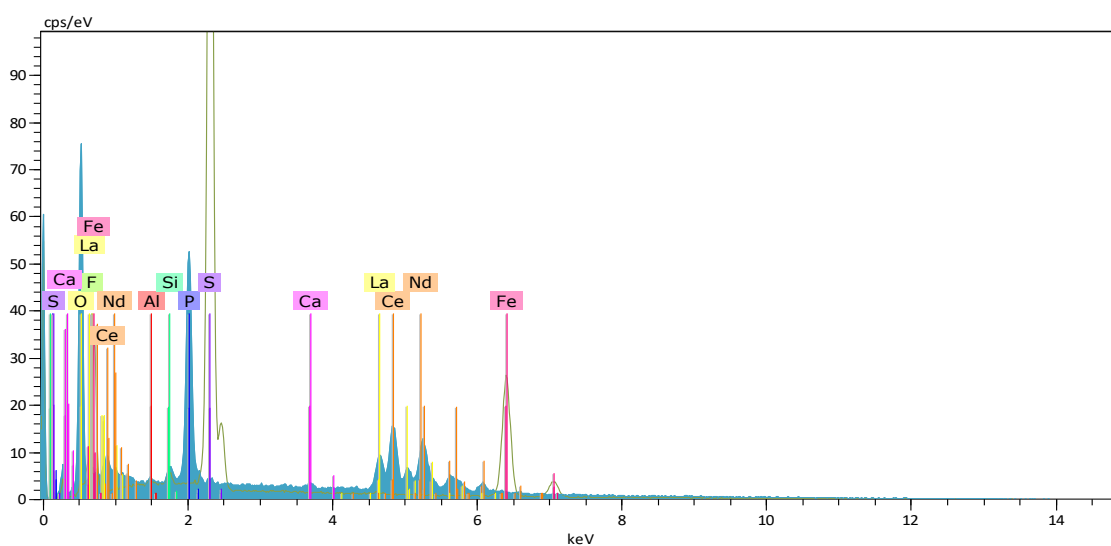
AT3K Mon   Date:22/03/2017 13:27:14   HV:15.0kV   Puls th.:41.57kcps
AT3K Pyr   Date:22/03/2017 13:27:21   HV:15.0kV   Puls th.:42.91kcps

108

Galgeberg shale: monazite
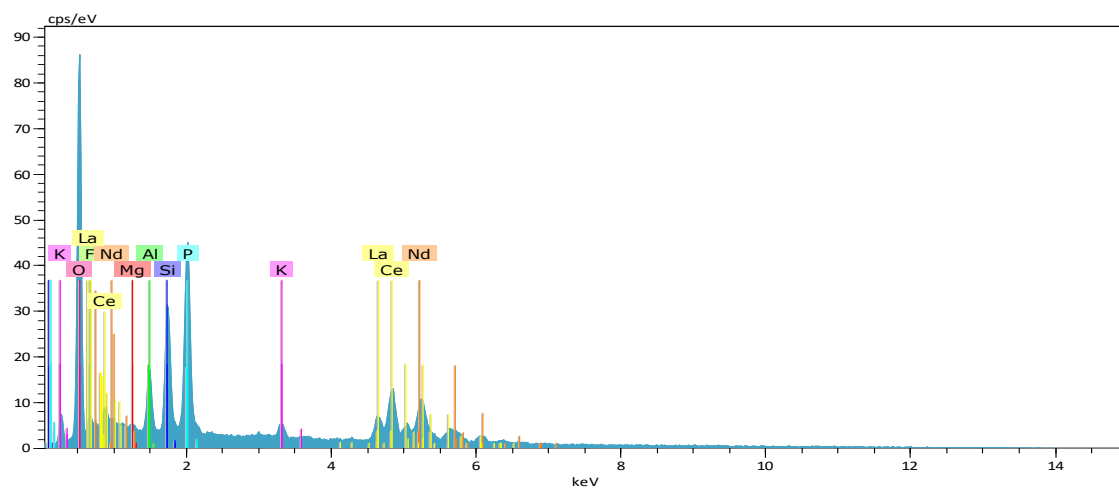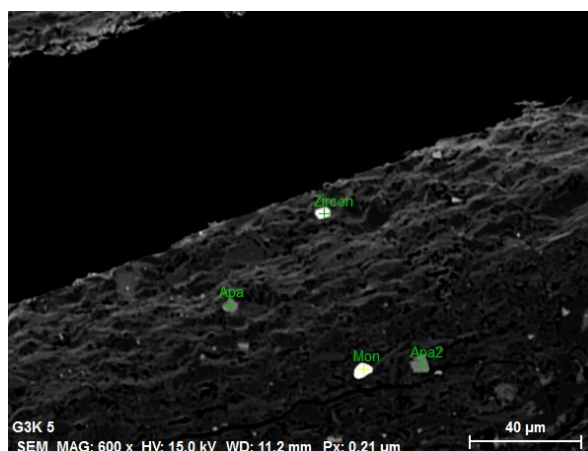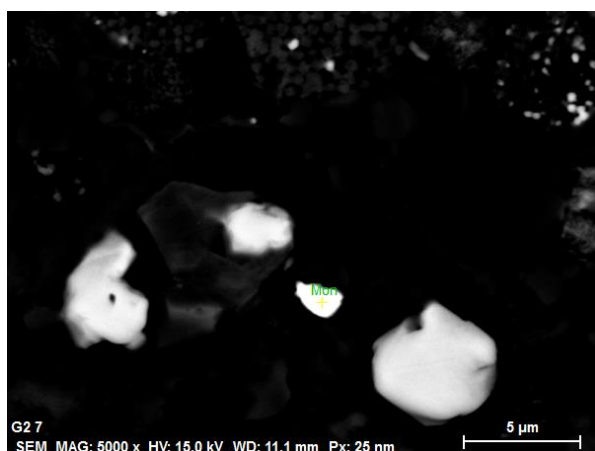
G2 Mon   Date:22/03/2017 10:01:49   HV:15.0kV   Puls th.:42.43kcps
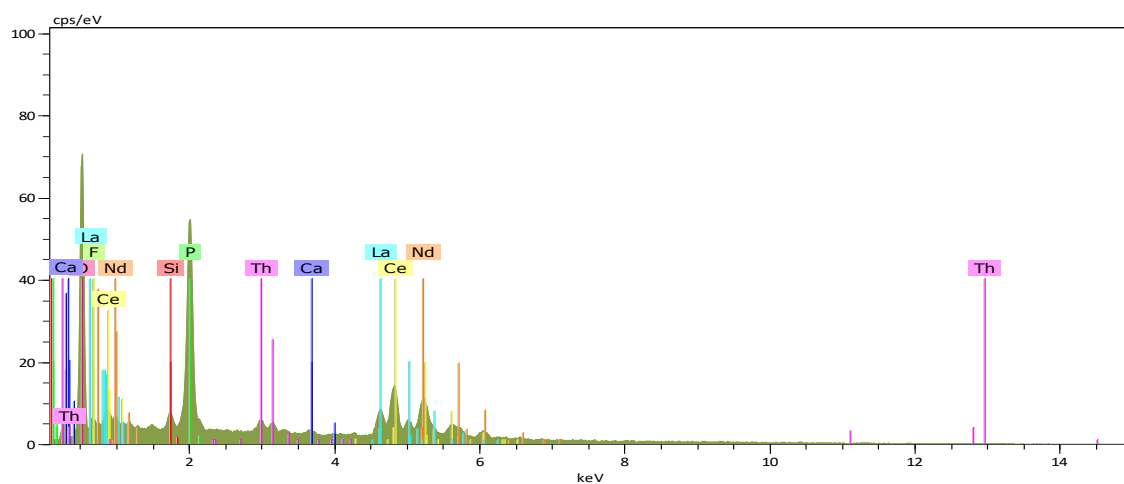
G3K Mon   Date:23/03/2017 14:01:17   HV:15.0kV   Puls th.:41.50kcps

Galgeberg shale: xenotime

G2 3
SEM MAG: 600 x HV: 15.0 kV WD: 11.1 mm Px: 0.21 µm

40 µm
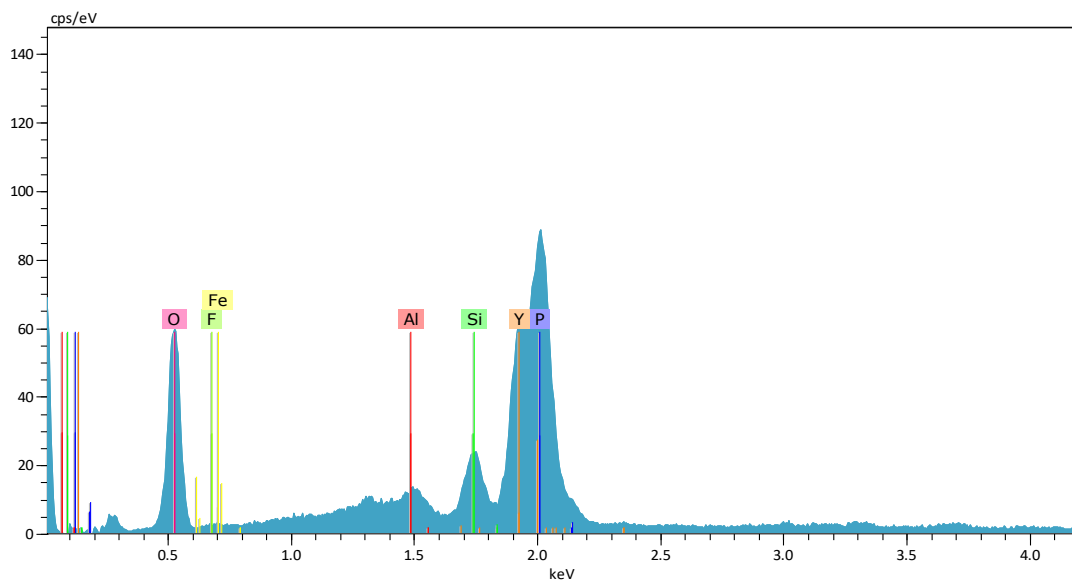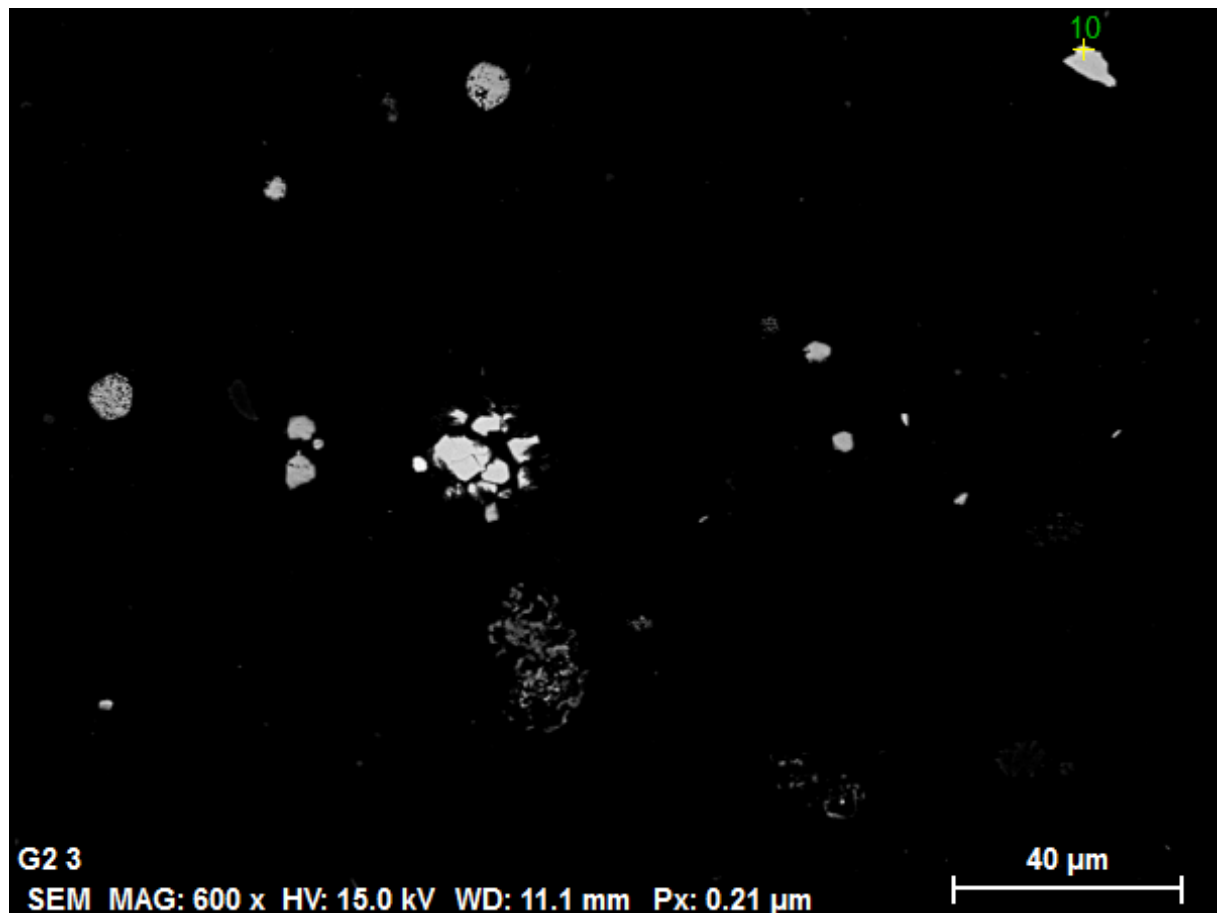
G2 10   Date:22/03/2017 09:32:03   HV:15.0kV   Puls th.:43.07kcps

110

Galgeberg shale: sphalerite and chalcopyrite
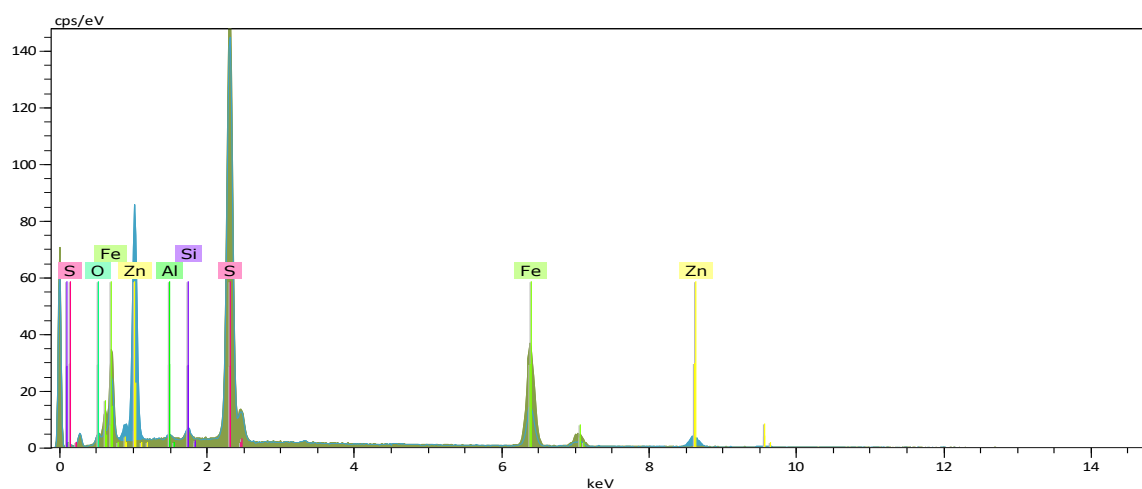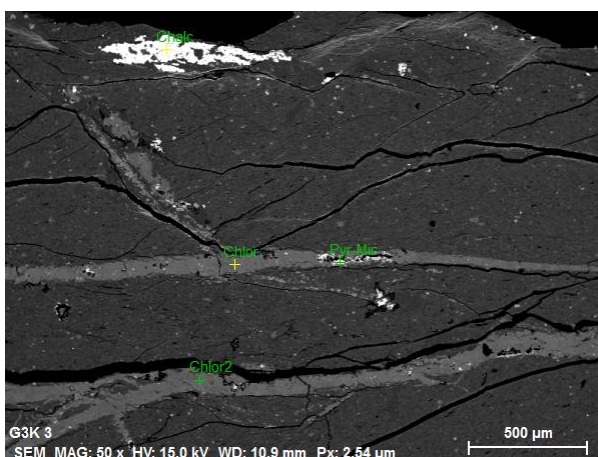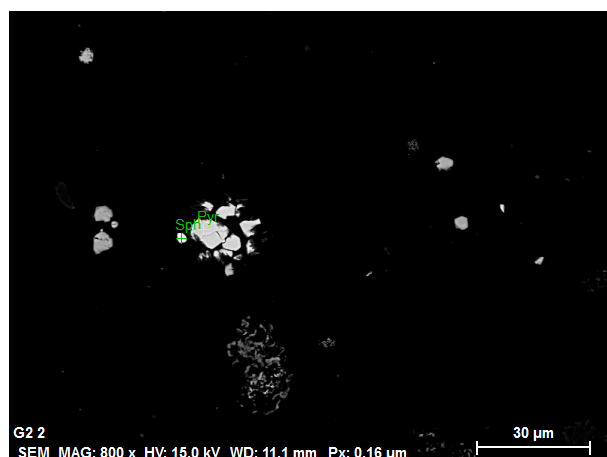
G2 Sph Date:22/03/2017 09:27:10   HV:15.0kV   Puls th.:43.82kcps
G2 Pyr Date:22/03/2017 09:27:16   HV:15.0kV   Puls th.:43.01kcps
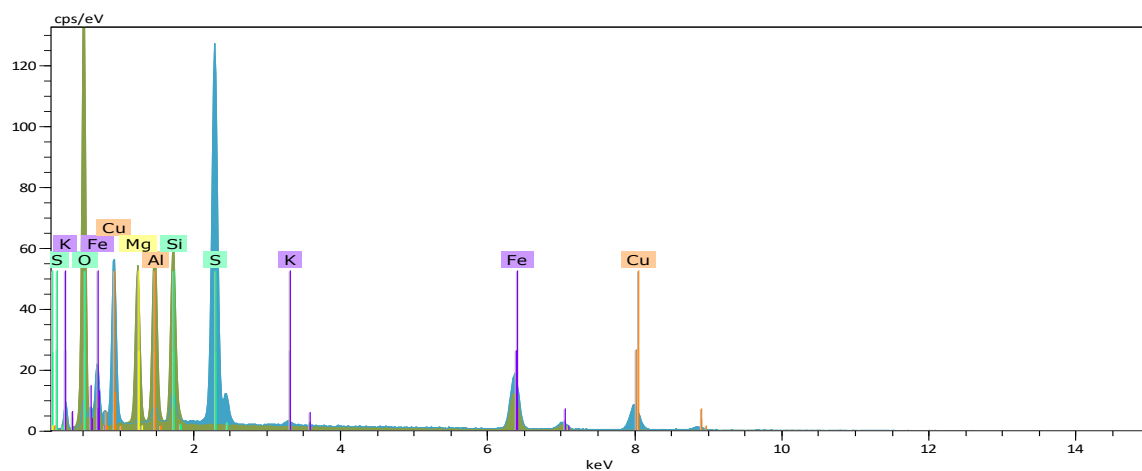
G3K Chalc   Date:23/03/2017 13:49:47   HV:15.0kV   Puls th.:43.19kcps
G3K Chlor   Date:23/03/2017 13:49:54   HV:15.0kV   Puls th.:39.96kcps

Appendix IV-III: Reflected light microscopy photos of BH1N
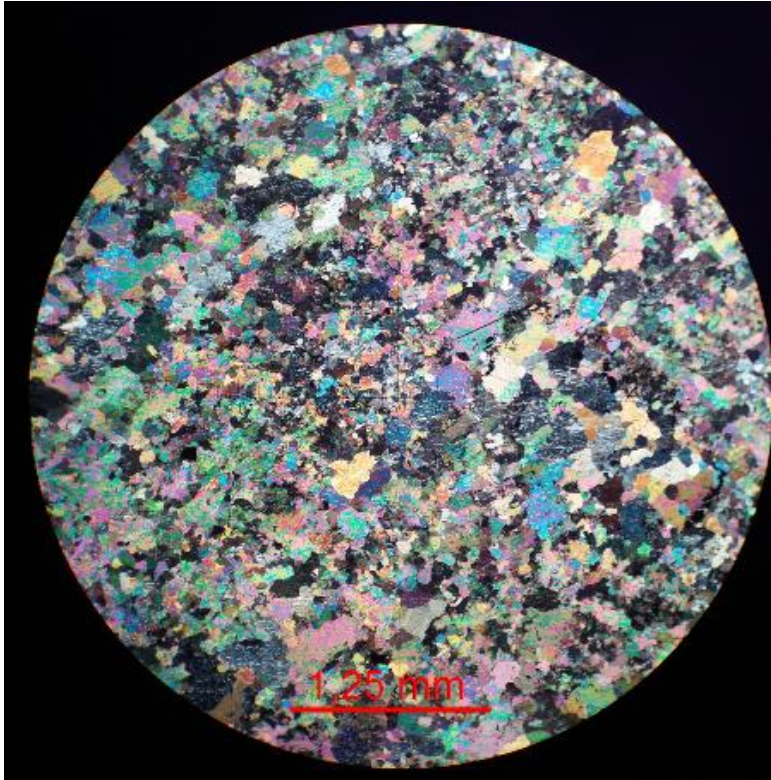
BH1N – 1m, taken at 4x magnification
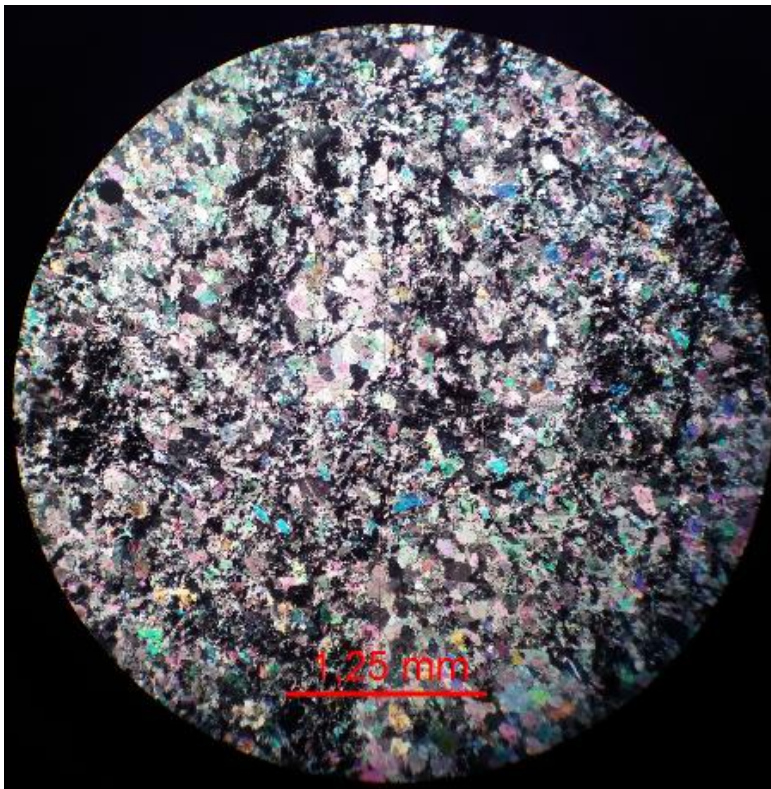
BH1N – 8m, taken at 4x magnification

Appendix IV-IV: SEM images of BH1N
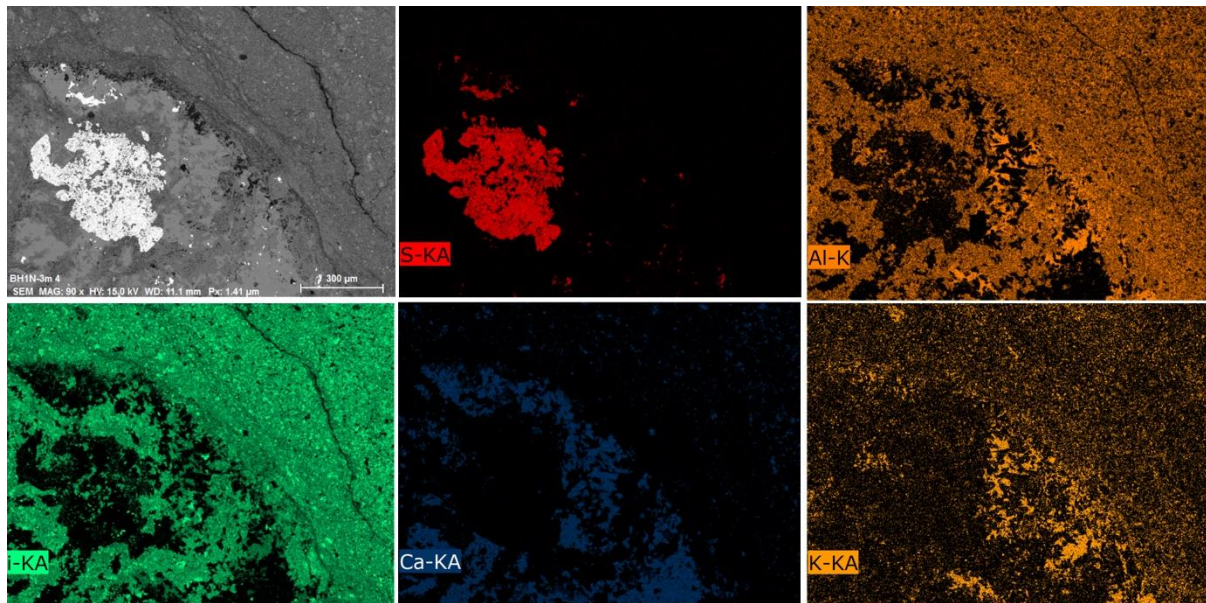
Mapping of BH1N – 3 m
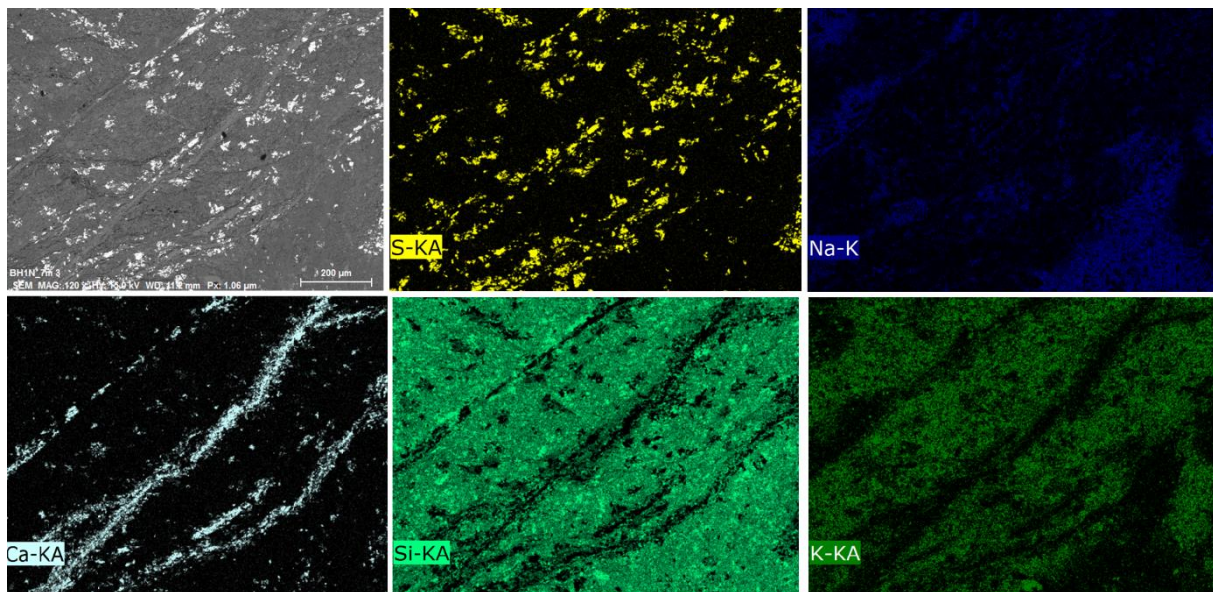
Mapping of BH1N – 7 m, images taken at 120x magnification.
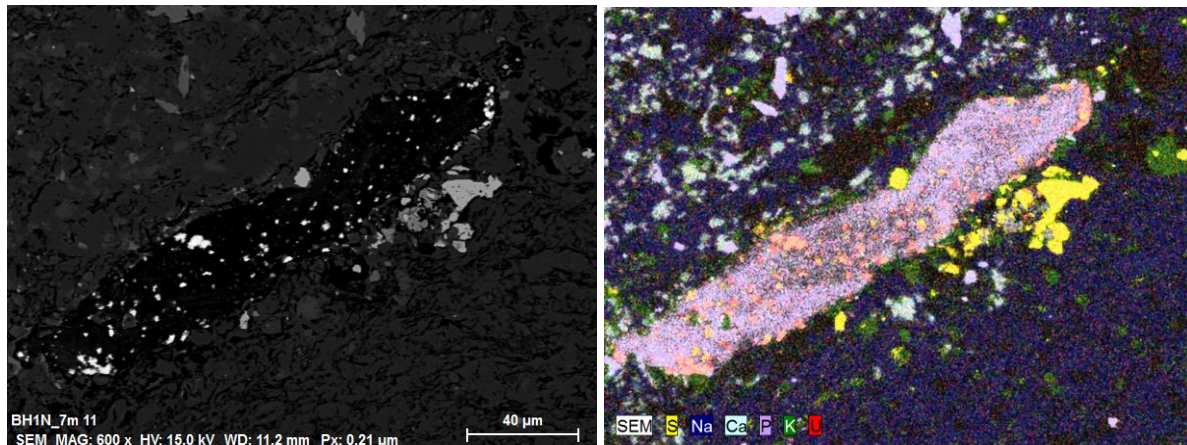
Mapping of apatite with U-bearing phosphates in BH1N – 7 m

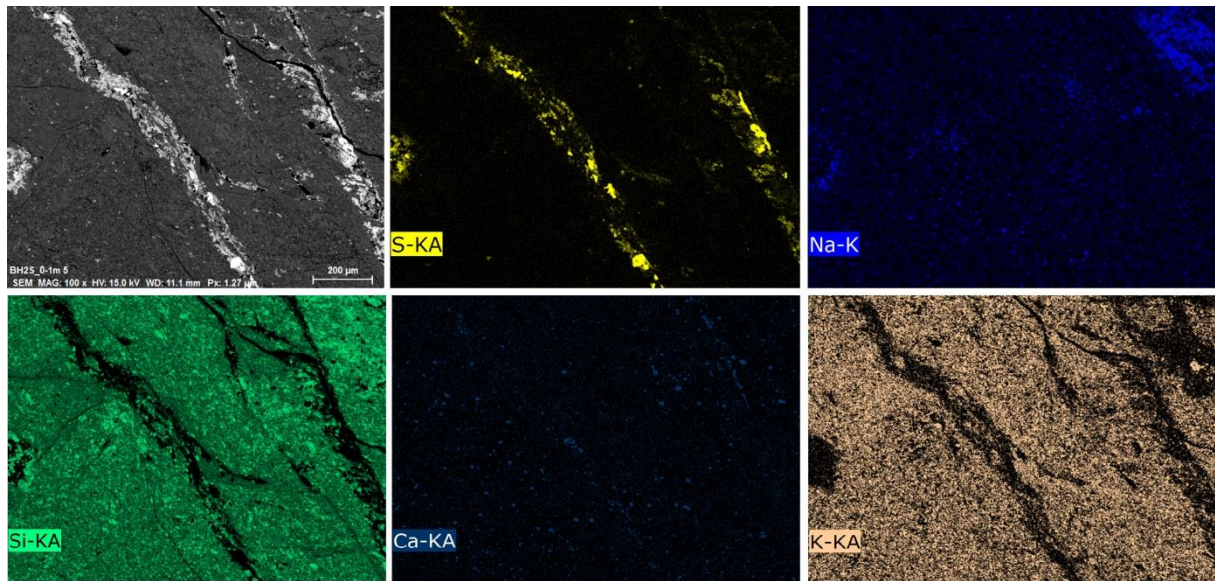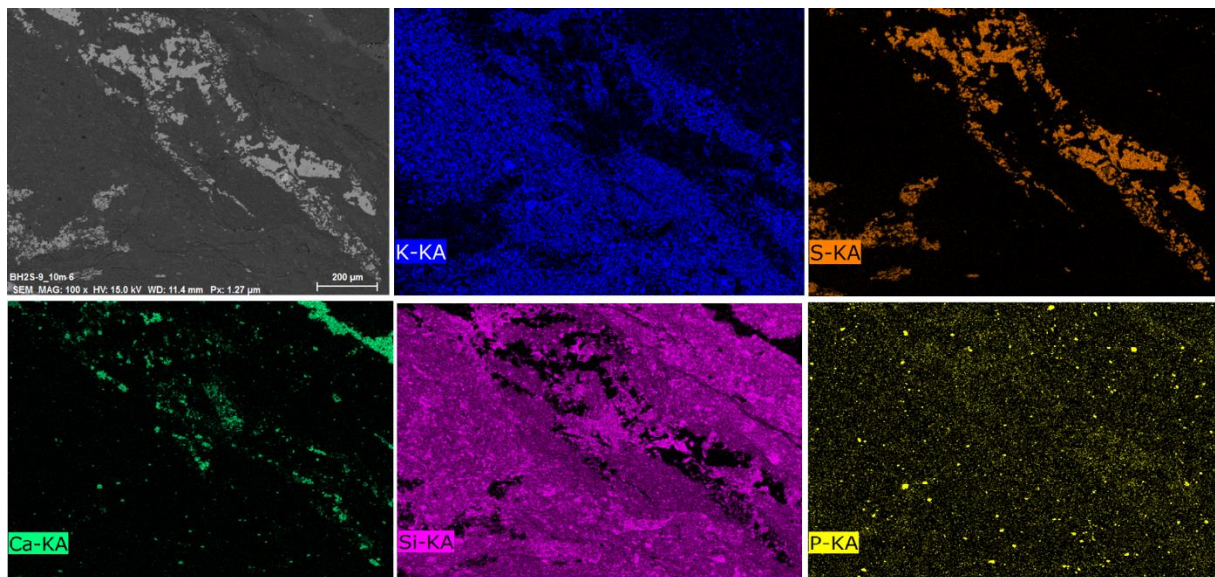## Appendix IV-V: Reflected light microscopy photos of BH2S
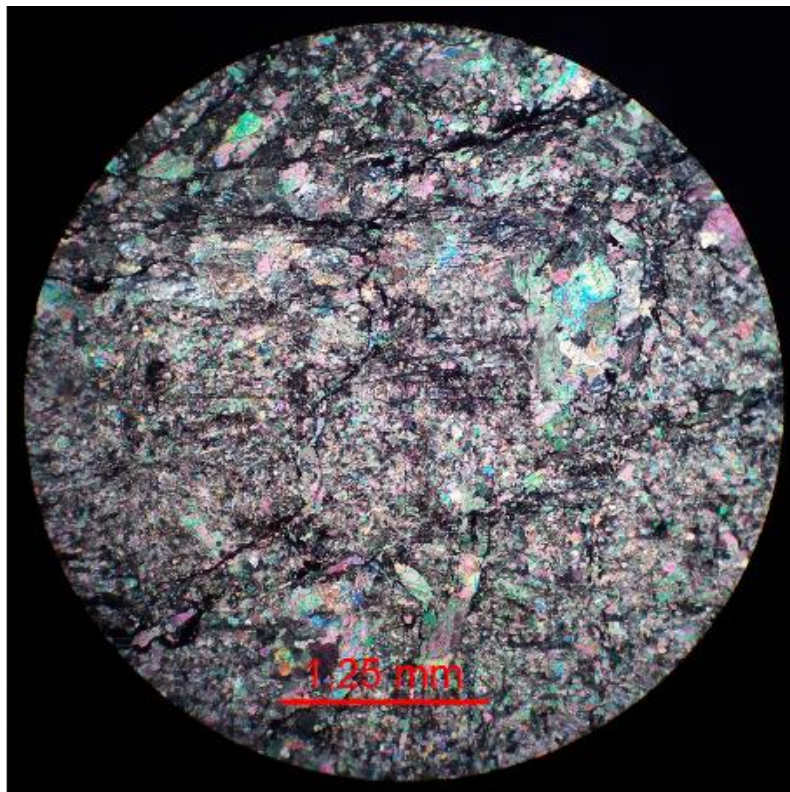
BH2S – 5 m
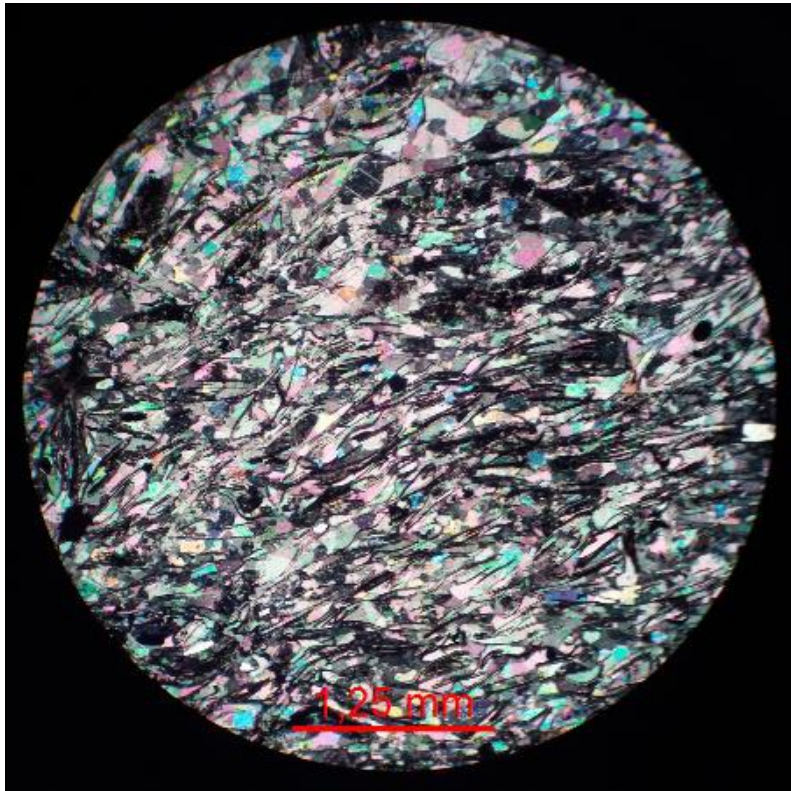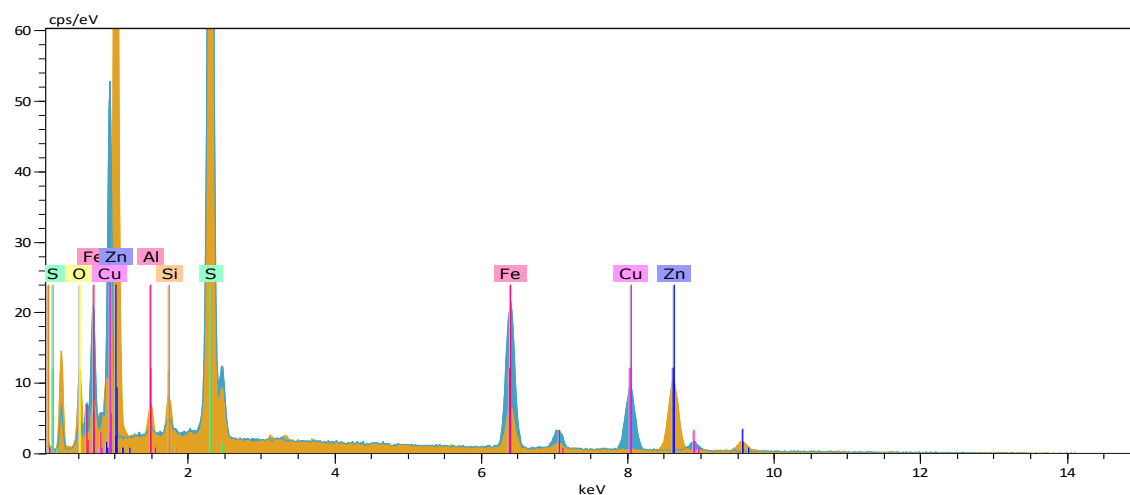
BH2S – 15 m
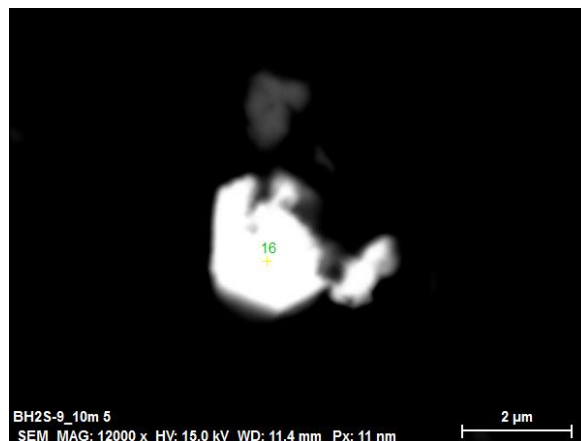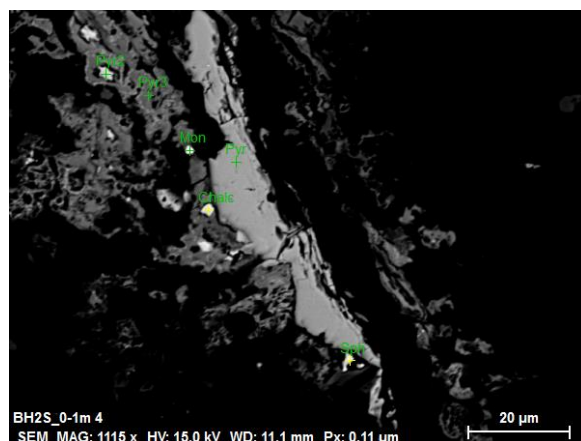
Appendix IV-VI: SEM images of BH2S

Mapping, BH2S – 1 m, image taken at 100x magnification

Mapping, BH2S – 9 m, image taken at 100x magnification
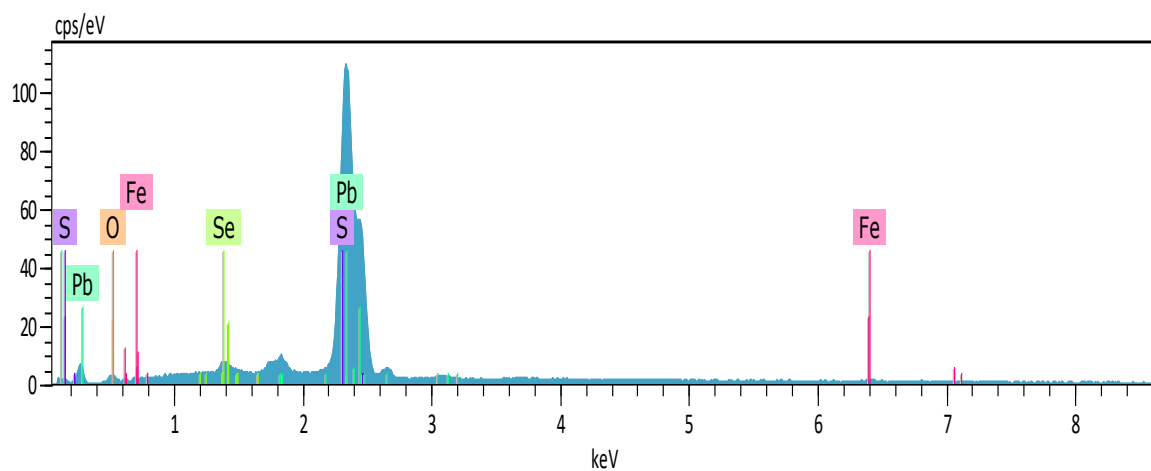
BH2S: Sphalerite, chalcopyrite and galena

BH2S_0-1m 4
SEM MAG: 1115 x HV: 15.0 kV WD: 11.1 mm Px: 0.11 µm   20 µm

BH2S-9_10m 5
SEM MAG: 12000 x HV: 15.0 kV WD: 11.4 mm Px: 11 nm   2 µm

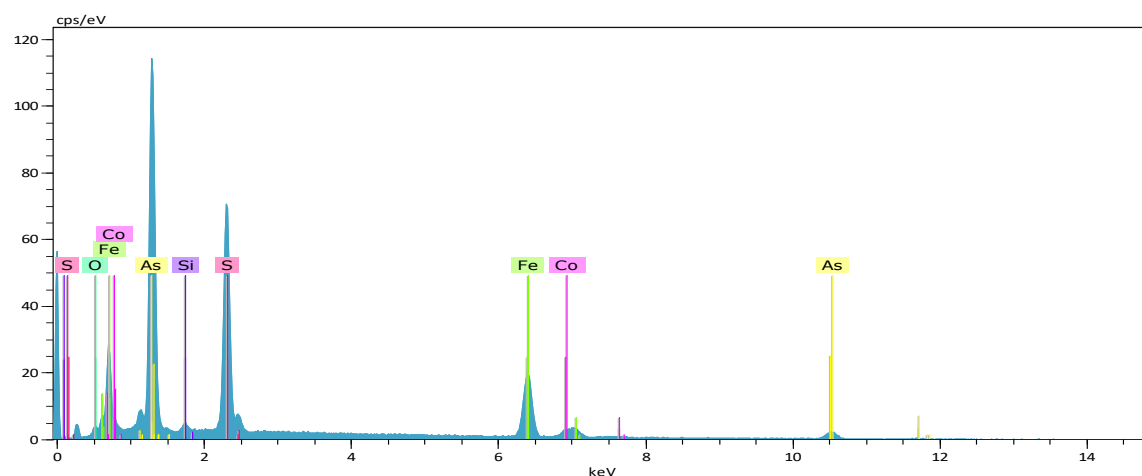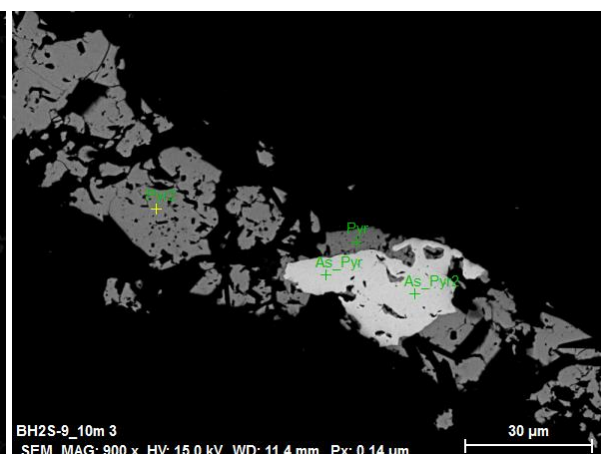| BH2S – 1 m Chalc | Date:22/03/2017 15:10:59 | HV:15.0kV | Puls th.:41.42kcps |
| BH2S – 1 m Sph | Date:22/03/2017 15:10:30 | HV:15.0kV | Puls th.:41.12kcps |

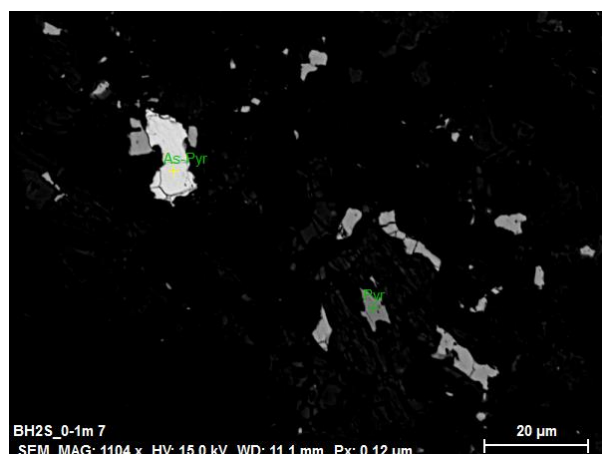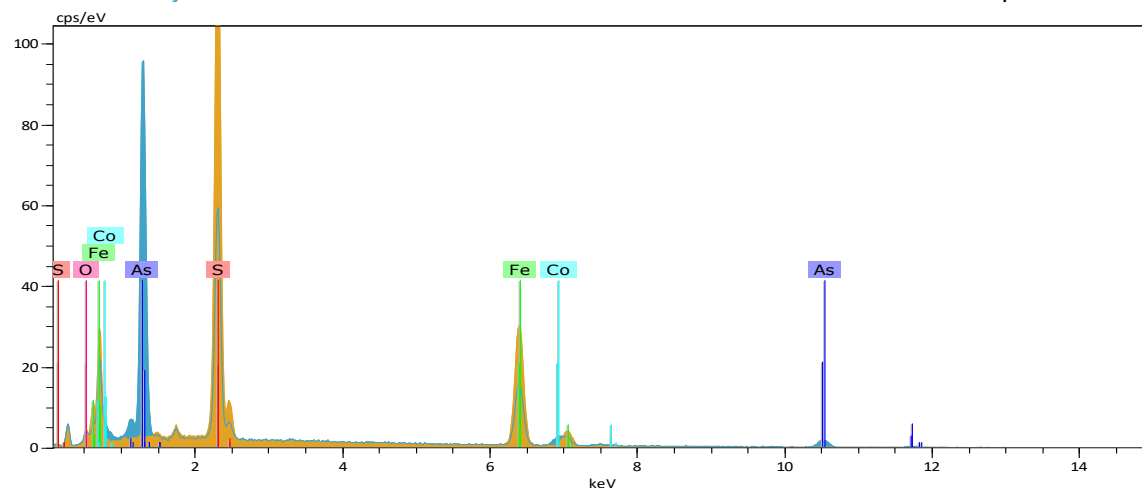BH2S – 9 m 16   Date:22/02/2017 13:44:27   HV:15.0kV   Puls th.:41.07kcps

BH2S: Arsenopyrite
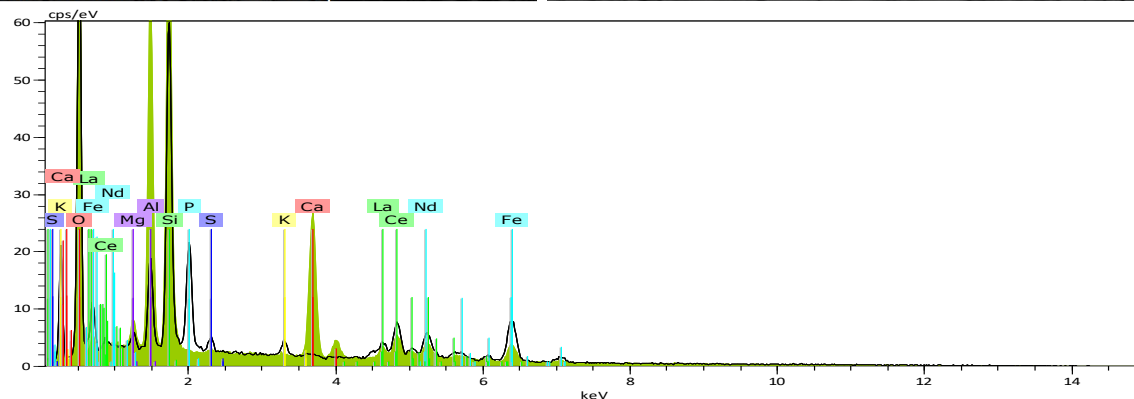

BH2S – 1 m As-Pyr   Date:22/03/2017 15:43:38   HV:15.0kV   Puls th.:42.49kcps

BH2S – 9 m   As_Pyr   Date:22/02/2017 13:32:15   HV:15.0kV   Puls th.:36.79kcps
BH2S – 9 m   Pyr2   Date:22/02/2017 13:32:38   HV:15.0kV   Puls th.:36.28kcps

BH2S: Monazite, Allanite and zircon

BH2S – 1 m Mon   Date:22/03/2017 14:53:01   HV:15.0kV   Puls th.:38.11kcps
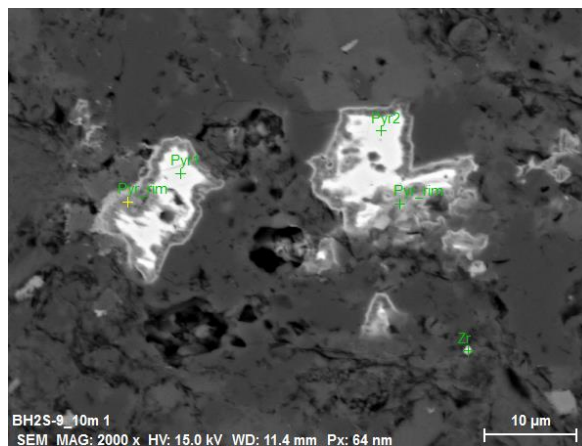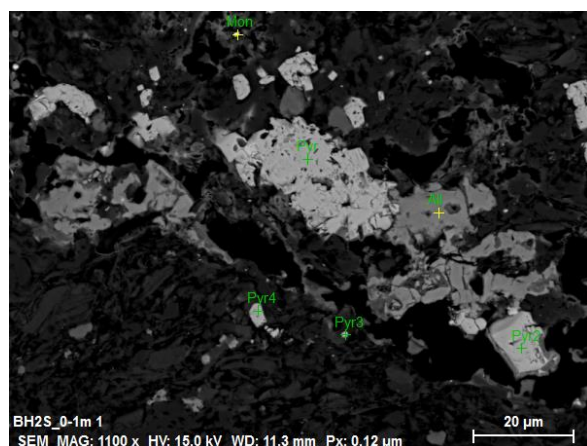BH2S – 1 m All   Date:22/03/2017 14:53:16   HV:15.0kV   Puls th.:40.53kcps
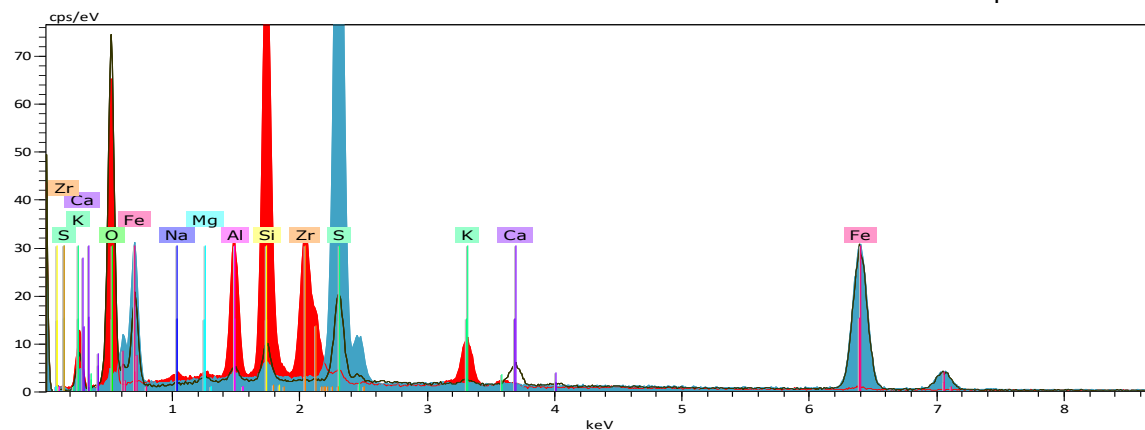
BH2S – 9 m Pyr1   Date:22/02/2017 13:07:37   HV:15.0kV   Puls th.:36.32kcps
BH2S – 9 m Pyr_rim   Date:22/02/2017 13:07:45   HV:15.0kV   Puls th.:28.30kcps
BH2S – 9 m Zr   Date:22/02/2017 13:08:12   HV:15.0kV   Puls th.:33.98kcps

Appendix V: Results from cation analysis of water samples from the column leaching experiment.

Results from cation analysis of water samples from the column leaching experiment. All units in mg/l.

	Na	K	Mg	Ca		Na	K	Mg	Ca
Column 1					**Column 3**				
07.des	-0.74	6.53	0.40	11.87	07.des	0.33	2.31	0.45	15.06
08.des	-0.02	0.77	0.09	5.69	08.des	-0.05	0.10	0.00	5.41
09.des	-0.06	0.13	0.24	5.27	09.des	0.08	0.21	-0.07	4.92
12.des	-0.02	0.09	0.44	5.20	12.des	0.02	0.14	0.76	5.42
13.des	-0.15	0.37	0.39	5.46	13.des	-0.33	-0.12	0.32	5.11
14.des	0.14	0.07	0.39	5.53	14.des	0.18	-0.07	0.31	5.14
15.des	-0.01	0.05	0.41	5.77	15.des	0.01	0.04	0.31	4.94
16.des	0.33	0.13	0.88	15.84	16.des	0.06	0.09	0.38	8.88
16.jan	1.81	1.44	11.85	0.00	19.des	-0.04	0.03	0.36	5.41
					21.des	-0.28	0.00	0.00	-0.22
					16.jan	1.80	0.46	3.98	0.00
Column 2					**Column 4**				
07.des	1.23	9.08	0.62	21.02	07.des	-0.23	3.49	0.55	23.68
08.des	0.00	0.58	0.15	5.61	08.des	-0.08	0.40	0.22	6.06
09.des	0.02	0.13	-0.04	5.76	09.des	-0.05	0.05	-0.01	5.25
12.des	0.01	0.13	0.46	5.27	12.des	0.03	0.13	0.35	5.11
13.des	-0.26	-0.09	0.32	5.43	13.des	-0.27	-0.08	0.38	5.12
14.des	0.09	0.11	0.32	5.63	14.des	0.12	-0.08	0.00	5.25
15.des	-0.03	0.08	0.00	5.34	15.des	-0.07	0.13	0.33	5.15
16.des	0.25	0.20	0.50	12.00	16.des	0.11	0.10	0.58	10.68
19.des	0.04	0.38	0.54	9.16	19.des	0.05	0.13	0.46	6.27
21.des	0.00	0.13	0.45	6.23	21.des	0.23	3.79	0.43	5.71
16.jan	1.78	0.74	3.49	0.00	16.jan	1.37	0.48	3.78	0.00

Appendix VI – PHREEQC code (for model with calcite)

DATABASE c:\phreeqc\database\llnl.dat

RATES #Pyrite oxidation code adapted from Apello and Postma, 2005.

Pyrite # rates from data compiled by Williamson and Rimstidt 1994.

-start

1 A = 0.73 * m0 # surface area in m2/dm3

10 if SI("Pyrite")>0 then goto 100 #Check if solution is saturated for pyrite

20 fH = mol("H+")

30 fFe2 = (1 + tot("Fe(2)")/1e-6)

40 if mol("O2") < 1e-6 then goto 80 #Check if dissolved oxygen is present

50 rO2 = 10^-10.19 * mol("O2")^0.5 * fH^-0.11 # rate with dissolved oxygen

60 rO2_Fe3 = 6.3e-4 * tot("Fe(3)")^0.92 * fFe2^-0.43 # rate with dissolved oxygen and Fe3+

70 goto 90

80 rem

81 rFe3 = 1.9e-6 * tot("Fe(3)")^0.28 * fFe2^-0.52 * fH^-0.3 # rate with Fe3+, without oxygen, and for pH < 3

90 rate = A * (m/m0)^0.67 * (rO2 + rO2_Fe3 + rFe3) * (1 - SR("Pyrite"))

91 moles = rate*time

100 save moles

-end

Sphalerite #0-th order rate law for sphalerite

-start

1 K = 4e-12

20 rate = K*((m/m0))*((1-SR("Sphalerite")))

21 moles = rate*time

100 save moles

-end

U-apatite #0-th order rate law for U-apatite

-start

1 K = 6e-13

20 rate = K*(m/m0)*(1-SR("Hydroxylapatite"))

21 moles = rate*time

100 save moles

-end

END

#Define a starting solution in equilibrium with alum shale minerals and atmospheric O2

Solution 1

EQUILIBRIUM_PHASES 1

   O2(g)   -0.68

   Calcite   0.0   0.99

   Goethite 0.0   0.0

   Gypsum   0.0   0.0

SAVE SOLUTION 1

END

#Pyrite, sphalerite and U-apatite oxidation using rates defined in RATES

KINETICS 1

Pyrite

 -m0 2.1 m 2.1 #Define amount of mineral phase (moles)

Sphalerite

 -m0 0.02 m 0.02

U-apatite

 -m0 0.05 m 0.05

 -formula Ca4.85U0.15(PO4)3(OH) #Alternative formula for U-apatite

 -cvode true

 -steps 1.5778463e9 in 500 steps #500 steps over 50 years

INCREMENTAL_REACTIONS true

END

USE solution 1

USE equilibrium_phases 1

USE kinetics 1

USER_GRAPH 1

   -headings   time pH

   -axis_titles   "Time, in days" "pH" ""

   -chart_title   "fixed P(O2)"

   -axis_scale x_axis   auto auto auto auto

   -initial_solutions   true

   -connect_simulations   false

   -plot_concentration_vs x

  -start

10 graph_x total_time/86400

20 graph_y -LA("H+")

 -end

   -active   true

USER_GRAPH 2

   -headings   time Sulfate

   -axis_titles   "Time, in days" "mg/l"

   -chart_title   "Equilibrium P(O2)"

   -axis_scale x_axis   auto auto auto auto

   -initial_solutions   true

122

```
    -connect_simulations    false

    -plot_concentration_vs  x

  -start

10 graph_x  total_time/86400

20 graph_y tot("S(6)")*96.06e3

  -end

    -active              true

USER_GRAPH 3

    -headings             time Ca

    -axis_titles          "Time, in days" "mg/l"

    -chart_title          "Equilibrium P(O2)"

    -axis_scale x_axis      auto auto auto auto

    -initial_solutions      true

    -connect_simulations    true

    -plot_concentration_vs  x

  -start

10 graph_x  total_time/86400

20 graph_y tot("Ca")*40.08e3

  -end

    -active              true

USER_GRAPH 4

    -headings             time Zn

    -axis_titles          "Time, in days" "mg/l"

    -chart_title          "Equilibrium P(O2)"

    -axis_scale x_axis      auto auto auto auto

    -initial_solutions      true

    -connect_simulations    true

    -plot_concentration_vs  x

  -start

10 graph_x  total_time/86400

20 graph_y tot("Zn")*65.39e3

  -end

    -active              true
```

```
USER_GRAPH 5

    -headings          time U

    -axis_titles       "Time, in days" "mg/l"

    -chart_title       "Equilibrium P(O2)"

    -axis_scale x_axis    auto auto auto auto

    -initial_solutions    true

    -connect_simulations   true

    -plot_concentration_vs  x

  -start

10 graph_x  total_time/86400

20 graph_y tot("U")*238.03e3

  -end

    -active            true

SELECTED_OUTPUT 1

 -file model2.txt

 -selected_out true

 -user_punch true

 -time true

 -totals U Zn Ca S(6)

END
```